Czech Technical University in Prague
Faculty of Electrical Engineering

Doctoral Thesis

February 2021

Ing. Jiří Šmarhák

Czech Technical University in Prague
Faculty of Electrical Engineering

Department of Microelectronics

Simulation of Carbon-based Nanostructures

Doctoral Thesis

Ing. Jiří Šmarhák

Prague, *February 2021*

Doctoral study program:
P 2612 Electrical Engineering and Information Technology

Study field:
2612V015 Electronics

Supervisor: *Doc. RNDr. Jan Voves, CSc.*

Prohlášení

Prohlašuji, že jsem tuto disertační práci vypracoval samostatně a výhradně s použitím citovaných pramenů, literatury a dalších odborných zdrojů.

V Praze, dne: 28.2.2021 ……

Jiří Šmarhák

Acknowledgement

This work has been kindly supported by grants of Grant Agency, Czech Republic No. P108/11/0894, and by student grants of CTU No. SGS 13/802810/13134 and SGS 13/207/OHK3/3T/13.

I'd especially like to thank my supervisor Jan Voves for leadership and patience.

Abstrakt

Tato práce se zabývá simulacemi nanostruktur založených na uhlíku, s ohledem na jejich využití v elektronice. Nejprve je provedena rešerše současného stavu znalostí v oboru nanostruktur a jejich samosestavování, která obsahuje také výhled do budoucna. Dále je, dle dostupné literatury, rozebrána teorie transferu elektronů v molekulárních systémech a teorie transportu proudu v nanostrukturách. Práce dále obsahuje popis některých molekul a materiálů založených na uhlíku současně s popisem současného stavu poznání výzkumu v dané oblasti. Konečně, práce obsahuje výsledky simulací nanostruktur založených na grafénu, helicénu a annulénu, uskutečněné v software Synopsys QuantumATK.

Klíčová slova: nanostruktury, grafén, helicén, annulén

Abstract

This work deals with carbon-based nanostructures simulations with respect to their electronic application. First, it contains an analysis of the current state of knowledge in the field of nanostructures and their self-assembly, and also some outlook for the future. The theory of electron tranfer in molecular systems and current transport in nanostructures is described in detail using the latest literature. Then, a description of carbon-based molecules and materials is made, analyzing the of state-of-art research in the field. Finally, the results of our simulations of graphene-, helicene- and annulene-based structures performed in Synopsys QuantumATK simulation software are presented and discussed.

Keywords: nanostructures, graphene, helicene, annulene

Content

1 Introduction

The recent advances in nanostructures simulation and synthesis are opening new possibilities to prepare electronic devices and to implement completely new phenomenons in electronics. One of the results of putting significant effort to graphene research was that materials based upon carbon became one of the prominent interests among material scientists. The properties diversity of different carbon allotropes and carbon-based compounds, accompanied by predictable chemical behaviour, inspired new approaches to electronic device technology and design, computer architecture etc. By employing highly ordered and anisotropic materials like carbon nanotubes, graphene nanoribbons, or nanographene quantum dots, phenomenons from quantum physics and chemistry ascended from purely theoretical to experimentally proven. Despite the rapidly advancing research, there is still no wide implementation of the identified concepts. Before this may happen, further analysis of carbon nanostructures landscape must be done.

The main goal of this thesis is theoretical analysis of carbon nanostructures with emphasis on graphene nanoribbons and helicenes. This includes definition of theoretical framework, selection of appropriate models for the chosen structures, comparison of simulation results with the current state of knowledge, and evaluation of usefulness for the specific applications.

This work describes basic knowledge needed for research of nanostructures in electronics and our, so far acquired, results of nanostructures computer simulations. The emphasis is layed upon carbon nanostructures. All is applicable for molecular-level (nanometer-scale structures) in general. Because the topic is wide and touches almost every branch, most of the information about subjects is simplified to a basic level. The text is divided in six chapters. The first chapter is an introduction to molecular-level systems and contains possible perspectives and motivation. The basic integrated circuit architectures made by means of molecular-level systems are described in this chapter as well. The second chapter describes electronic and energy transfer processes in molecules. This knowledge is important when treating large molecules and supramolecular systems. The third chapter describes theory of nanostructures simulations. It is divided in two parts: the one deals with molecular geometry optimization, the second with simulation of current transport in nanostructures. In the fourth chapter, basic informations about the used simulation software are uncovered. The fifth chapter enumerates some of the notable carbon-based nanostructures. Their description is combined with data we obtained from our calculations. In this section, our results are also compared with theoretical and experimental data from the available literature. The last chapter provides short conclusions and summarizes our achievements.

1.1 Introduction to Molecular-level Systems

As it is described in [1], a molecular-level device can be defined as an assembly of a discrete number of molecular components designed to perform a specific function. A molecular-level machine is a set of devices from which some of them have the property of movement. Example of such structure is a supramolecular assembly which performs some more complex functions resulting from the cooperation of various components. As our understanding of nature shows, this definition is fitting even for molecular devices and machines that are responsible for biological processes, although they are not designed by us but by long-term evolutionary changes. Molecular-level devices operate via electronic and/or nuclear rearrangements and, like macroscopic devices, they need energy to operate and signals to communicate with the operator.

The term molecular electronics may cover a broad range of topics. Using the most recent terminology from [2] it can be divided in two basic branches: molecular-scale electronics, and molecular materials for electronics. Molecular materials for electronics deal with bulk materials, like films or crystals (thin-film transistors, light-emitting diodes, etc.), that contain many trillions of molecules per functional unit. The properties of these units are measured on the macroscopic scale. Molecular-scale electronics deals with one to a few thousand molecules per device. This work is mainly focused on molecular-scale electronics, but in technical means these fields are often intertwined.

A promising strategy towards obtaining a technology on nanometer scale is offered by the bottom-up (small-upward) approach, which starts from atom or molecule and builds up to nanostructures [1]. One of the ideal strategies to build up nanostructures by this approach is to use knowledge from chemistry which says that atoms are reliable material which is forming molecules and they have well defined sizes and shapes. The idea that atoms could be used to construct nanoscale devices and machines was first raised by R. P. Feynman who (in his lecture "There's Plenty of Room at the Bottom") foretold that „*The principles of physics do not speak against the possibility of maneuvering things atom by atom*“. The possibility of manipulating and arranging single atoms has been demonstrated e.g. by recent atomic probe microscopy or atomic layer deposition techniques. However, the effective nano-assembly of a real device or machine by these means is highly unprobable because of the slow speed and high demands for the well defined environment where the assembly takes place. The main problem of atom-by-atom approach is the complexity of chemical behaviour of each atom. It seems that for more complex supramolecular structure, there is no way to simply put one atom to another but chemistry rules have to be applied. By applying the knowledge of chemical reactions, especially the bond-breaking and bond-making processes and by using the quantum chemistry computer numerical simulations it is possible to predict the arrangement and all the processes needed for the construction of a specific molecular device or machine. The research on supramolecular chemistry and molecular biology shows that molecules are much more convenient building blocks, than atoms, for construction of nanoscale devices and machines. Molecules are stable species whereas atoms are difficult to handle. Another example we can get from nature, because it uses the most complex assembly of self-replicating nanoscale structures so far known and mostly handles with molecules. As an example, the light-harvesting carotene molecular antenae for bacterial photosynthesis are formed by self-assembly and self-organization of many molecular components. In living cells we can e.g. see self-assembly and self-organization of proteins, managed by ribosomes and other molecular machines which communicate through different means. These processes evolved in nature spontaneously and are purely following rules of physics, chemistry, biology and they have been formed by evolutionary processes for eons. The result we have in today's nature is the whole laboratory of processes of self-

assembly and self-organization of supramolecular and well organized macroscopic systems which includes precisely controlled growth of nanotubes in cells, transport of various molecules, writing and reading of genetic code, building up structures like single-molecular layers, photonic structures and plasmonic structures, nanopores and single-atomic channels, building up compact high area surfaces, handling and compactification of long chains of molecules, etc.

The applications are appearing, e.g. in nanophotonics, inspired by self-assembled nanostructures on the moth wing [3] (**Figure 1**), or in plasmonics inspired by self-assembly of insect lenses [4] (**Figure 2**). The DNA also shows a big potential as a building block for molecular devices and machines [5, 6]. There are 3D-printing techniques to create an artificial chromosome which then takes control over the cell function when implanted in to its nucleus [7]. This method, used to create a predefined cell, will among other methods (molecular scissors etc.) may open the possibility of manipulating nanoscale structures by living cells programmed to do so. In other words, it leads to production of nanoscale devices and machines which can produce another devices and machines or simply replicate itself as life does. It as well opens the possibility to transport the necessary information about life through cosmic distances by electromagnetic waves in order to be then *in situ* assembled by a 3D-printer from the elements available at the destination point and/or basic molecular components carried by the probe. The implication of such an advanced manipulation of atoms and molecules, even over a great distances of space, are undoubtedly tempting. Therefore, a strong motivation rises to study the processes in living cells and to do *ab initio* quantum simulations of various simple structures on the molecular level in order to find their properties. Another argument for molecule-by-molecule assembly of nanodevices is that the most laboratory chemical processes today deal with molecules, not atoms. As well, molecule is an object that already has a distinct shape and carry a specific properties (e.g. those governed by the photochemical or electrochemical inputs), and the molecules can self-assemble or can be fused to create larger structures like polymers and layers. As it is mentioned in [1], the rapidly growing supramolecular chemistry is opening virtually unlimited possibilities concerning design and construction of artificial molecular-level devices and machines by means of bottom-up molecule-by-molecule approach. It is also evident that such an approach can make an invaluable contribution to better understanding the molecular-level aspects of the highly complex devices and machines that are responsible for biological processes.

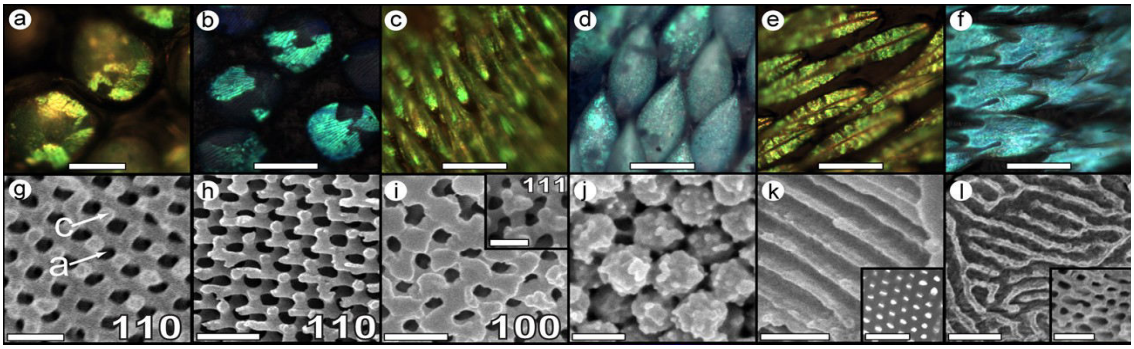

Figure 1. An example of biophotonic nanostructures which are forming by self-assembly on an arthropod wings. (**a-f**) Light micrographs, (**g-l**) electron micrographs. The image is taken from [3].

As also mentioned by authors of [1], the development of the supramolecular bottom-up approach towards the construction of nanoscale devices and machines was made possible by gaining the large amount of knowledge in the fields of organic synthesis and photochemistry, by the preparation of early examples of molecular-level devices and machines like the light-controlled molecular-level tweezers, triads for vectorial charge separation and light-harvesting

antennae, and by development of new techniques like the single molecule fluorescence spectroscopy and already mentioned atomic probe microscopy. This was also made possible by global increase in computing power and development of new algorhythms and quantum chemistry simulation methods. Also the supramolecular chemistry is rapidly developing interdisciplinary field.

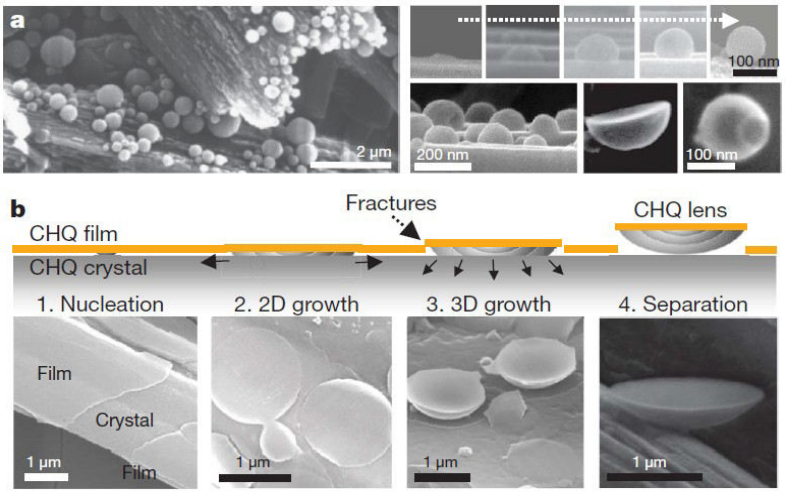

Figure 2. Self-assembly of the plano-spherical convex lenses from calix[4]hydroquinone (CHQ) inspired by insect compound eye. The image is taken from [4].

A chemical system is considered as a molecule when all its components are linked with strong (e.g. covalent) bonds only. In the most cases the molecular-level devices and machines are multicomponent chemical systems in which chemical bonds of different nature play role, and they are thus considered as supramolecular systems. This definition is yet inadequate because there is a need to take the interaction energy of molecule parts into account. The definition of a supramolecular species can be based on the degree of intercomponent electronic interactions. During photochemical stimulation, a system A~B (consisting of two units A and B with bond ~ that keeps the unit together), can be defined as a supramolecular species if light absorption leads to excited states that are substantially localized on either A or B, or causes electron transfer from A to B and *vice versa*. This is in contrast to excited states substantially delocalized on the entire system in a large molecule. Oxidation and reduction of supramolecular species can then be described as oxidation and reduction of specific units, whereas oxidation and reduction of a lerge molecule leads to species in which holes or electrons are delocalized over the entire system. When the interaction energy between units is small when compared with the other relevant energy parameters a system can be regarded as a supramolecular species, irrespective of the nature of the bonds that link its units [1].

As next stated in [1], the construction of artificial supramolecular structures via self-organization needs suitably programmed molecular components and full control of all the weak intermolecular forces (including solute-solvent interactions) involved in the thermodynamically driven formation of the desired system. This can be fulfilled by precise chemical design of the molecular components. Several supramolecular structures (e.g. helicates, grids, capsules, molecular polyhedra, etc.) have been obtained by self-association and self-organization of artificial molecular components. The construction of artificial supramolecular devices and machines by self-assembly and self-organization is a much more difficult task, because the various molecular components must be programmed not only to ensure their self-assembly into a structurally organized system but also to ensure their functional integration, as required by the operation the device or machine is expected to perform. Moreover, Supramolecular systems based on weak interaction

are fragile because they can be easily disassembled by external perturbations (e.g. change of solvent, change of pH, rise of temperature). Artificial devices and machines are therefore often constructed by following a design based on covalent interaction bonds.

The first step in the bottom-up approach is synthesis and characterization of molecular-level structures capable of responding to external stimuli. It seems likely that, for example, the molecular-based computer would operate in ways analogous to silicon-based computers where we use electrical and light stimuli. Molecules can process electrons or photons and generate electrons on photoexcitation and photons on electrical stimulation. It is therefore possible that electronics and photonics will merge increasingly as miniaturization proceeds [1]. While the construction of molecular-based computer is still in process, the design and realization of a molecular-level electronic structures as wires, switches, plugs, sockets, extensions, rectifiers, antennae, batteries, etc., is topic of a great scientific interest. Most molecular-level systems capable of function like macroscopic devices involve photoinduced electron- and/or energy-transfer processes in supramolecular species. These processes play also a fundamental role in operating biological devices and machines and therefore we discussed it more (see **Chapter 3**).

1.2 Basic Molecular-level Integrated Circuit Architectures

According to [2], there are at least three general architectural approaches to create integrated circuits for molecular-level computing. The first approach is based on quantum cellular automata (QCA). This method relies on electrostatic field repulsion to transport information throughout the circuitry. One major benefit of the QCA approach is that heat dissipation is less of an issue because only one to several electrons are used rather than thousands of electrons needed for each bit of information in classical electronic solid-state devices. The second approach is based on building of massively parallel computing device using molecular electronic-based crossbar technologies that are said to be very defect tolerant. This approach is proposed to use single-walled carbon nanotubes (SWNT) or synthetic nanowires for crossbars. Logic functions are performed either by sets of crossed and specially doped nanowires or by molecular switches placed at each junction. The third approach uses molecular-scale switches as part of a nanocell, a concept that is a hybrid between present silicon-based technology and technology based purely on molecular switches and molecular wires (but in fact all the mentioned approaches will be hybrid technologies as well, at least in the first generations). The nanocell relies on the use of arrays of molecular switches to perform logic functions but does not require each switching molecule to be individually addressed or powered. It utilizes the principles of chemical self-assembly in construction of the logic circuitry, thereby reducing complexity.

1.2.1 Quantum Cellular Automata

Quantum dots are sometimes called artificial atoms because they have discrete charge states and energy-level structures that are similar to atomic systems and can contain from a few thousands to just one electron. They are typically small electrically conducting regions, 1μm or less in size, with a variety of geometries and dimensions. Because of the small volume, the electron energies are quantized. No shell structure exists, instead of that, the generic energy spectrum has universal statistical properties associated with zero-point energy („quantum chaos“). An example of self-organized quantum dots of various dimensions, could be the structures obtained by swelling, shrinking and adaptation of graphene substrate) presented by the authors of [8] (see **Figure 3**).

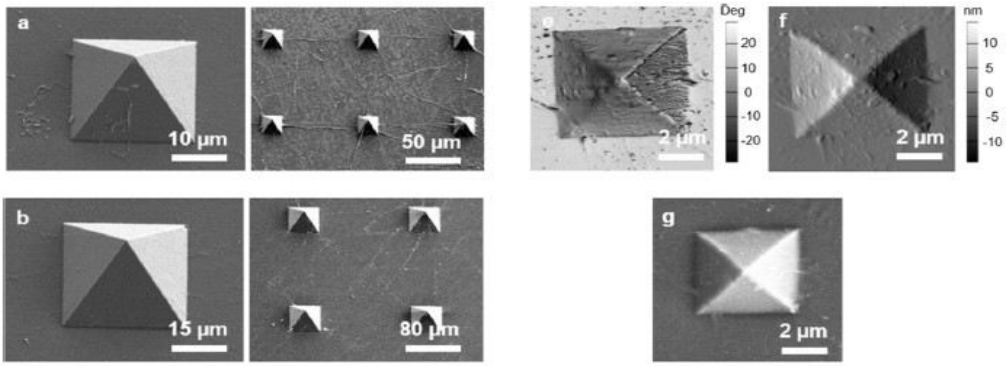

Figure 3. 3D integrated graphene of various dimensions taken by SEM. The image is taken from [8].

As more explained in [3], the principle of operation of QCA is based on the fact that electrons ale able to tunnel between dots but are unable to leave the cell. When two excess electrons are placed in the cell, Coulomb repulsion will force the electrons to occupy dots on opposite corners. The two ground-state polarizations are energetically equivalent and can be labeled as logic „0“ or „1“. Flipping the logic state of one cell, for instance by applying a negative potential to an electrode near the quantum dot occupied by an electron, will result in the neigbouring cell to flip ground states in order to reduce Coulombic repulsion force. In this way, a line of QCA cells can be used to do computations. An example of QCA topology that can produce AND and OR gates is called a majority gate and is shown in Figure 9. The three input cells „vote“ on the polarization of the central cell. The polarization of the central cell is then propagated as the output. One of the inputs can be designated as programming input and determines whether the majority gate produces an AND or an OR. If the programming gate is a logic 0, then the result shown in **Figure 4** is OR while a programming gate equal to logic 1 would produce a result of AND.

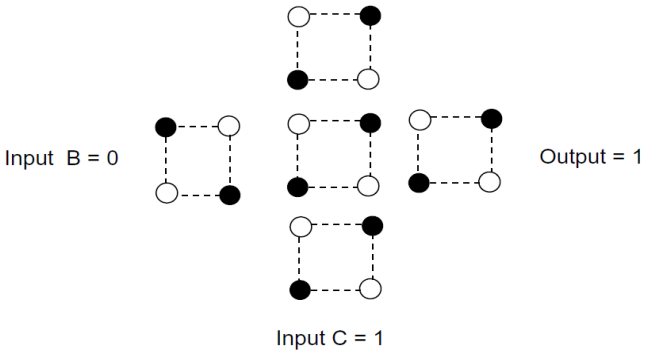

Figure 4. QCA majorty cell in which the three input cells A, B, and C determine the ground state of the center cell, which then determines the logic of the output. A logic input of 0 gives a logic output of 1. The image is taken from [2].

1.2.2 Crossbar Arrays

Another architecture mentioned in [2], the molecular computer (based on so called Teramac design), is using wires that make up the address lines controlling the settings of the configuration switches and the data lines that link the logic devices. Large amount of research has been done in the branch of nanowires. Very promising material for nanowire preparation (mostly by top-down approach) are graphene-based structures and helicenes, as more explored in our work. As explored by the authors of [5, 6], another possible nanowire is a DNA molecule. An example of carbon nanotubes (CNT) usage as an electronic component is in the **Figure 5**.

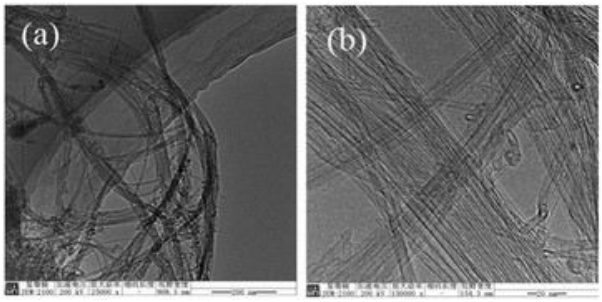

Figure 5. An example of bistable electrical switching by means of carbon nanotubes network and organic molecules. The image is taken from [9].

1.2.3 The Nanocell Approach

This approach, also described in [2], uses a theoretical treatment of the electron transport through single molecules attached to metal surface and there is also an analysis of the electrical behavior of many molecules. For example oligo(phenylene ethynylene) molecules. These molecules were examined in nanopore testing device (emulating electrode connection) and were exhibiting large ON:OFF ratios and negative differential resistance. The peak-to-valley ratio was 1030:1 at 60 K. The same nanopore testing device was used to study the ability of the molecules to hold their ON states for extended periods of time. The performance of molecules as molecular memory device was tested, and in this study only the two nitro-containing molecules were found to exhibit storage characteristics. The write, read, and erase cycles are shown in **Figure 6**. An example of I/V characteristics of Au-molecule-Au device are shown in the **Figure 7**. The characteristics are repeatable to high accuracy with no degradation of the device noted even after 1 bilion cycles over a one-year period. As being feasible in terms of computational power but still dealing with matter on a nanoscale, this approach is widely used in this work.

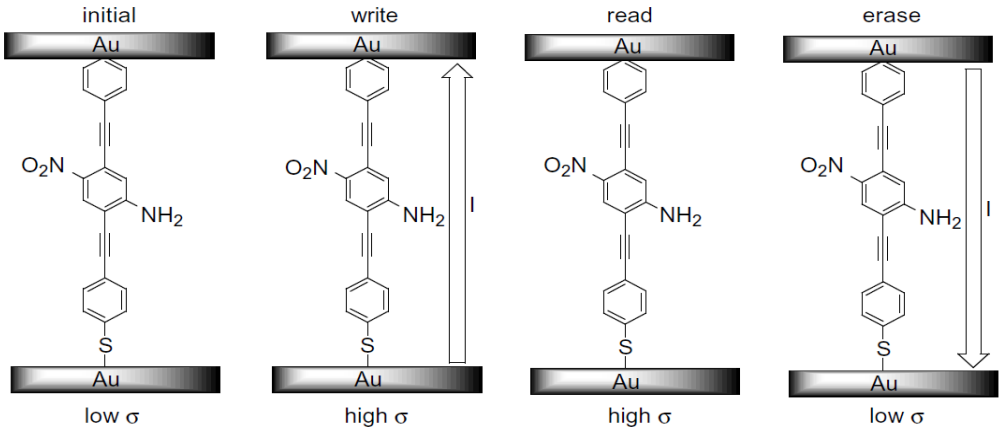

Figure 6. The memory device operates by storage of high- or low-conductivity state. The image is taken from [2].

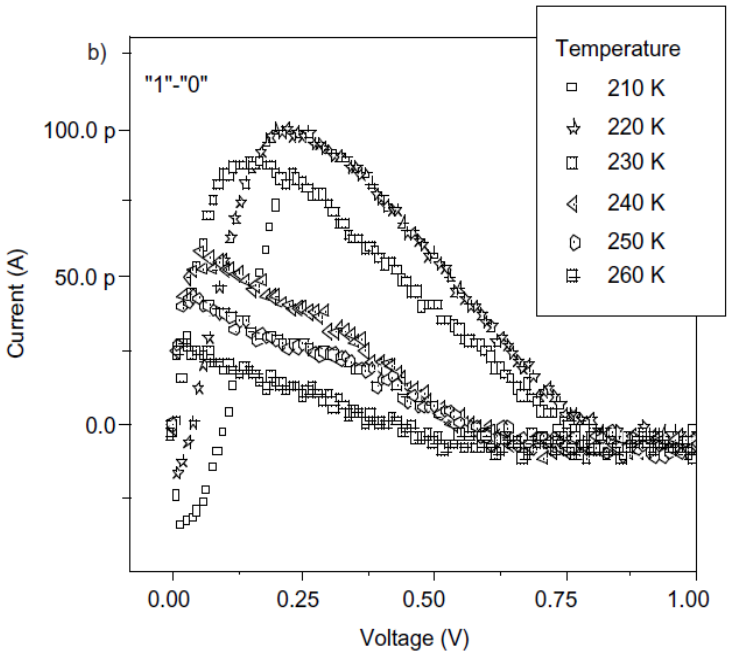

Figure 7. The I/V characteristics of Au-molecule-Au device at different temperatures. The image is taken from [2].

2 Photoinduced Electron- and/or Energy-transfer Processes

The following chapter is based upon the literature [1]. An electronically excited state obtained when a molecule absorbs light of suitable energy is a species with properties different from those of the ground state molecule. An excited state may be involved in electron-transfer processes and it can also transfer energy to another molecule. Let us consider an A-L-B supramolecular system, where A is the light-absorbing molecular unit, B is the other molecular unit involved with A in the light-induced processes, and L is a connecting unit (bridge). In this system, the photoinduced electron- and/or energy-transfer processes can be indicated as in **Equations (1-4)**:

A-L-B + $h\nu$ → *A-L-B	photoexcitation	**(1)**
*A-L-B → A^{+}-L-B^{-}	oxidative electron transfer	**(2)**
*A-L-B → A^{-}-L-B^{+}	reductive electron transfer	**(3)**
*A-L-B → A-L-*B	electronic energy transfer	**(4)**

Photoinduced electron-transfer processes are followed by spontaneous back-electron-transfer reactions that regenerate the starting ground state of the system **Equations (5, 6)** and photoinduced energy transfer is followed by radiative and/or non-radiative deactivation of the excited acceptor **Equation (7)**.

A^{+}-L-B^{-} → A-L-B	back electron transfer	**(5)**
A^{-}-L-B^{+} → A-L-B	back electron transfer	**(6)**
A-L-*B → A-L-B + $h\nu$	excited state decay	**(7)**

2.1 Electron Transfer

For mentioned photoinduced electron-transfer processes the relevant excited-state thermodynamic properties are the reduction potential for the couples A^{+}/*A (**Equation (2)**) and *A/A^{-} (**Equation (3)**). Because of its higher energy content, an excited state is both a stronger reductant and a stronger oxidant than the corresponding ground state. The first approximation is that the redox potentials of the excited state couples can be calculated from the potentials of the ground state couples and the one-electron potential corresponding to the zero-zero excitation energy, as shown by **Equations (8, 9)**:

$$E(A^{+}/^{*}A) \approx E(A^{+}/A) - E^{0\text{-}0} \qquad \textbf{(8)}$$

$$E(^{*}A/A^{-}) \approx E(A/A^{-}) + E^{0\text{-}0} \qquad \textbf{(9)}$$

Electron-transfer processes involving excited states and those involving ground state molecules can be kinetically dealt within framework of the Marcus theory and by more theoretical models. Quantum mechanically both the photoinduced and back-electron-transfer processes can be viewed as radiationless transitions between different, weakly interacting electronic states of the A-L-B supermolecule. The rate constant of such processes is given by Fermi „golden rule“ expression:

$$k_{el} = (4\pi/h)(H^{el})^2 FC^{el} \qquad \textbf{(10)}$$

where H^{el} is the electronic coupling and FC^{el} the Franck-Condon density of states.

2.1.1 Electronic Factor

In the absence of any intervening medium, the electronic factor decreases exponentially with increasing distance:

$$H^{el} = H^{el}(0)\, e^{\frac{-\beta^{el}}{2}(r_{AB} - r_0)} \qquad \textbf{(11)}$$

where r_{AB} is the donor-acceptor distance, $H^{el}(0)$ is the interaction at the contact distance r_0, and β^{el} is an attenuation term. The 1/2 factor arises because originally β^{el} was defined as the exponential attenuation parameter for rate constant rather than for electronic coupling **Equation (12)**:

$$k_{el} \propto e^{-\beta^{el} r_{AB}} \qquad \textbf{(12)}$$

For donor-acceptor components separated by vacuum, β^{el} is estimated to be in range 2-5 $Å^{-1}$. When donor and acceptor are separated by matter (e.g. the bridge L), the electronic coupling can be mediated by mixing of the initial and final states of the system with virtual high energy electron-transfer states involving the intervening medium as illustrated in **Figure 8** (superexchange mechanism).

The second-order perturbation expression describing the superexchange coupling is:

$$H^{el} = \frac{H_{ie} H_{fe}}{\Delta E_e} + \frac{H_{ih} H_{fh}}{\Delta E_h} \qquad \textbf{(13)}$$

where H_{ie}, H_{fe}, H_{ih}, and H_{fh} are the appropriate donor-bridge and bridge-acceptor coupling elements (**Figure 8a**), and ΔE_e and ΔE_h are the energy differences between the virtual states and the initial or final state (these energy differences are taken at the transition state nuclear geometry, where the initial and final state have the same energy). From **Equation (13)** it follows that readily reducible bridges are good electron-transfer mediators, and readily oxidizable bridges are good hole-transfer mediators. For modular bridges the superexchange model can be extended to involve virtual electron-transfer states localized on each modular unit, as shown on **Figure 8b**. For a system involving n identical modular units, **Equation (11)** can be replaced with **Equation (14)**:

$$H^{el} = \frac{H_{i1} H_{nf}}{\Delta E} + \left(\frac{H_{12}}{\Delta E}\right)^{n-1} \qquad \textbf{(14)}$$

In such a case, an exponential dependence on number of modular units contained in the bridge is obtained, which means an exponential dependence on donor-acceptor distance (measured along the bridge). **Equations (11)** and **(14)** can be related considering that r_0 is the length increment associated with a single module, $H^{el}(0)$ is the donor-acceptor coupling for a one-module bridge ($(H^{i1}H^{nf})/\Delta E$), and the attenuation factor β^{el} is a bridge-specific parameter which depends on the magnitude of the coupling between adjacent modules and on the energy of the electron- (or hole-) transfer states

localized on each module.

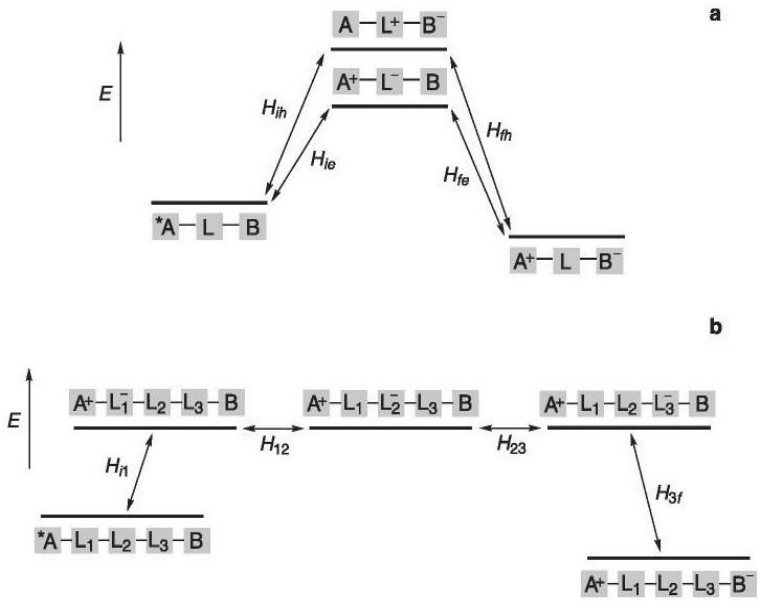

Figure 8. State diagram illustrating the superexchange interaction between an excited state electron donor (*A) and an electron acceptor (B) through **a)** simple and **b)** molecular bridges. In the second example only the electron-transfer virtual states of the bridge are shown. The image is taken from [1].

2.1.2 Nuclear Factor

The FC^{el} term of **Equation (10)** is thermally averaged Franck-Condon factor connecting the initial and final states. It contains a sum of overlap integrals between the nuclear wavefunctions of initial and final states of the same energy. Both inner and outer (solvent) vibrational models are included. The general expression of FC^{el} is quite complicated. It can be shown that in the high temperature limit ($h\nu < k_BT$) an approximation sufficiently accurate for many room temperature processes, the nuclear factor takes the simple form:

$$FC^{el} = \sqrt{\frac{1}{4\pi\lambda k_B T}}\, e^{-\frac{(\Delta G^\circ + \lambda)^2}{4\lambda k_B T}} \qquad \textbf{(15)}$$

where λ is the sum of the inner (λ_i) and outer (λ_0) reorganizational energies. The exponential term of **Equation (15)** is the same as that predicted by the classical Marcus model based on parabolic energy curves for initial and final states. Both classical and quantum mechanical models contain an important predistions like that the three distinct kinetic regimes exist, depending on the driving force of the electron-transfer process. The first regime is a normal regime for small driving forces ($-\lambda < \Delta G^\circ < 0$) in which the process is thermally activated and its rate increases with increasing driving force. The second is an activationless regime ($-\lambda \approx \Delta G^\circ$) in which a change in the driving force does not cause large changes in the reaction rate. And the last is an „inverted“ regime for strongly exergonic processes ($-\lambda > \Delta G^\circ$) in which the rate of the process decreases with increasing driving force.

The three kinetic regimes are shown in terms of the classical Marcus parabolae in **Figure 9**, along with the difference between predictions of the classical and quantum mechanical models in the inverted region (parabolic or linear decreases of $\ln(k_{el})$ with increasing driving force).

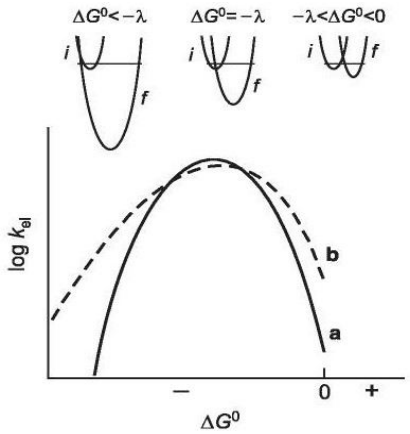

Figure 9. Free energy dependence of electron-transfer rate (i, initial state; f, final state) according to **a)** classical and **b)** quantum mechanical treatments. The three kinetic regimes (normal, activationless, and „inverted“) are shown in terms of Marcus parabolae. The image is taken from [1].

2.2 Energy Transfer

The thermodynamic ability of an excited state to intervene in energy-transfer processes is related to its zero-zero spectroscopic energy, $E^{0\text{-}0}$. The energy-transfer process must obey energy conservation and requires some kind of electronic interaction between donor and acceptor. Energy transfer in a supramolecular system can be viewed as a radiationless transition between two „localized“ electronically excited states (**Equation (4)**). The rate constant can be obtained by use of an appropriate „golden rule“ expression:

$$k_{en} = (4\pi/h)(H^{en})^2 FC^{en} \qquad \textbf{(16)}$$

where H^{en} is the electronic coupling between the two excited states interconverted by the energy-transfer process and FC^{en} is an appropriate Franck-Condon factor.

2.2.1 Coulombic Mechanism

The electronic factor H^{en} is a two-electron matrix element involving the HOMO and LUMO of the energy-donor and energy-acceptor components. This factor can be split into two additive terms, a Coulombic term and an exchange term. The two terms depend differently on the parameters of the system (spin ground and excited states, donor-acceptor distance, etc.) and each can become predominant depending on the specific system and experimental conditions. The orbital aspects of the two mechanisms are represented in **Figure 10**. The Coulombic (also called resonance, Förster-type, or through-space) mechanism is a long-range mechanism that does not require physical contact between donor and acceptor. It can be shown that the most important term within the Coulombic interaction is the dipole-dipole term, which obeys the same selection rules as the corresponding electric dipole transitions of the two partners ($^*A \rightarrow A$ and $B \rightarrow {}^*B$), **Figure 10**.

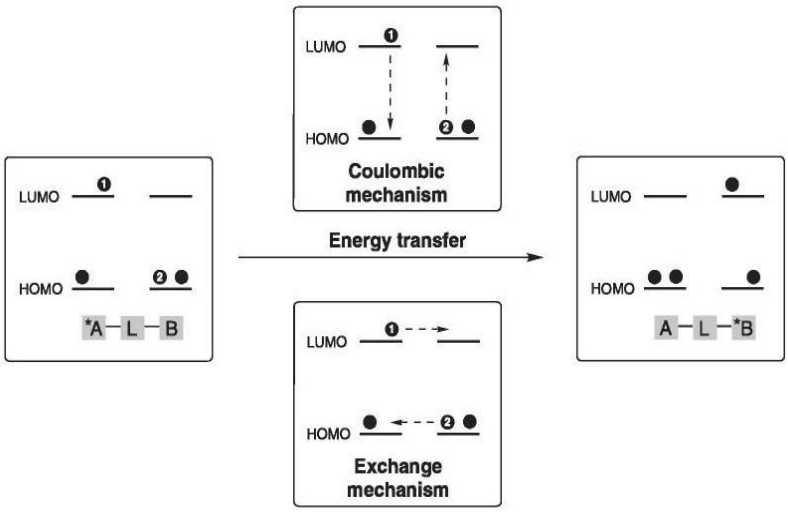

Figure 10. Schematic representation of the Coulombic and exchange energy-transfer mechanisms. The image is taken from [1].

Coulombic energy transfer is therefore expected to be efficient in systems in which the radiative transitions connecting the ground and the excited states of the each partner have high oscillator strength. The rate constant for the dipole-dipole Coulombic energy transfer can be expressed as a function of the spectroscopic and photophysical properties of the two molecular components:

$$k_{en}^{F}=8.8\times10^{-25}\frac{K^2\Phi}{n^4\tau r_{AB}^6}J_F \qquad \textbf{(17)}$$

where

$$J_F=\frac{\int F(\bar{\nu})\varepsilon(\bar{\nu})/\bar{\nu}^4 d\bar{\nu}}{\int F(\bar{\nu})d\bar{\nu}} \qquad \textbf{(18)}$$

where K is an orientation factor which takes into account the directional nature of the dipole-dipole interaction (K^2 = 2/3 for random orientation), Φ is the luminiscence quantum yield and τ is the lifetime of the donor, n is the solvent refractive index, r_{AB} is the distanec (Å) between donor and acceptor, and J_F is the Förster overlap integral between the luminiscence spectrum of the donor, $F(\bar{\nu})$ and the absorption spectrum of the acceptor, $\varepsilon(\bar{\nu})$, on an energy scale (cm^{-1}). With a good spectral overlap integral and appropriate photophysical properties, the $1/r_{AB}^6$ distance dependence enables energy transfer to occur efficiently over distances substantially exceeding the molecular diameters. A typical example of an efficient Coulombic mechanism is that of singlet-singlet energy transfer of the photosynthetic apparatus.

2.2.2 Exchange Mechanism

The exchange (also called Dexter-type) mechanism requires orbital overlap between donor and acceptor, either directly or mediated by the bridge (through-bond) and decay is, therefore, exponentially dependent on distance. The exchange interaction can be regarded as double electron transfer process (**Figure 10**), one electron moving from the LUMO of the excited donor to the LUMO of the acceptor, and the other from the acceptor HOMO to the donor HOMO. This important insight is illustrated in the **Figure 11**. The attenuation factor β^{en} for exchange energy transfer shoud be

approximately equal to the sum of the attenuation factors for two separated electron-transfer processes. In example β^{el} for electron transfer between the LUMO of the donor and acceptor, and β^{ht} for the electron transfer between the HOMO (*ht* index denotes hole transfer from the donor to the acceptor). This prediction has been confirmed by experiments. The spin selection rules for this type of mechanism arise from the need to obey spin conservation in the reacting pair as a whole. This enables the exchange mechanism to be operative in many instances in which the excited states involved are spin-forbidden in the unusual spectroscopic sense. Thus, the typical example of an efficient exhange mechanism is that of triplet-triplet energy transfer. Although the exchange mechanism was originally formulated in terms of direct overlap between donor and acceptor orbitals, it is clear that it can be extended to coupling mediated by the intervening medium (i.e. the connecting bridge), as discussed above for electron-transfer processes (superexchange mechanism).

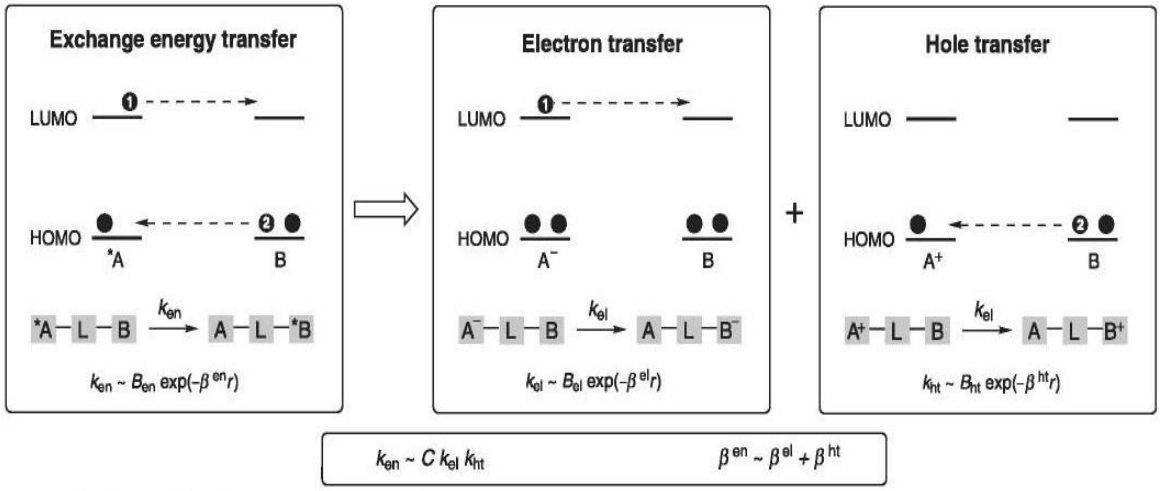

Figure 11. Analysis of the exchange energy-transfer mechanism in terms of electron- and hole-transfer processes. The relationships between the rate constants and the attenuation factors of the three processes are also shown. The image is taken from [1].

2.3 Role of the Connecting Bridge

The connecting units (bridges) play important role in the mediation of electron- and energy-transfer processes between donor and acceptor components in supramolecular structures. It has become customary to consider bridges as „molecular wires“ and to talk their „conducting“ properties. In the superexchange mechanism the bridge levels are always much higher in energy than those of donor and acceptor, so the electron tunnels in a single step from donor to acceptor and the rate of the process varies according to **Equation (12)**. Electron transfer through such bridges is not comparable with electron transfer in macroscopic systems where the electron really moves along the wire. It might happen that the energy level of the bridge is so low that it becomes intermediate between the initial and final states. In such cases, electron hopping occurs (**Figure 12a**) and the bridge is directly involved in the process.

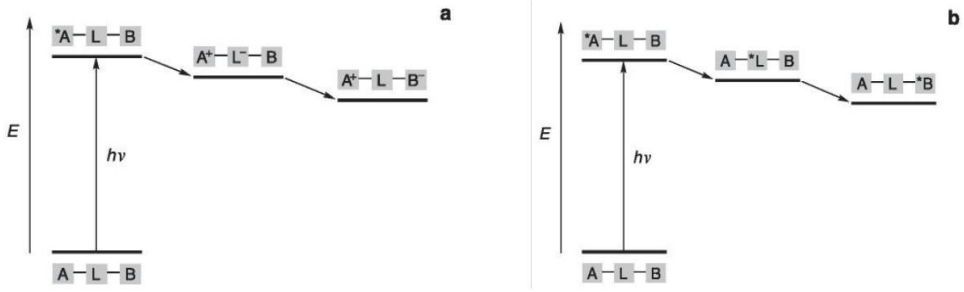

Figure 12. Representation of sequential donor-bridge-acceptor **a)** electron transfer and **b)** energy transfer hopping mechanisms. The image is taken from [1].

A similar situation can also be encountered for energy-transfer processes (**Figure 12b**). When such a hopping-type mechanism is operative, very small distance dependence of their rate constants is expected. If each single hopping step occurs over the same distance the rate constant is inversely proportional to a small power of the number of hopping steps, *N*:

$$k_{el} \propto N^{-\eta}; \quad \eta \sim 1\text{-}2 \qquad \textbf{(19)}$$

Finally, when there is complete mixing among the donor/bridge/acceptor orbitals (large coupling limit) the bridge essentially acts as an incoherent molecular wire, as happens for conjugated conducting polymers, and the system is expected to behave according to an ohmic regime where the distance dependence of electron-transfer rates varies inversely with bridge length.

3 Theory of Nanostructures Simulation

The following chapter is based upon the available literature on molecular mechanics [10, 11] and recent models of quantum transport [12].

3.1 Molecular Mechanics

Method based upon the usage of Schrödinger and Newton equations is called *ab initio* or "first principle". It uses only fundamental physical parameters as input variables. An advance of this method is theoretical possibility of describing every system with all its emergent behaviour. However, the disadvantage is its growing complexity for systems with many atoms and thus enormous requirements of computational power. It is therefore necessary to apply approximations which can simplify calculation. The only parameters we have to know at the beginning are physical constants (elementary charge, mass of electron, proton and neutron) and position of atoms. There is no need to know which particular chemical elements is the system composed of or any other details about it. The first equation used to construct this model is the time-independent Schrödinger equation:

$$\mathrm{H}\Psi = E\Psi\,, \qquad \textbf{(20)}$$

where H is Hamilton operator (Hamiltonian), Ψ is wave function of electrons in the field created by ions, and E is total potential energy of system (without movement of atoms). This equation describes how atoms interact through electrons therefore it is possible to describe atomic interactions, chemical reactions and optical or stationary eletrical parameters of the system solely by solving it. Solving of this equation is based on the search for a wave function which, after application of Hamilton operator, will give the same wave function differing only by constant included in matrix of eigenvalues E (which represents total energy of the system in thermodynamic equilibrium). The time-independent Schrödinger equation depends only on coordinates of elements. Generally we can write:

$$\mathrm{H}(\{\boldsymbol{\rho}_i\};\ \{\boldsymbol{r}_i\})\Psi(\{\boldsymbol{\rho}_i\}) = E(\{\boldsymbol{r}_i\})\Psi(\{\boldsymbol{\rho}_i\})\,, \qquad \textbf{(21)}$$

where $\{\boldsymbol{\rho}_i\}$ is set of electron coordinates and $\{\boldsymbol{r}_i\}$ is set of ion coordinates. The second necessary equation in this model is Newton first law of motion:

$$\boldsymbol{F}_i = m_i\boldsymbol{a}_i\,, \qquad \textbf{(22)}$$

where $\boldsymbol{F}_i$ is total force acting on atom i because of other atoms and external fields, m_i is mass of atom i and $\boldsymbol{a}_i$ is acceleration of atom i. This equation describes how the ions are moving in the system and solution of this equation is initial value problem for differential equations. The solution is a new position of atoms and their velocities, and forces between them. Because of the fact, that solution of Schrödinger equation gives wave function and matrix of eigenvalues corresponding to potential energy which is dependent only on coordinates of ions, it is possible to calculate force $\boldsymbol{F}$ by means of gradient

$$\boldsymbol{F}_i = -\ \mathrm{grad}\ E(\{\boldsymbol{r}_i\}). \qquad \textbf{(23)}$$

From this equation we can get force $\boldsymbol{F}_i$ acting on ion i and this force substitute to motion equation **(22)** when we know mass m_i. The result is a new position of ions and which we solve for the time-independent Schrödinger equation **(20)** and the proces repeats until lowest energy difference between steps is achieved.

3.1.1 Born-Oppenheimer Approximation

Hamiltonian of a group of electrons and ions is given by the kinetic energy of electrons K_e and ions K_i and by the potential energy (of interactions) between electrons and ions V_{ei}, ions and other ions V_{ii}, and electrons with other electrons V_{ee}. It may be written as follows

$$H = K_e + K_i + V_{ei} + V_{ii} + V_{ee}. \qquad \textbf{(24)}$$

Because the ions are much heavier than electrons, and electrons therefore move at much higher velocities, we may use an approximation in which we assume ions as stationary. This approximation is called Born-Oppenheimer approx., and for the Born-Oppenheimer Hamiltonian H_{BO} we may write:

$$H_{BO}(\rho_1, \rho_2 \dots, \rho_n; \{r_i\}) = -\sum_{i=1}^{n} \frac{\hbar^2 \left|\vec{\nabla}_{\rho_i}\right|^2}{2m_e} - \sum_{i,j}^{n,N} \frac{Z_i e^2}{|\rho_i - r_j|} + \sum_{i<j}^{n} \frac{e^2}{|\rho_i - \rho_j|}, \qquad \textbf{(25)}$$

where $\hbar = h/2\pi$ is reduced Planck constant, m_e is mass of electron, n is number of electrons, N is number of ions, Z_i is nuclear charge of the ion i, e is elementary charge, ρ_i are coordinates of electrons and r_j coordinates of ions. The first sum in Hamiltonian represents kinetic energy of electrons, the second represents potential energy between ions and electrons, and the last is potential energy between electrons. Thanks to this approximation, it is possible to solve wave equation for every set of ion coordinates separately. Hamiltonian is then:

$$H = K_e + V_{ei} + V_{ee}. \qquad \textbf{(26)}$$

3.1.2 Mean-field Theory

A wavefunction $\Psi(\{\rho_i\})$ is defined in the space with dimension $3n$, where n is number of electrons. Because the complexity of such a computation task grows abowe all limits even for the small number of atoms, it is necessary to use more approximations. One of the widely used is the Mean-field theory (Self-consistent field theory). Let us assume that wavefunction $\Psi(\{\rho_i\})$ is product of all particular electron wavefunctions written as

$$\Psi(\{\rho_i\}) = \phi_1(\{\rho_1\})\, \phi_2(\{\rho_2\}) \dots \phi_n(\{\rho_n\}). \qquad \textbf{(27)}$$

This product is called Hartree product. It assumes, that there are no mutual correlations of these wavefunctions. If we substitute this to the **Equation (25)**, we get Hartree equation:

$$\left[-\frac{\hbar^2}{2m_e}\left|\vec{\nabla}\right|^2 - \sum_{i}^{N} \frac{Z_i e^2}{|r_i - \rho|} + \sum_{i \neq j}^{n} e^2 \int \frac{|\phi_i(\rho')|^2}{|\rho - \rho'|} d^3\rho'\right] \phi_j(\rho) = E'\phi_j(\rho), \qquad \textbf{(28)}$$

where $\phi_i(\{\rho'\})$ is product of all electrons wavefunctions with exception of one toward which we are performing the calculation. The term similar to Hamiltonian used here is so called effective Hamiltonian, which, among other, includes also the term for interaction (potential energy) of one electron with average wavefunction of all other electrons. It may be written as

$$\langle H\rangle = \sum_{i=1}^{n}\int d^3\rho\phi_1^*(\rho)\left[-\frac{\hbar^2|\vec{\nabla}|^2}{2m_e}-\sum_{j}^{N}\frac{Z_i e^2}{|\rho-r_j|}\right]\phi_i(\rho)+\sum_{i<j}^{n}\int d^3\rho_i d^3\rho_j\frac{e^2|\phi_i(\rho_i)|^2|\phi_j(\rho_j)|^2}{|\rho_i-\rho_j|}, \quad \textbf{(29)}$$

where total energy of the system is equal to average Hamiltonian value, and Hamiltonian depends on the wanted orbitals. In this calculation, it is not necessary to use $3n$-dimensional space as we consider all the other electrons as one with wavefunction equal to Hartree product without impact of electron for which we make the calculation. The main advantage of this approximation thus is that we need only n-times repeat the calculation in 3D space which reduces complexity significantly.

3.1.3 Including the Pauli Exclusion Principle

A problem of the mentioned model is that electrons are not interchangeable with each other. If we assume n particles which ale together forming a wavefunction and we swap positions of two arbitrary particles, the result is another wavefunction multiplied by the constant c. For all known particles in the universe this constant has value either 1 (for bosons) or -1 (for fermions).

$$\psi(\rho_1,\rho_2,\dots,\rho_i,\dots,\rho_j,\dots,\rho_n) = c\psi(\rho_1,\rho_2,\dots,\rho_j,\dots,\rho_i,\dots,\rho_n) \quad \textbf{(30)}$$

$$c=\begin{cases}1 & boson\\ -1 & fermion\end{cases}$$

Because electron is fermion, it is apparent that its wavefunction is anti-symmetric. All femnions are subject of the Pauli exclusion principle. It says that two indistinguishable fermions can not be in the same quantum state. Let us assume a wavefunction of two-electron system

$$\psi(\rho_1,\rho_2)=\phi_1(\rho_1)\phi_2(\rho_2), \quad \textbf{(31)}$$

where electron ρ_1 is on spin orbital ϕ_1 and electron ρ_2 on spin orbital ϕ_2. We introduce symmetrization of wavefunction by averaging as

$$\psi(\rho_1,\rho_2)=\frac{1}{\sqrt{2}}\big(\phi_1(\rho_1)\phi_2(\rho_2)-\phi_2(\rho_1)\phi_1(\rho_2)\big), \quad \textbf{(32)}$$

where when $\phi_1(\rho_1) = \phi_2(\rho_2)$, it means when both electrons share the same spin orbital, it the resulting wavefunction equal to zero. This is in agreement with Pauli exclusion principle. By generalizing this problem for N electrons we get Slater determinant.

$$\Psi(\rho_1,\dots,\rho_N)=\frac{1}{\sqrt{N!}}\begin{vmatrix}\phi_1(\rho_1) & \phi_2(\rho_1) & \dots & \phi_N(\rho_1)\\ \phi_1(\rho_2) & \phi_2(\rho_2) & \dots & \phi_N(\rho_2)\\ \vdots & \vdots & \vdots & \vdots\\ \phi_1(\rho_N) & \phi_2(\rho_N) & \dots & \phi_N(\rho_N)\end{vmatrix}. \quad \textbf{(33)}$$

3.1.4 Hartree-Fock

If we assume that a wavefunction of many electrons is not Hartree product but Slater determinant instead, the Pauli exclusion principle is included in the model. This model is called Hartree-Fock. If we try to solve Hartree equation **(28)** by using Slater determinant we get

$$\left[-\frac{\hbar^2|\nabla|^2}{2m_e}-\sum_i^N\frac{Z_ie^2}{|r_i-\rho|}\right]\phi_j(\rho)+\sum_i^n e\int\frac{|\phi_i(\rho')|^2\phi_j(\rho)}{|\rho-\rho'|}d^3\rho'-\sum_i^N e^2\int\frac{\phi_1^*(\rho')\phi_j(\rho')\phi_i(\rho)}{|\rho-\rho'|}d^3\rho'=E_j\phi_j(\rho) \quad \textbf{(34)}$$

where effective Hamiltonian is

$$\langle H\rangle=\sum_{i=1}^n\int d^3r\,\phi_1^*(\rho)\left[\frac{\hbar^2|\vec{\nabla}|^2}{2m_e}-\sum_j^N\frac{Z_ie^2}{|\rho-r_j|}\right]\phi_i(\rho)+\sum_{i<j}^n\int d^3\rho d^3\rho'\frac{e^2|\phi_i(\rho)|^2|\phi_j(\rho')|^2}{|\rho-\rho'|} \quad \textbf{(35)}$$
$$-\sum_{i<j}^n\int d^3\rho d^3\rho'\frac{e^2\phi_i^*(\rho)\phi_j^*(\rho')\phi_i(\rho')\phi_j(\rho)}{|\rho-\rho'|},$$

where the last sum is called exchange energy. It comes from the anti-symetric nature of electron wavefunction and has no direct physical equivalent in contrast to the other parts of Hamiltonian. There is a long list of post-Hartree-Fock methods used in today computational chemistry which are trying to improve Hartree-Fock method. A disadvantage of this method (that is the non-correlated electron wavefunction) can be solved by introducing Møller–Plesset perturbation theory, Multi-Configurational Self-Consistent Field (with or without Complete Active Space) and more into it, but at a cost of higher computational complexity.

3.1.5 Density Functional Theory

A method next to Hartree-Fock is Density functional theory (DFT). This method is based upon theorem published in year 1964 (Pierre Hohenberg and Walter Kohn) which says that wave function of electrons $\Psi_0(\rho, \rho_2, ..., \rho_n)$ in ground state is functional of electron density $n_0(\rho)$ by equation

$$n_0(\rho)=\int d^3\rho_2, d^3\rho_3, \ldots, d^3\rho_n|\Psi_0(\rho,\rho_2,\ldots,\rho_n)|^2 \quad . \quad \textbf{(36)}$$

The gound state of quantum-mechanical system is quantum state in which this system has lowest possible energy. This energy is called zero-point energy and is (like wave function) also functional of electron density. By using Dirac notation we can say

$$E_0=\langle\Psi_0[n_0]|H|\Psi_0[n_0]\rangle=E[n_0] \quad , \textbf{(37)}$$

where E_0 is zero-point energy of the system and Ψ_0 is wave function of system in ground state. Zero-point energy of system is energy which minimizes functional of energy with respect to all possible variations of electron density. Electron density which minimizes functional of energy is ground state density n_0 and is given as

$$E[n_0]\leq E[n]. \quad \textbf{(38)}$$

A wave function is defined in 3n-space where n is number of electrons, but probability density of presence of electrons is function only with dimension 3. This fact will therefore allow us to greatly reduce processing time. Total energy of system is given as

$$E[n] = T_s[n] + U_H[n] + V_{ext}[n] + E_{xc}[n], \qquad \textbf{(39)}$$

where $T_s[n]$ is kinetic energy, $U_H[n]$ is Hartree potential (interaction between electron and other electerons by Mean-Field theory), $V_{ext}[n]$ is potential energy of external fields (interaction of electron with field created by ions) and $E_{xc}[n]$ is exchange and correlation energy functional which represents any unknown interactions with system. By solving Schrödinger equation **(20)** we get

$$\left[\frac{-\hbar^2}{2m_e}|\nabla^2| + v_{ext}(\rho) + v_H(\rho) + v_{xc}(\rho)\right]\phi_i = \varepsilon_i \phi_i \quad , \quad \textbf{(40)}$$

where $v_{xc}(\rho)$ is exchange and correlation potential and

$$n(\rho) = \sum |\phi_i(\rho)|^2 \quad , \qquad \textbf{(41)}$$

is electron density. These two equations are called Kohn-Sham equations and it is, similarly to Hartree-Fock, solving of one-particle time-independent Schrödinger equation. A drowback of this model is expression of $v_{xc}(\rho)$. The heart of the problem is therefore reduced to solving the exchange and correlation energy functional which can be further divided into exchange energy functional and correlation energy functional like

$$E_{xc}[n] = E_x[n] + E_c[n], \qquad \textbf{(42)}$$

and may be approximated by several methods. One of the widely used methods is Local density approximation (LDA) where functional of exchange energy is given by equations for non-interacting homogenious electron gas

$$E_{x,hom}(n) = \frac{-3q^2}{4}\left(\frac{3}{\pi}\right)^{1/3} n^{4/3} \quad , \qquad \textbf{(43)}$$

and

$$E_{x,LDA}[n(\rho)] = \frac{-3q^2}{4}\left(\frac{3}{\pi}\right)^{1/3} \int d^3\rho\, n(\rho)^{4/3} \quad , \qquad \textbf{(44)}$$

where $q = \sqrt{4\pi\epsilon_0 \hbar c}$ is Planck charge.

The correlation energy functional is not yet analytically solved, however D. M. Ceperley and B. J. Alder published in year 1980 numerical simulation based on Quantum Monte Carlo method. A drowback of LDA is inaccurate results for quick spatial changes of electron density. In case of systems where this may occure, Generalized Gradient Approximation is used. It works on the same basis like LDA, however in this case we suppose that exchange and correlation energy functional is dependent not only on electron density but as well on it's gradient like

$$E_{xc,GGA}[n(\rho)] = \int d^3 \rho \, e_{xc,GGA}(n(\rho), \nabla n(\rho)) \quad . \quad \textbf{(45)}$$

This method can reduce inaccuracy however for the price of greater computing demands. Solving DFT numerically is still relatively computing challenge therefore there are used many approximations including pseudopotentials (where electrons near atomic core are not included in computing because they are not get involved to interactions between valence electrons), and using points of high symmetry in reciprocal space. DFT is intensively improved because of the wide use. Some new extents are PBE (Perdew, Burke, Ernzerhof, 1996), BLYP (Becke's exchange + Lee, Yang and Parr, 1988) or B3LYP (combination with semi-empirical models through hybrid functional, hyper-GGA). For simulation of nanostructures the Hartree-Fock and DFT methods are neccessary. Inaccurate results are in structures with infinitesimal number of states near Fermi energy level.

3.2 Quantum-level Simulation of Current

This chapter deals with method used for simulation of quantum transport of current in nanostructures. When we are simulating electronic devices the size plays the key role. As it is shown on the **Figure 13**, generally we can use diffusion model while modeling systems around units to hundreds of micrometers. The path of electrons, carrying quantum of charge, is disturbed by scattering mechanisms (collisions with ions and defects of crystal lattice).

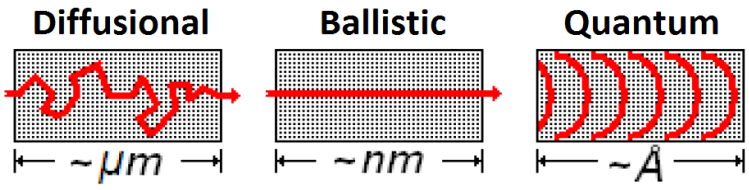

Figure 13. Three types of electron transport sorted by spatial scale.

As it is described in [18], electrons do not collide with ions in case of structures on the nanometer scale. This is called ballistic transport. It is possible to achieve this type of transport by specific conditions even in the larger (two-dimensional) structures (e.g. graphene). The diffusion transport is in fact composed of short sections of the ballistic transport which is disturbed by collisions and scattering. The ballistic transport may be described by Boltzmann transport equation and by the means of statistical mechanics. On the larger scale the quantum interference effects cancel each other out by mechanism of dephasing. Similarly, the ballistic transport is result of interference effects coming from the wave character of electrons. If we have a structure with size comparable to atom diameters (tenths of nanometer) it is neccessary to include this to the model.

3.2.1 Quantum Theory of Conductivity

In general, we can divide a structure by grid in to specific number of points. Let us assume electrodes *S* and *D* (Source and Drain) connected to channel *Ch* formed only by one grid point (**Figure 14**). At this point of grid, we are able to describe the transport in the channel by means of allowed energy levels. Every level indicates an allowed state in which the electron can be present. Let us assume the equilibrium state and thermodynamic temperature 0 K, and let us assume as well that the channel will behave like a perfectly isolated quantum system (no interaction with surroundings). From the theory of conductance it is clear that (at 0 K) the allowed energy levels under Fermi level will be all occupied

and allowed energy levels above Fermi level will be all unoccupied. For another simplification let us assume that electrodes *S* and *D* are large enough and have continuous functions of density of states so we have sufficiency of electrons for transport from occupied levels in the first electrode in to the empty states of the second electrode.

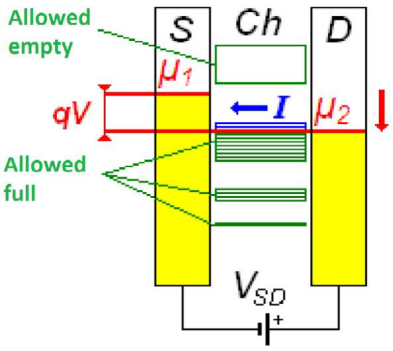

Figure 14. The transport of current in a structure with one grid point without the effect of electrodes.

When applying a small voltage, the channel *Ch* is conducting only if there are any available allowed energy levels (empty or filled by electrons) within the range of electrochemical potentials. The applied voltage creates a difference in electrochemical potentials

$$\mu_1 - \mu_2 = qV \,, q = \sqrt{4\pi\epsilon_0 \hbar c} \quad , \qquad \textbf{(46)}$$

where q is Planck charge and $V = V_{SD}$ is the applied voltage. Current I is flowing through structure on the **Figure 14** because electrons from electrode *S* (with electrochemical potential μ_1) are filling empty states in channel *Ch* which are created by moving electrons from filled states into lower energy levels in electrode *D* (with electrochemical potential μ_2). Every allowed energy level in between electrochemical potentials will participate in transport of the current.

3.2.2 Simplified Quantitative Model

In previous text we had to make simplification which ignores most of the quantum mechanics. Let us have a structure which is perfectly isolated from its environment and has an allowed energy level. Then value of this energy level will be sharply defined. However, the uncertainity principle will apply when we connect this structure to electrodes, because electron is in this quantum state (which is corresponding to the allowed energy level) only for a limited time. The result is that the connection of electrodes will cause broadening of this energy level and we are further describing it as a density of states $D(E)$.

Let us assume structure on the **Figure 15**. It is a simplified two-electrode system with only one grid point as a channel. We have two electrodes *S* and *D* with different electrochemical potentials. There is a channel with density of stated $D(E - U)$ in between electrodes, where U is sum of effects of the external potential fields on the channel energy levels. The density of states is therefore dependent not only on the energy E but also on applied voltage V_{SD}. The shift of energy levels in the channel (red arrow in the **Figure 14**) can be prevented by using a biased gate electrode.

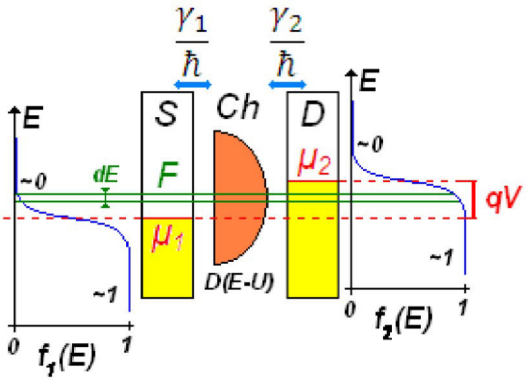

Figure 15. The current transport at $T = 0$ K for one grid point system.

As it is described in the **Figure 15**, Fermi functions $f_1(E)$ and $f_2(E)$ are (for $T > 0$ K) continuous graphs (blue in **Figure 15**) and their values are in interval <0,1>. Let us define $\gamma_i/\hbar$ as escape rate of electrons between an electrode and channel. This quantity represents quality of electrode connection to channel. The dimension of $\gamma_i/\hbar$ is $[s^{-1}]$ therefore γ_i has dimension of energy. Let us introduce the factor of occupation $F \in <0,1>$ for element of energy dE in channel. For a current between electrode S and channel we can say

$$I_1 = q\frac{\gamma_1}{\hbar} dE D(E)[F - f_1] \quad , \textbf{(47)}$$

and similarly for a current between channel and electrode D

$$I_2 = q\frac{\gamma_2}{\hbar} dE D(E)[f_2 - F] \quad . \textbf{(48)}$$

For simplification let us assume that $\gamma = \gamma_1 = \gamma_2$. From the assumption of thermodynamical equilibrium it follows that current I_1 flowing into channel will be equal to current I_2 flowing from the channel, therefore

$$F - f_1 = f_2 - F \quad \Rightarrow \quad F - f_1 = \frac{f_2 - f_1}{2} \quad , \textbf{(49)}$$

and for total current I through channel

$$I = \frac{q}{\hbar}\int dE T(E)[f_2 - f_1] \quad , \textbf{(50)}$$

where

$$T(E) = \frac{K(E)}{2} \equiv \pi D(E)\gamma \quad \textbf{(51)}$$

is transmission.

3.2.3 Diffusional and Ballistic Transport

Until now we presumed a channel formed only by one grid point. For generalization of this model for arbitrary number of grid points we will approach from the channel with two grid points as in **Figure 16**.

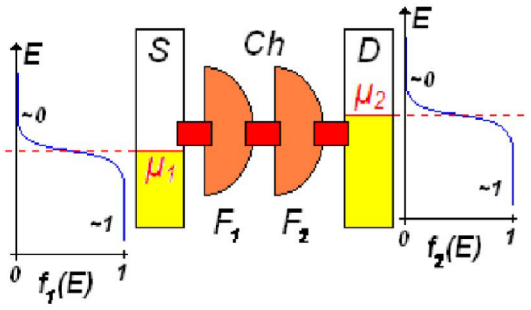

Figure 16. A system consisting of two grid points and two electrodes.

In this case we have three interfaces and we need to define factor of occupation F_1 and F_2 for both grid points. For the currents through interfaces it stands

$$I_1 = K(E)[F_1 - f_1], I_{12} = K(E)[F_1 - F_2], I_2 = K(E)[f_2 - F_2] \quad . \textbf{(52)}$$

From the presumption of steady state (thermodynamical equilibrium) it follows $I_1 = I_{12} = I_2$ and therefore

$$F_1 - f_1 = F_1 - F_2 = f_2 - F_2 \quad \Rightarrow \quad F_1 - f_1 = \frac{f_2 - f_1}{3} \quad . \textbf{(53)}$$

For total current we can say

$$I = \frac{K(E)}{3}[f_2 - f_1] \quad . \textbf{(54)}$$

For explanation of diffusion transport by means of this model we can use analogy with Ohm's law $I = GU$. Let us have $K(E)$ corresponding to conductivity G and values of occupation factors F_1, F_2 and Fermi functions f_1 and f_2 corresponding to voltage U. Let us assume steady state where conductivity of particular interfaces are identical. It is clear that for one grid point the resulting current will be given by sum of two conductivities $G/2$, this corresponds with the factor $K(E)/2$ for structure with one grid point. Similarly, for a structure with two grid points (three interfaces) we get conductivity $G/3$ which corresponds with factor $K(E)/3$. As seen, this model describes diffusion transport in which we expect the resistance for serially connected grid points to be bigger than for one grid point. This approach is expression of classical diffusion formula $I \sim \partial F / \partial z$ for discretized space variable z.

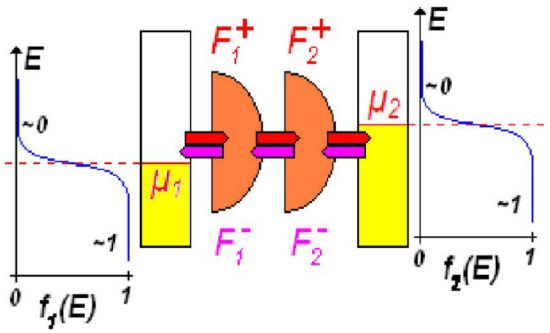

Figure 17. Clarification to diffusional and ballistic transport chapter.

In order to include diffusional and ballistic transport in to this model we use following consideration. Let us assume system with two grid points (**Figure 17**). In contrast to previous description we have two quantities of occupation factor F_i^+ and F_i^- for description of the state of electrons in every grid point. F_i^+ corresponds to occupation factor of states for electrons moving right and F_i^- corresponds to occupation factor of states for electrons moving left. For both currents we can say

$$I_1^+ = \frac{K(E)}{2}F_1^+, \qquad I_1^- = \frac{K(E)}{2}F_1^-, \qquad I_2^+ = \frac{K(E)}{2}F_2^+, \qquad I_2^- = \frac{K(E)}{2}F_2^-. \tag{55}$$

Assuming the condition that electrons will be not scattered in between grid points we can write

$$f_1 = F_1^+ = F_2^+, \; F_1^- = F_1^- = f_2. \tag{56}$$

We can get total current by subtracting left directing curents from right directing currents

$$I = \frac{q}{\hbar}\int dE \frac{K(E)}{2}[f_2 - f_1] \quad , \tag{57}$$

which is the same result as for the current through one grid point. This behaviour of grid points corresponds to regime of ballistic transport where resistance of all channel is given by resistance of one grid point. Let us introduce parameter of backscattering $b \in \langle 0, 1 \rangle$ and let us assume that certaint number of electrons will change direction to the opposite when flowing through channel. We can derive

$$I_2^+ = (1 - b)I_1^+ + bI_2^- \Rightarrow F_2^+ = (1 - b)f_1 + bf_2, \tag{58}$$

$$I_1^- = (1 - b)I_2^- + bI_1^+ \Rightarrow F_1^- = (1 - b)f_2 + bf_1, \tag{59}$$

which gives total current

$$I = \frac{K(E)}{2}(1-b)[f_2 - f_1] \quad . \tag{60}$$

It can be derived that for the small b and for $n + 1$ sections we can say

$$I = \frac{K(E)}{2} \frac{1}{1+nb} [f_2 - f_1] \quad . \qquad \textbf{(61)}$$

If the parameter $b = 0$, it will be ballistic transport. If the parameter $b = 1/2$ it is diffusive transport. By means of parameter b we can therefore continuously change between ballistic and diffusion transport. This model is discretization of more general equations for current transport

$$\frac{\partial I^+}{\partial z} = -\beta I^+ - \beta I^-, \qquad \frac{\partial I^-}{\partial z} = \beta I^+ + \beta I^-, \qquad \textbf{(62)}$$

where $\beta \in \langle 0,1 \rangle$ corresponds to part of electrons which change direction in channel to opposite. In general form we can write diffusion and ballistic transport of current by means of Boltzmann transport equation as

$$\frac{\partial I(\vec{k})}{\partial z} = \int d\vec{k} \left(S(\vec{k}, \vec{k}\,') I(\vec{k}\,') - S(\vec{k}\,', \vec{k}) I(\vec{k}) \right), \qquad \textbf{(63)}$$

where we assume current I as dependent on vector $\vec{k}$.

3.2.4 Coherent Quantum Transport

In the previous text we presumed that transport of current proceeds on the basis of diffusive and ballistic mechanisms. Let us, however, assume a structure which characteristic dimension is comparable to atoms. Here we need to include effects of quantum interference. It was stated that in case of diffusive transport we can use Ohm's Law for adding conductances of particular grid points. In the case of ballistic transport, the total conductance is given by conductance of one grid point. Finally, in the case of quantum transport, the adding and subtracting of waves can give us unpredicted result (by means of constructive or destructive interference) as is higher conductivity for a structure with more serial grid points than for the one grid point structure. To include this effect to our model we have to use Schrödinger equation. At first we use system with one grid point and let us neglect the effect of electrodes on energy levels (**Figure 14**). Then we can write

$$E\psi_1 = \varepsilon \psi_1 \quad \Rightarrow \quad [E - \varepsilon]\psi_1 = 0 \quad , \qquad \textbf{(64)}$$

where ε stands for energy level of grid point and E is the total energy of system. If we include the effect of electrodes (**Figure 15**) we can write for time-independent Schrödinger equation

$$[E - \varepsilon + \frac{i\gamma_1}{2} + \frac{i\gamma_2}{2}]\psi_1 = 0 \quad , \qquad \textbf{(65)}$$

and for the time-dependent Schrödinger equation

$$[i\hbar \frac{d}{dt} - \varepsilon + \frac{i\gamma_1}{2} + \frac{i\gamma_2}{2}]\psi_1 = 0 \quad , \qquad \textbf{(66)}$$

where t is time and i is imaginary unit. For the wave function of electron in the structure with one grid point we can write

$$\psi_1 = e^{\frac{-i\varepsilon t}{\hbar}} . e^{\frac{-i\gamma_1 t}{2\hbar}} . e^{\frac{-i\gamma_2 t}{2\hbar}} \quad , \qquad \textbf{(67)}$$

and for electron density

$$n_1 = \psi_1 \psi_1^* = e^{\frac{-\gamma_1 t}{\hbar}} \cdot e^{\frac{-\gamma_2 t}{\hbar}} . \qquad \textbf{(68)}$$

After adding of source s_2 function to Sch. equation we get

$$[E - \varepsilon + \frac{i\gamma_1}{2} + \frac{i\gamma_2}{2}]\psi_1 = s_2 \quad , \qquad \textbf{(69)}$$

where

$$s_2 s_2^* = \gamma_2 f_2, \qquad \textbf{(70)}$$

for wave function we get

$$\psi_1 = \frac{s_2}{E - \varepsilon + \frac{i\gamma_1}{2} + \frac{i\gamma_2}{2}} \quad , \qquad \textbf{(71)}$$

and for electron density we get

$$n_1(E) = \frac{\gamma_2 f_2}{(E-\varepsilon)^2 + \left(\frac{\gamma_1}{2} + \frac{\gamma_2}{2}\right)^2} \quad , \qquad \textbf{(72)}$$

By integration of electron density we get total number of electrons

$$N_1 = \int \frac{dE}{2\pi} n_1(E) = \frac{\gamma_2 f_2}{\gamma_1 + \gamma_2} \quad . \qquad \textbf{(73)}$$

Let us assume source s_1 and s_2 from both electrodes. Wavefunctions induced by non-correlated sources is not possible to add but we can write the electron density like

$$n_1(E) = \frac{s_2 s_2^* + s_1 s_1^*}{(E-\varepsilon)^2 + \left(\frac{\gamma_1}{2} + \frac{\gamma_2}{2}\right)^2} \quad , \textbf{(74)}$$

and total number of electrons as

$$N_1 = \int \frac{dE}{2\pi} n_1(E) = \frac{\gamma_2 f_2 + \gamma_1 f_1}{\gamma_1 + \gamma_2} \quad , \textbf{(75)}$$

Considering structure with two grid points as an isolated system without the electrode effect we can write Schrödinger equation as follows

$$E\begin{Bmatrix}\psi_1\\ \psi_2\end{Bmatrix}=\begin{bmatrix}\varepsilon_1 & t\\ t & \varepsilon_2\end{bmatrix}\begin{Bmatrix}\psi_1\\ \psi_2\end{Bmatrix}\Rightarrow\begin{bmatrix}E-\varepsilon_1 & -t\\ -t & E-\varepsilon_2\end{bmatrix}\begin{Bmatrix}\psi_1\\ \psi_2\end{Bmatrix}=\begin{Bmatrix}0\\ 0\end{Bmatrix}, \quad \textbf{(76)}$$

where t is coupling between energy levels ε_i of particular grid points which is mediating the quantum interference effects. Let us assume zero input from source $s_1 = 0$ and non-zero input from source $s_2 \neq 0$, then

$$\begin{bmatrix}E-\varepsilon_1+\frac{i\gamma_1}{2} & -t\\ -t & E-\varepsilon_2+\frac{i\gamma_2}{2}\end{bmatrix}\begin{Bmatrix}\psi_1\\ \psi_2\end{Bmatrix}=\begin{Bmatrix}0\\ s_2\end{Bmatrix}. \quad \textbf{(77)}$$

Similarly let us assume a structure with arbitrary number N of grid points. Then the Sch. equation for zero input and without effect of electrodes is

$$E\Psi = \mathrm{H}\Psi \Rightarrow [EI - \mathrm{H}]\Psi = 0, \quad \textbf{(78)}$$

where I is identity matrix N x N, H is Hamilton operator of dimension N x N, E is eigenvalue matrix N x N and Ψ is column vector of wave functions. When we use input from right electrode by means of column vector S_2, we can write

$$[EI - \mathrm{H} - \Sigma_1 - \Sigma_2]\Psi = S_2, \quad \textbf{(79)}$$

where

$$\{S_2\} = \begin{Bmatrix}0\\ \vdots\\ s_2\end{Bmatrix}, \quad \textbf{(80)}$$

is column vector which stands for input and has all elements zero but the last, because we expect that input (second electrode) is connected only to the last grid point of the channel. Matrices Σ_1 and Σ_2 represent properties of the connection to electrodes and we can write for them

$$\Sigma_1 = \begin{bmatrix}-\frac{i\gamma_1}{2} & 0 & \cdots & 0\\ 0 & \vdots & \cdots & \vdots\\ \vdots & \vdots & \cdots & \vdots\\ 0 & \cdots & \cdots & 0\end{bmatrix}, \quad \Sigma_2 = \begin{bmatrix}0 & \cdots & \cdots & 0\\ \vdots & \cdots & \vdots & \vdots\\ \vdots & \cdots & \vdots & 0\\ 0 & \cdots & 0 & -\frac{i\gamma_2}{2}\end{bmatrix}, \quad \textbf{(81)}$$

and they are called self-energy matrices. Only the element $\Sigma_1(1, 1)$ or the element $\Sigma_2(N, N)$ is non-zero. This is because of fact that only the first grid point of the channel is connected to the first electrode and only the last grid point of the channel is connected to the second electrode. We can also write the matrix version of γ_1 and γ_2 as anti-hermitian part of Σ_1 and Σ_2 respectively

$$\Gamma_1 = i[\Sigma_1 - \Sigma_1^+], \quad \Gamma_2 = i[\Sigma_2 - \Sigma_2^+], \quad \textbf{(82)}$$

where Γ_1 and Γ_2 are broadening matrices. Plus in the upper index denotes Hermitian adjoint. Let us introduce retarded Green's function G as

$$G = [EI - \mathrm{H} - \Sigma_1 - \Sigma_2]^{-1}, \quad \textbf{(83)}$$

This function represents wave function which we get when the system is excited by unit source, it is therefore impulse response of the system. Let us introduce correlation function G^n as

$$G^n(\equiv -iG^<) = \{\Psi\}\{\Psi\}^+ = \begin{Bmatrix}\psi_1 \\ \vdots \\ \psi_N\end{Bmatrix}\{\psi_1^* \quad \cdots \quad \psi_N^*\} = \begin{bmatrix}\psi_1\psi_1^* & \cdots & \psi_1\psi_N^* \\ \vdots & \cdots & \vdots \\ \psi_N\psi_1^* & \cdots & \psi_N\psi_N^*\end{bmatrix}. \quad \textbf{(84)}$$

The diagonal elements of this correlation function corresponds to electron density. The out of diagonal elements correspond to correlation of wave functions in between two different grid points. By substituting column vector of wavefunction Ψ by Green's function G and by column vector of input S_2 we get

$$G^n = \Psi\,\Psi^+ = GS_2S_2^+G^+, \quad \textbf{(85)}$$

Because the power of the source is

$$S_2S_2^+ = \Gamma_2 f_2, \quad \textbf{(86)}$$

we can write that

$$G^n = G\Gamma_2G^+f_2 + G\Gamma_1G^+f_1, \quad \textbf{(87)}$$

The advance of introduced correlation function is that we can superpose the contribution of more sources in this function. If we need matrix representation of total density of states we can simply lay $f_i = 1$ (all allowed states are occupied) and we can write

$$A = G\Gamma_2G^+ + G\Gamma_1G^+ = i[G - G^+], \quad \textbf{(88)}$$

where matrix A is spectral function. The spectral function is, in some sense, showing the total number of states through total density of allowed states. The diagonal elements of G^n matrix on the other hand represent their occupation through electron density. The spectral function can be measured directly by means of the scanning tunneling microscope. For situation with N grid points, the measured tunneling current at particular grid point is proportional to the value of spectral function diagonal element $A(i, i)$ in the vicinity of energy corresponding to electrochemical potential. This diagonal element is called local density of states (LDOS). In case of structure with two grid points we can express the current flowing through interface of the first electrode and first grid point as

$$I_1/(q/\hbar) = \mathrm{Tr}([\Gamma_1A]f_1 - [\Gamma_1G^n]), \quad \textbf{(89)}$$

and current flowing through interface of the second grid point and the second electrode as

$$I_2/(q/\hbar) = \mathrm{Tr}([\Gamma_2A]f_2 - [\Gamma_2G^n]), \quad \textbf{(90)}$$

where $\mathrm{Tr}(A)$ is trace of matrix A. These equations for current apply generally even for non-coherent transport (with scattering effects). In the special case of coherent transport we can write the transmission of two-grid points structure as follows

$$T'(E) = \mathrm{Tr}[\Gamma_1G\Gamma_2G^+]), \quad \textbf{(91)}$$

and for current of two-grid points structure in case of coherent transport we can say

$$I = \frac{q}{\hbar}\int dE\, T'(E)[f_2 - f_1], \quad \textbf{(92)}$$

where $T'(E)$ stands for effective transmission for which in case of coherent transport apply

$$T'(E) = T(E). \quad \textbf{(93)}$$

3.2.5 Spin and Transformation of Bases

To as well include spin of the electron it is possible to use following reasoning. Let us assume a structure with one grid point. Let us also assume that along both electrodes acts an magnetic field on the channel (**Figure 18**). The original energy level ε splits in two different levels $\varepsilon + t$ and $\varepsilon - t$, therefore we get two-dimensional Hamiltonian

$$H = \begin{bmatrix} \varepsilon + t & 0 \\ 0 & \varepsilon - t \end{bmatrix}, \quad \textbf{(94)}$$

which is the same Hamiltonian as for structure with two grid points. Spin UP can flow only through left electrode and spin down only through right electrode. For self-energy matrices we get

$$\Sigma_1 = -i\frac{\gamma_1}{2}\begin{bmatrix} 1 & 0 \\ 0 & 0 \end{bmatrix}, \qquad \Sigma_2 = -i\frac{\gamma_2}{2}\begin{bmatrix} 0 & 0 \\ 0 & 1 \end{bmatrix}. \quad \textbf{(95)}$$

Problem is that while Hamiltonian is expressed in one basis, the self-energy matrices are expressed in another basis. Let us place the structure into orthogonal coordinates x, z as in **Figure 18**.

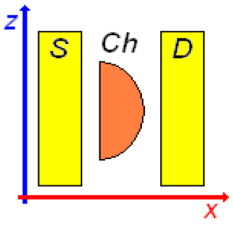

Figure 18. To the explanation of basis transformations.

The orientation of states in the channel described by Hamiltonian corresponds to movement of electrons from one electrode to another, therefore in direction of x axis. Basis of this matrix is therefore with orientation "left-right". The magnetic field which causes broadening of states is oriented along electrodes, perpendicular to the channel and therefore in direction of z axis. Basis of this matrix is therefore with orientation "up-down". We need to have all matrices in the same basis and therefore transform the first matrix to basis "up-down" or the second to basis "left-right". Let us assume spin UP spinor in orthogonal coordinates with vertical axis z and horizontal axis x having components $\cos(\theta/2)$ and $\sin(\theta/2)$ and spin DOWN spinor having components $-\sin(\theta/2)$ and $\cos(\theta/2)$, then (by substituting appropriate θ) we get spinor components in z direction

$$\theta = 0: \begin{Bmatrix} 1 \\ 0 \end{Bmatrix} \text{ for „UP“ and } \begin{Bmatrix} 0 \\ 1 \end{Bmatrix} \text{ for „DOWN“}, \quad \textbf{(96)}$$

and spinor components in x direction

$$\theta = \frac{\pi}{2}: \begin{Bmatrix}+1\\+1\end{Bmatrix} \text{ for „UP“ and } \begin{Bmatrix}+1\\-1\end{Bmatrix} \text{ for „DOWN“.} \qquad \textbf{(97)}$$

These column vectors are together giving matrix of transformation to transform either Hamiltonian basis from "left-right" basis to "up-down" basis resulting in

$$H = \begin{bmatrix}\varepsilon & t\\ t & \varepsilon\end{bmatrix}, \qquad \textbf{(98)}$$

or basis of self-energy matrices from "up-down" to "left-right" basis resulting in

$$\Sigma_1 = -i\frac{\gamma_1}{2}\begin{bmatrix}0{,}5 & 0{,}5\\ 0{,}5 & 0{,}5\end{bmatrix}, \qquad \Sigma_2 = -i\frac{\gamma_2}{2}\begin{bmatrix}0{,}5 & -0{,}5\\ -0{,}5 & 0{,}5\end{bmatrix}. \qquad \textbf{(99)}$$

By using the same approach we can transform basis of respective matrices in order to describe quantum interference by means of bonding and anti-bonding orbitals.

3.2.6 United Restricted Non-coherent Quantum Transport

As it was mentioned earlier in this chapter, the quantum interference effects cease to be substantial over larger distances because of dephasing. The cause of this effect is that possitions of atoms change by random fluctuations and therefore the channel is very variable environment for an electron, where in one moment the wave function is given by constructive interference and next time by destructive. Until now we discussed coherent transport through the channel. For the non-coherent transport (with dephasing) we consider a general structure at **Figure 19**.

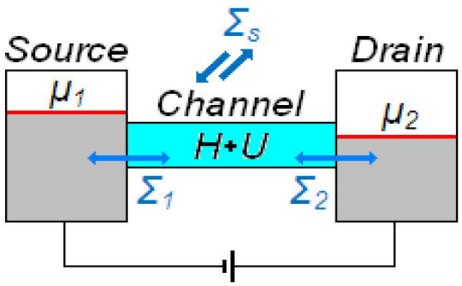

Figure 19. A general quantum structure with two electrodes and voltage source.

We will introduce simple model for dephasing where we will presume Σ_S to be acting like an another fictive electrode. An electron which is leaving the channel can go back to the system by means of this fictive electrode and to have random properties. After modification of non-equilibrium Green's function defined as

$$G = [EI - \mathrm{H} - \Sigma_1 - \Sigma_2 - \Sigma_S]^{-1}, \qquad \textbf{(100)}$$

we get

$$G^n = G\Gamma_2 G^+ f_2 + G\Gamma_1 G^+ f_1 + G\Sigma_S{}^{in} G^+, \qquad \textbf{(101)}$$

where $G\Sigma_S^{in}G^+$ is electron density of electrons re-injected back to channel. Let us introduce constant D as

$$\Sigma_S = DG \text{ and } \Sigma_S^{in} = DG^n. \quad \textbf{(102)}$$

For $D = 0$ we get

$$\Sigma_S = 0 \text{ and } \Sigma_S^{in} = 0, \quad \textbf{(103)}$$

therefore transport changes to coherent. When $D > 0$ then transport changes to non-coherent. More effective dephasing proces gives higher value of D. This simple model does not include elasticity of proces because it presumes that electron which left system is returning back with the same energy and it is only special case.

3.2.7 Unrestricted Model and Introduction to Fock space

The above mentioned approach does not describes all effects (e. g. Coulombic blockade) and therefore it is called "restricted" model. In unrestricted model we include shift of energy levels due to occupation/non-occupation by electrons. While this model is giving us (expected) gradual I-V characteristics, the exact energy of each step is not corresponding with the real case. Therefore there is need to use fermionic Fock space, which is mathematical representation of fermions behavior. It is formed by binary expressed electron states and by transitions in between these states. For example system with two energy levels will have allowed states 00, 01, 10 and 11. In the equilibrium, all electrons will fall into state 00 and nothing more happens. If there is a difference in electrochemical potential of electrodes, it depends, if it's span involves both free levels in the channel (then it can be in random state) or only one free level (then system cannot be in state 11). This adition to unrestricted model will give us gradual I-V curves in match with an experiment. More details on this topic can be found in [13].

4 Synopsys QuantumATK Simulation Software

In our simulations we used Synopsys QuantumATK simulation software [14]. Quantum ATK (Atomistix ToolKit) is commercial continuation of TranSIESTA-C which is based on technologies, models and algorithm produced in academic codes TranSIESTA and McDCal. It is combining DFT and NEGF for *ab initio* and semi-empirical calculations of structure and electron transport in systems like electrode-nanostructure-electrode, molecule, and periodic structures like crystal or nanotube. Software is operated by graphic user interface and it supports scripting environment based on Python (like NanoLanguage). Today, it is integrated with other quantum and mesoscopic simulation codes. Among the most important functions of this software is transport properties calculation (including spin-polarization) in two-electrode configuration with bias voltage, calculation of energy spectra, wave functions, electron densities, atomic forces, effective potentials and another properties of nanostructures. It supports optimization of geometry by several algorithms and modeling of macromolecular dynamics. We used methods described in more detail in literature [15, 16, 17]. The simulation method parameters are provided along with the simulation results.

5 Simulations of Carbon-based Nanostructures

After being pioneered by Geim and Novoselov [18], graphene became a valuable source of materials for nanotechnology and nanoelectronics. From bulk materials to molecular-level structures, the number of possible applications, as they were gathered e.g. in [19], is staggering. In recent decades the bottom-up approach was utilized to synthesize molecular based nanostructures and allowed for the study of nanographenes and even much more complex molecular systems [20, 21, 22]. The advances in chemical synthesis also allow to functionalize certain molecules and use them as precursors to build more complex molecular systems as explored e.g. in [23] with cyano groups. The atomically precise bottom-up fabrication of GNRs [24] has been developed, integrated circuits based on conjugated polymer monolayers were introduced [25], and self-assembly pathways for complex multicomponent structures were sketched [6]. The development in this field also inspired the old research of acenes, helicenes and other polycyclic aromatic hydrocarbons to rise again.

5.1 Graphene

Graphene (**Figure 20a**) is monolayer material with single-atom thickness composed of hexagonally oriented carbon atoms. It has many interesting properties, depending on its morphology and atomic structure. Notable properties are massless Dirac electronic structure, anomalous quantum Hall effect, high electron mobility, high thermal conductivity, stiffness and strength [18, 19]. Next to morphology and atomic structure, the properties and specific behaviour can be modified by interior and exterior doping effects from defects, molecular adsorptions (e.g. hydrogenation, oxidation), electromagnetic fields or mechanical stress. The bulk graphene sheet is semi-metal with linear dispersion around the Dirac point. However when one of the in-plane dimensions reduces below 20 nm while maintaining the other dimension, the graphene ribbon features an edge-dependent electronic structure due to the quantum confinement lattice symmetry. Armchair-edged graphene nanoribbons (AGNR) have width-dependent energy gaps, while a zigzag-edged nanoribbons (ZGNR) are always metallic with a localized state at the edge when the spin is unpolarized. This unique structure-property relationship suggests that by simple geometrical tailoring we can realize effective modification of graphene properties.

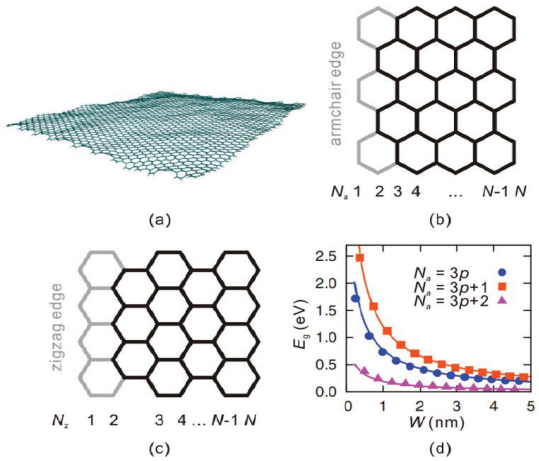

Figure 20. a) Graphene membrane. **b)** and **c)** Atomic structures of armchair and zigzag GNRs. **d)** Bandgap of armchair graphene nanoribbons (AGNR) calculated from density functional theory. The image is taken from [26].

As illustrated in the **Figure 20b**, width of AGNR structure can be denoted by the number N_a (although, several other definitions are also used). Tight-binding analysis shows that when N_a is $3p$+2 (where p is positive integer), the AGNR is metallic. While when N_a is $3p$ or $3p$+1, the bandgap of AGNR is inversely proportional to its width ($E_{g(3p)} \geq E_{g(3p+1)}$). Similar results are obtained by density functional theory (DFT) calculations based on local density approximation (LDA) with only difference that the reconstruction of structure and electron density at ribbon edge opens small gap for $N_a = 3p + 2$, and decreases (increases) the gaps of $3p$ ($3p + 1$) AGNRs. The structure of ZGNR is shown in the **Figure 20c**. Simple analysis from the tight-binding picture predicts that the spin-unpolarized eigenstates of ZGNRs near Fermi energy E_F have a peculiar edge-state structure. There are two edge states decaying into the center of ZGNRs with a profile depending on their momentum. This can be seen from the center of ZGNRs and it is shown in the flat bands for $k > 2\pi/3$, which give rise to a very large density of states at E_F and infinitesimally small on-site repulsion, could make the ZGNRs magnetic. Furthermore when a transverse electric field is applied, an energy gap is opened for one spin channel while the other remains metallic [18, 19, 26].

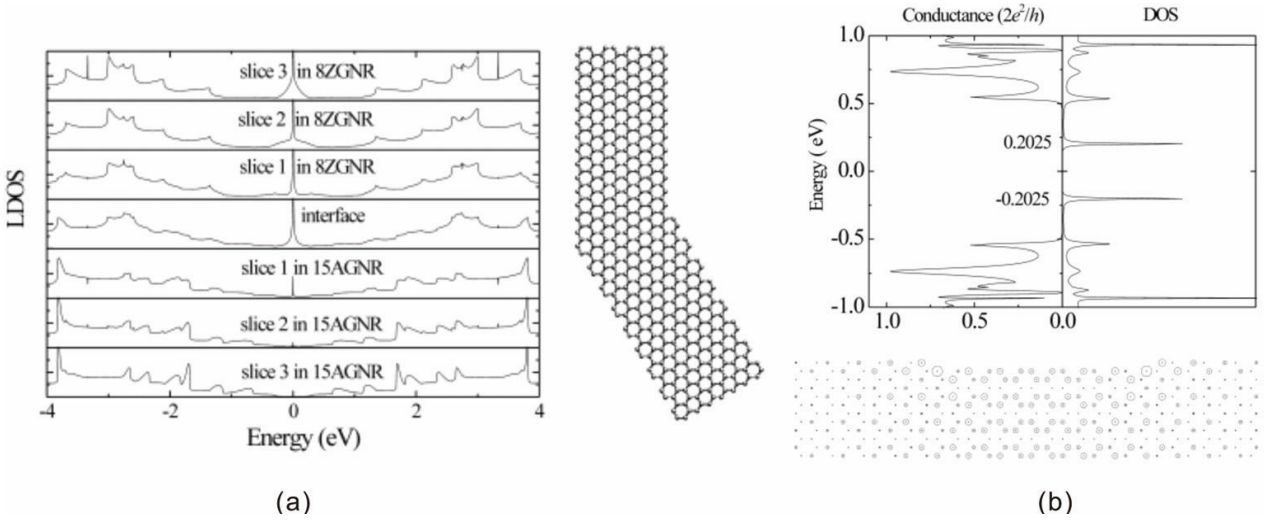

Figure 21. GNR junction-based building blocks for nanoelectronics: **a)** a junction connecting metallic ZGNRs and semiconducting AGNRs forms Schottky barrier at the interface. **b)** sandwich AGNR structure with varying width behaves as a quantum dot, the energy levels are tunable through varying the width of the central GNR. The image is taken from [26].

The bandgap E_g shows no direct dependence on the crystallographic direction and during the fabrication process or during the self-passivating process after the structure is formed, the edge shape (armchair or zigzag) can reconstruct and this may cause the bandgap to appear for graphene nanoribbons with any crystalline orientation. Elementary building blocks for nanoelectronics, such as metal/semiconductor junctions and quantum dots, thus can be constructed through a combination of structural patterns of graphene nanoribbons. A junction combining metallic and semiconducting GNRs is easy in principle (**Figure 21a**). A sandwich structure (**Figure 21b**) behaves as quantum dots with tunable energy levels. The finite-sized graphene nanodisc is another graphene derivative containing close edges with similar electronic structure as GNRs. The triangular zigzag nanodisc can be interpretated as a quantum dot with an internal degree of freedom. Its ground state is a quasi-ferromagnet, which is a ferromagnetic-like state with a finite (but very long) lifetime. A combined system, including nanodiscs and leads, can find applications in spin filters, amplifiers and diodes. The arbitrarily shaped graphene nanoflakes can exhibit shape dependence of magnetic properties and are interesting for spintronic nanoscale devices made by sculpting graphene fragments. Other nanostructures such as twists and scrolls also have interesting electronic properties and potential applications.

In his work, J. E. Anthony provides a detailed outlook on the application of acenes in the field of organic electronics [27]. The larger acenes (and other large conjugated systems as well [28]) are subject of study as a potential replacement for inorganic semiconductors which is expected to reduce the manufacturing cost and allow fabrication of devices on lightweight and flexible substrates. The prospect is to use soluble inks which may be deposited and patterned by a number of printing techniques [29], but also organized molecule-level systems has been studied [30]. Several recent works provide a proof that [*n*]acene may be synthesized at least to $n = 10$. Zuzak et al. generated nonacene by on-suface dehydrogenation [31], and Krüger et al. used on-surface assisted reduction of tetraepoxy decacene on Au(111) to produce decacene [32]. The experiments show that acenes larger than $n = 6$ are increasingly reactive with *n*, dimerise in air conditions and feasible way to isolate them is as crystalline solids [27, 33].

The larger acenes are also building blocks of carbon nanotubes and graphene and thus responsible for its electronic properties. In this work, we use acenes as a building block of ZGNRs. Theoretical study by Wu et al. provides detailed calculations of ZGNR electronic structure. Wu sumarizes that longer ZGNRs possess increasingly polyradical character in the ground states, where the active orbitals are mainly localized at the zigzag edges, and also that with the increasing length of the ribbon, the fundamental gaps and vertical ionization potentials decrease while the vertical electron affinities increase [34]. The properties further depend on width of the ribbon. The width of a ZGNR may be described by the number of carbon pairs forming its zig-zag edge when repeated. We use this description because it turned out to be less confusing than the mentioned above. The minimal number of these pairs to form a base unit of a ZGNR is 2, (denoted as 2ZGNR). A number of theoretical studies was conducted on the topics of electronic transport properties in GNRs [35, 36], investigating impact of edges on it [37, 38], in order to get GNR-based heterostructures [39] and field-effect transistors [40, 41].

An interesting application of graphene and graphene layers was described in recent papers. Tombros et al. report the observation of spin transport, as well as Larmor spin precession over micrometer-scale distance in single graphene layers [42], while Leutenantsmeyer et al. observed a large spin-lifetime anisotropy in bilayer graphene [43]. Zhang et al. show that ZGNRs with two ferromagnetic strips along two opposite sides may be used as a spin filter [44]. In another works, the gate-tunable spin valve is proposed and role of universal conductance fluctuations and spin injection is discussed [45, 46]. The nanographenes of various topologies are investigated, e.g. the triangular shaped as nanomagnets for molecular spintronics [47, 48]. The magic-angle twisted trilayer graphene is shown to have tunable strongly coupled superconductivity by Park et al. [49]. Finally, physical properties of nanographenes are also investigated for applications in fuels and combustion [50, 51].

We investigated graphene nanoribbons in various configurations. In one of our first publications we analyzed edge-localized states for the purpose of spin filtering [A3]. We selected the proper structure, placed the carbon atoms in to original positions and passivated all the free bonds by hydrogen atoms. In order to reach the thermodynamic equilibrium of the system, the optimized atom positions are computed by molecular mechanics. We used embedded Brenner quick optimizer to optimize geometry of the chemical bonds so as the maximal component of the interatomic force was less than 10^{-9} eV/Å after optimization. For the calculation of electrical properties we used semi-empirical EH-SCF method for nanoscale devices, with spin polarization considered [17]. As shown on the **Figure 22**, the simulated

system is divided in two electrodes (source and drain) and the central region. This is the configuration explained in the **Chapter 3.2**. Due to the used method, we need to extend the electrodes into the structure. In order to consider the electrodes as a bulk region, we need to have enough space in the central region for both electrode extensions. Depending on the structure, this length for extension should be about 5 to 10 Å. It is 7.38 Å in case of this simulation. Atom *i'* in the electrode extension is identical to *i* in the electrode (shown on the **Figure 22** as the red dots). Further details about the EH-SCF method can be obtained in [17]. In order to simulate the situation where electrodes are made of GNRs, we need to leave the atoms involved in the electrodes without change. Thus the first three atoms from both sides of the structure are left without defects and they are only affected by mechanic of the whole system during the optimization, which mostly means small linear strain over the *z*-axis.

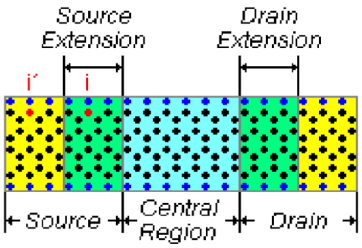

Figure 22. General situation scheme of the simulated system.

At first, we analyzed the 2-ZGNR structure shown in the **Figure 23a**. From the **Figure 23b** we can clearly see that, while spin up electron eigenstates are strictly placed on the edge of the ribbon, the spin DOWN electron eigenstates are on the contrary placed inside the ribbon. We obtained transmission spectrum (**Figure 23c**) with visible strong spin splitting. There are free energy levels only able to transport electrons with spin DOWN in the vicinity of the Fermi level. For the energies greater than zero, another mode seems to emerge, making possible greater transmission for spin UP (DOWN) electrons at positive (negative) energy levels. Transmission of spin DOWN electrons is always approximately 1 or greater for the surveyed small energy levels. The second analyzed structure is the 4-ZGNR shown on the **Figure 24a**. The **Figure 24b** shows similar character of the eigenstate localization for spin UP (or DOWN) electrons as visible on **Figure 23b**. Once again, we can see significant spin splitting of the free energy levels in the transmission spectrum (**Figure 24c**). This time, on the contrary to 2-ZGNR, spin DOWN electrons transmission seems to be almost fully restrained for some small negative energy levels and the transmission spectrum itself is more symmetrical than the one of the 2ZGNR.

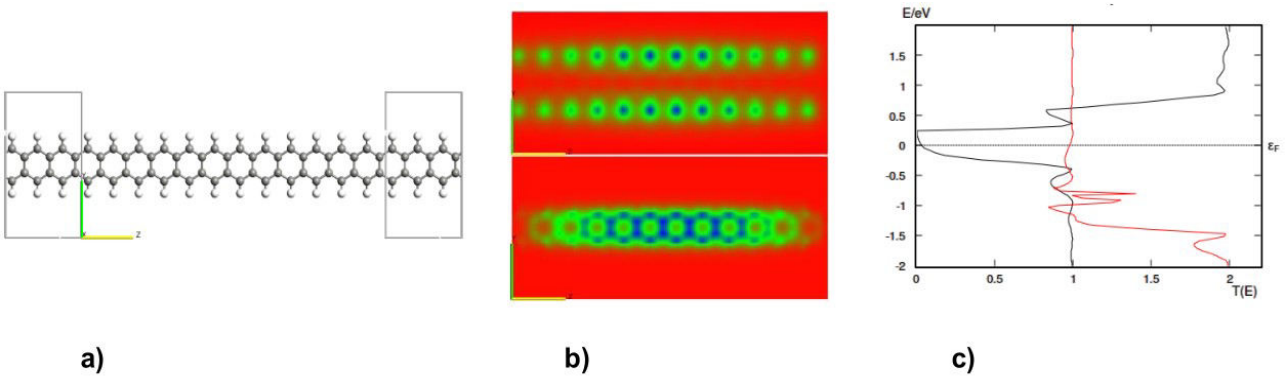

Figure 23. a) Simulated 2ZGNR system. **b)** Eigenstates for the quantum number 0, spin UP electrons at the top and spin DOWN at the bottom. The color range covers the eigenstate values from their minimum (blue) to maximum (red). **c)** Transmission spectrum for spin UP (black) and DOWN (red).

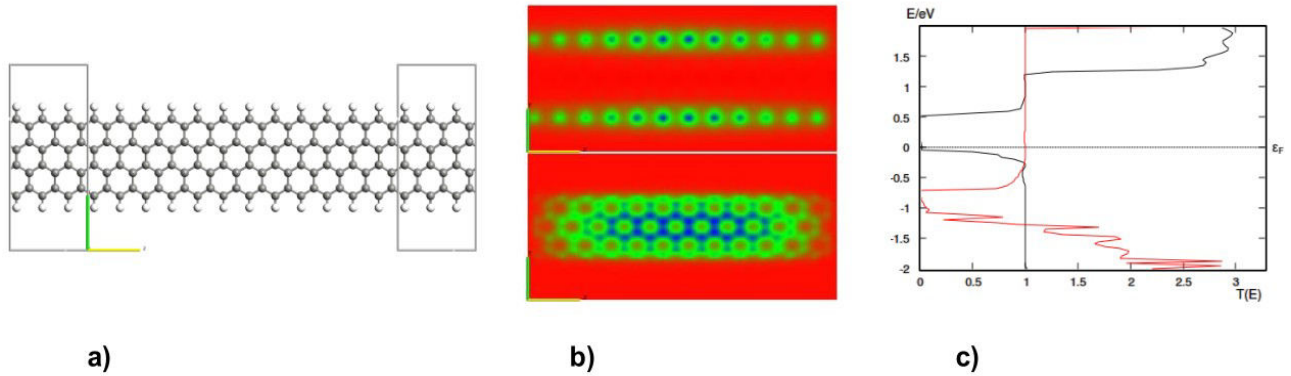

Figure 24. a) The simulated system. **b)** Eigenstates for the quantum number 0, spin UP electrons at the top and spin DOWN at the bottom. The color range covers the eigenstate values from their minimum (blue) to maximum (red). **c)** Transmission spectrum for spin UP (black) and DOWN (red).

The third analyzed structure is the 4ZGNR with an edge defect in the central region of the system (**Figure 25a**). The defect is symmetrical to the z-axis and it is causing the narrowing of the ribbon to the 2ZGNR, creating very short segment of the 2ZGNR connected to the 4ZGNR electrodes. The eigenstates on the **Figure 25b** shows clearly the effect of the necking in the central region. By comparison of **Figure 24b** and **25b**, we can conclude that the area of both spin electron eigenstates on **Figure 25b** is smaller and it is arranged close to the defect. The transmission spectrum on the **Figure 25c** shows the energy levels spin splitting and also the overall inhibition of transmission at the surveyed low energy levels.

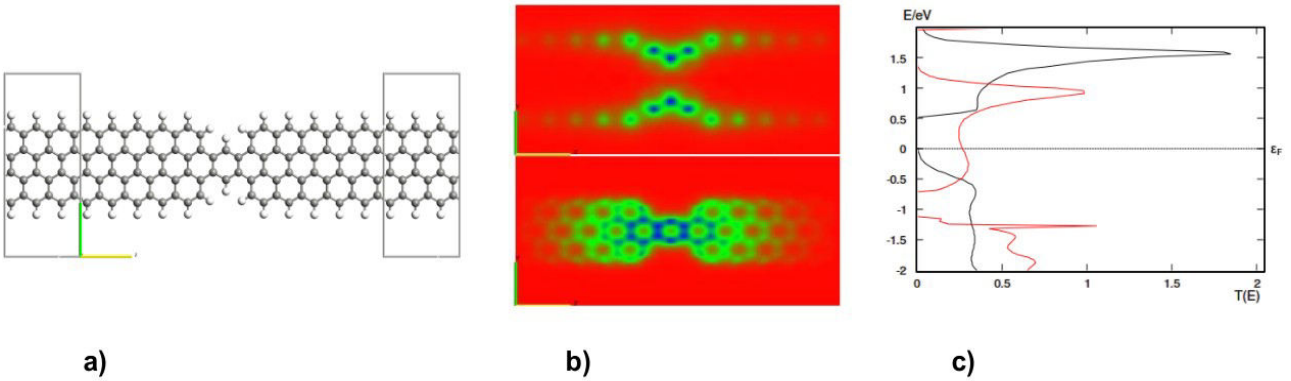

Figure 25. a) The simulated system. **b)** Eigenstates for the quantum number 0, spin UP electrons at the top and spin DOWN at the bottom. The color range covers the eigenstate values from their minimum (blue) to maximum (red). **c)** Transmission spectrum for spin UP (black) and DOWN (red).

The last analyzed structure is the 4ZGNR with the linear defect causing the separation of the ribbon in two segments and disconnecting carbon-carbon bonds completely (**Figure 26a**). The defect is placed shapely that the separation is anti-symmetrical to the z-axis and y-axis. All the aromatic rings on adjacent sides of the separation are preserved and distance between the two separated sides of the ribbon is slightly enhanced due to the repulsive forces of the bonded hydrogen. In the **Figure 26b** we can see the arrangement of the eigenstates. The UP spin electron eigenstates are located at the center while the DOWN spin electron eigenstates are located only on the one side of the separated ribbon. In the transmission spectrum (**Figure 26c**) we can see the result of this phenomenon. The DOWN spin free energy states

seems to be diminished almost completely but the UP spin energy states are available for energies allowing transport of the UP spin electron from one side of the separated ribbon to another. In the **Figure 27a** and **27b** we can see, that only the hydrogen atoms can facilitate the UP spin electron transport. These figures show how the electrons transmist through the ribbon at the energy ε = 1.9 eV. We can clearly see that current created by DOWN spin electrons (**Figure 27a**) on this energy level cannot overcome the defect because in this case it is transported only through the carbons. On the contrary, the current created by the UP spin electrons (**Figure 27b**) can overcome the barrier of the linear defect because of the closely located hydrogen atoms.

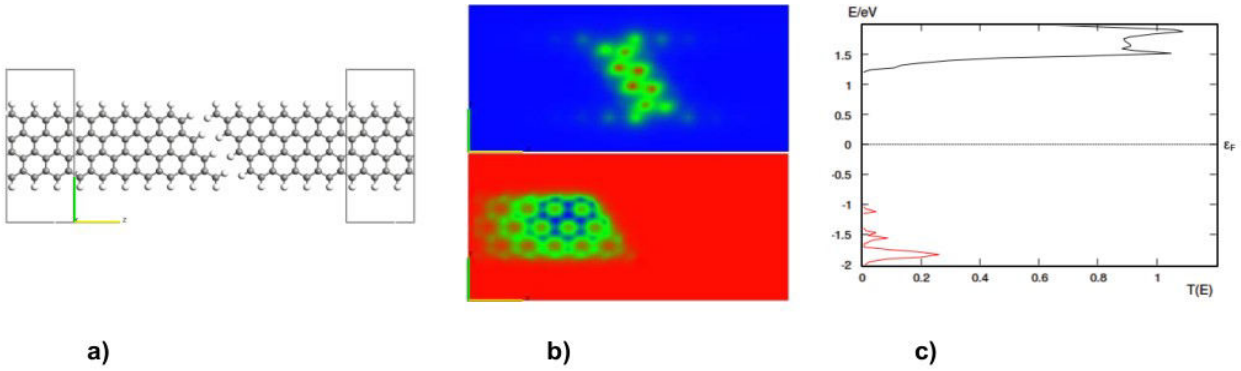

Figure 26. a) The simulated system. **b)** Eigenstates for the quantum number 0, spin UP electrons at the top and spin DOWN at the bottom. The color range covers the eigenstate values from their minimum (blue) to maximum (red). **c)** Transmission spectrum for spin UP (black) and DOWN (red).

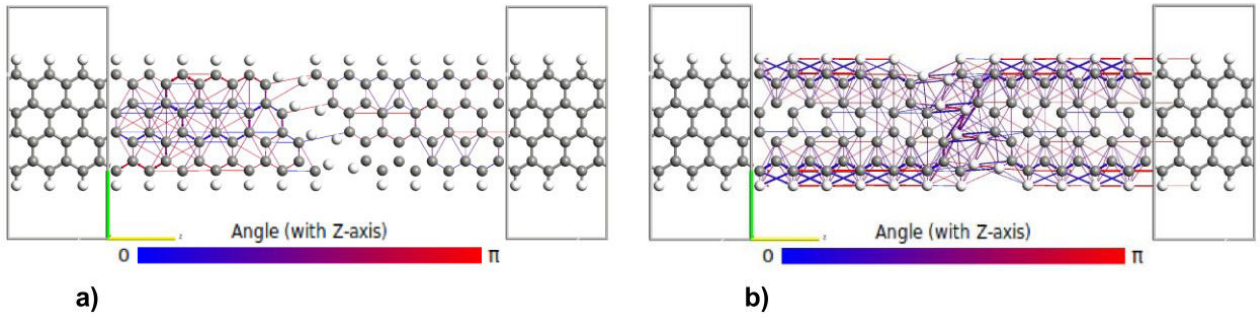

Figure 27. Electron transmission pathways at the energy 1.9 eV. The line thickness is proportional to the strength of the current. **a)** For spin DOWN electrons. **b)** For spin UP electrons.

Let us show some unpublished results of the other structures, gathered during our study of nanoribbons, in the following figures. Motivated by the quantum-mechanical tunneling effect in nanoribbons and probing of QCA/crossbar/nanocell architecture approaches mentioned before, we investigated a set of GNR structures in parallel configuration. The nanoribbons were fused in different points to test properties of their wavefunctions and to evaluate the efficiency of used simulation methods. The same semi-empirical model as in the previous example was used to conduct this study.

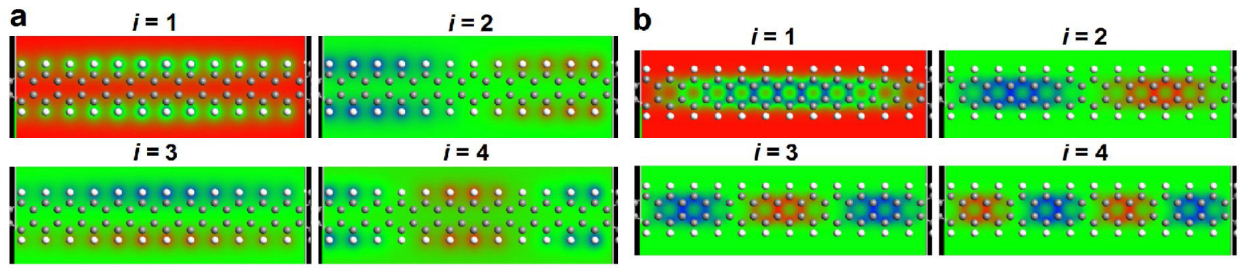

Figure 28. First four eigenstates for **a)** spin UP and **b)** spin DOWN. The color range covers the eigenstate values from their minimum (blue) to maximum (red).

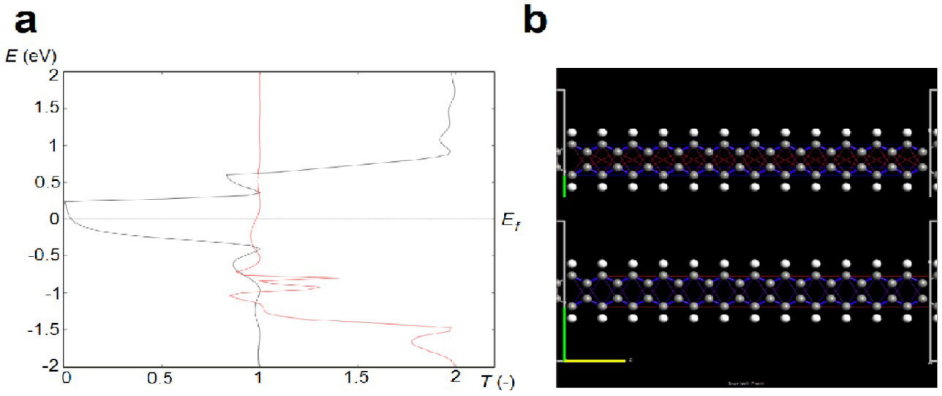

Figure 29. a) Transmission spectrum for spin UP (black) and DOWN (red). **b)** Transmission pathways for spin UP (top) and DOWN (bottom).

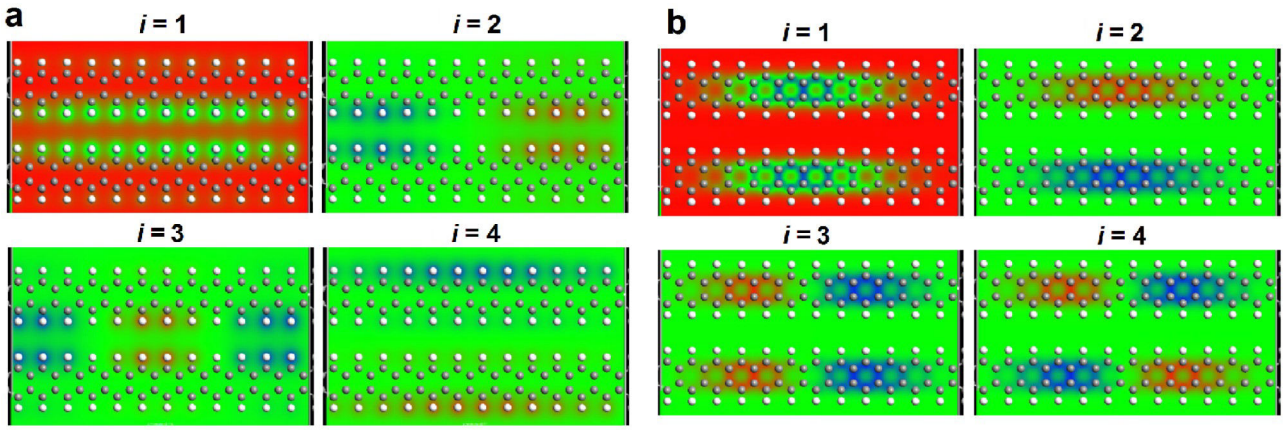

Figure 30. First four eigenstates for **a)** spin UP and **b)** spin DOWN. The color range covers the eigenstate values from their minimum (blue) to maximum (red).

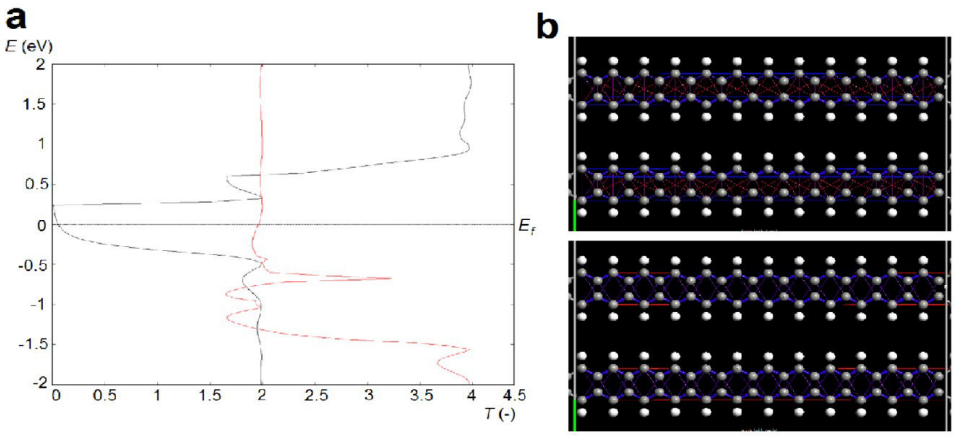

Figure 31. a) Transmission spectrum for spin UP (black) and DOWN (red). **b)** Transmission pathways for spin UP (top) and DOWN (bottom).

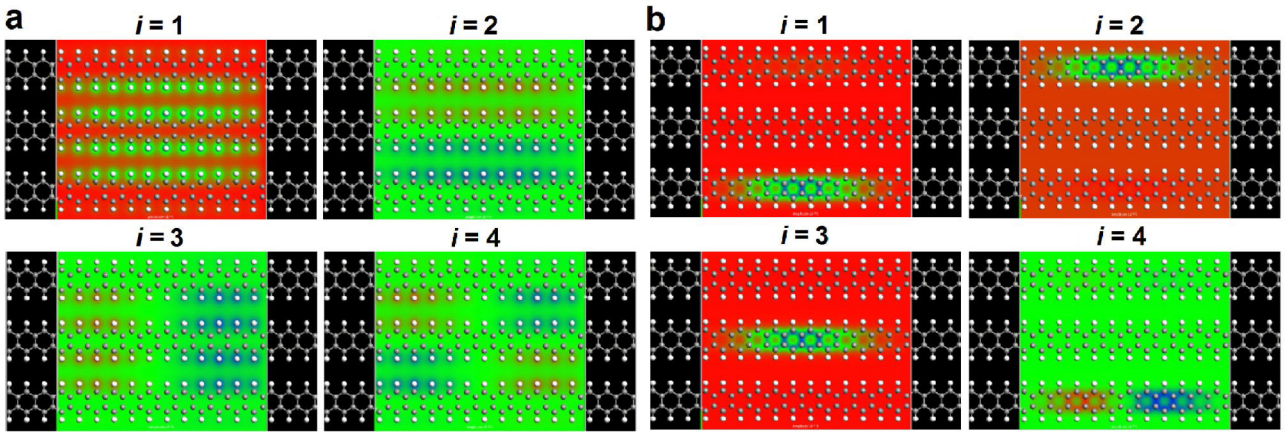

Figure 32. First four eigenstates for **a)** spin UP and **b)** spin DOWN. The color range covers the eigenstate values from their minimum (blue) to maximum (red).

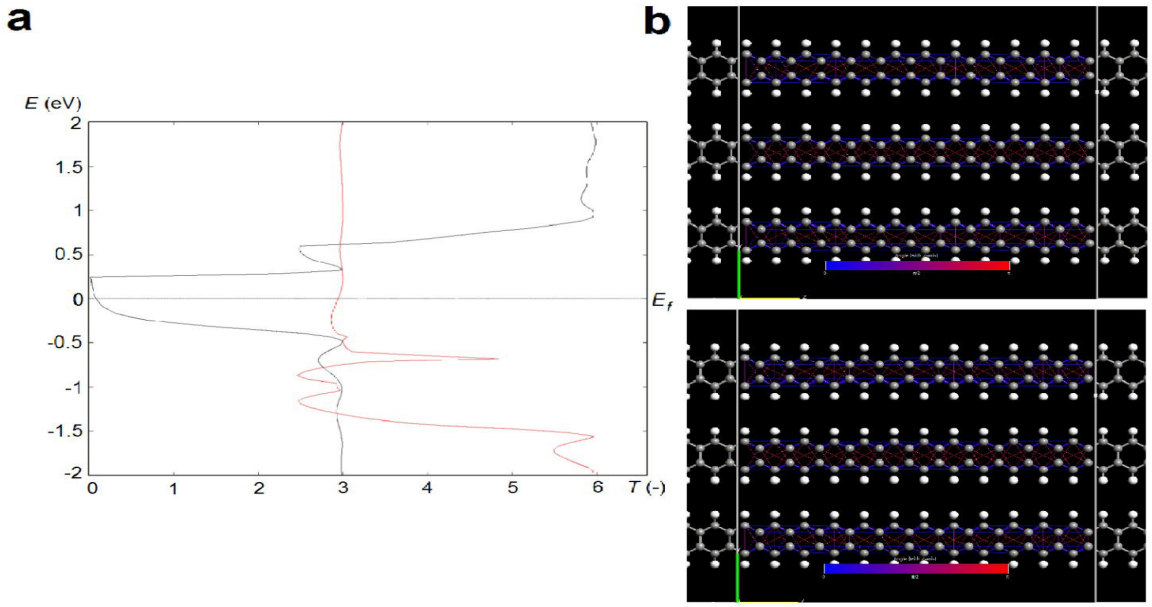

Figure 33. a) Transmission spectrum for spin UP (black) and DOWN (red). **b)** Transmission pathways for spin UP (top) and DOWN (bottom).

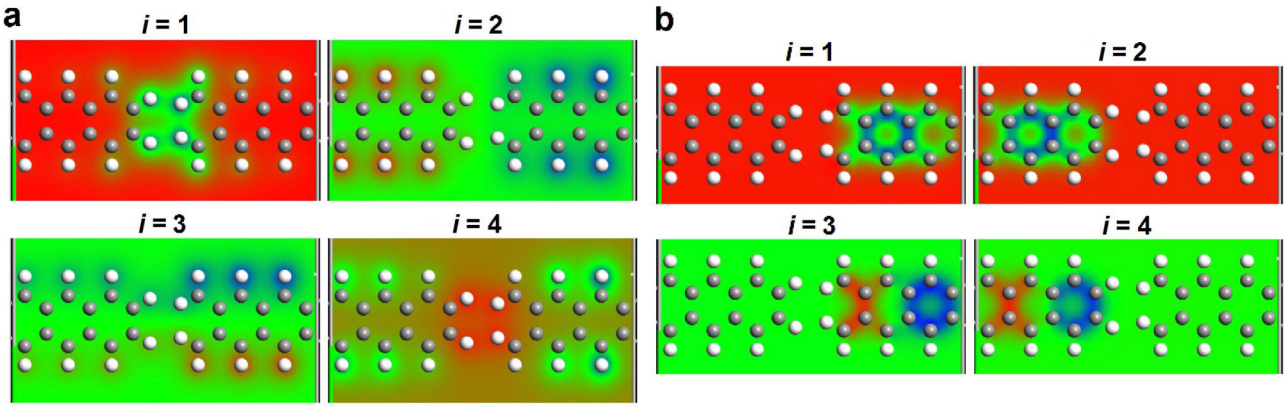

Figure 34. First four eigenstates for **a)** spin UP and **b)** spin DOWN. The color range covers the eigenstate values from their minimum (blue) to maximum (red).

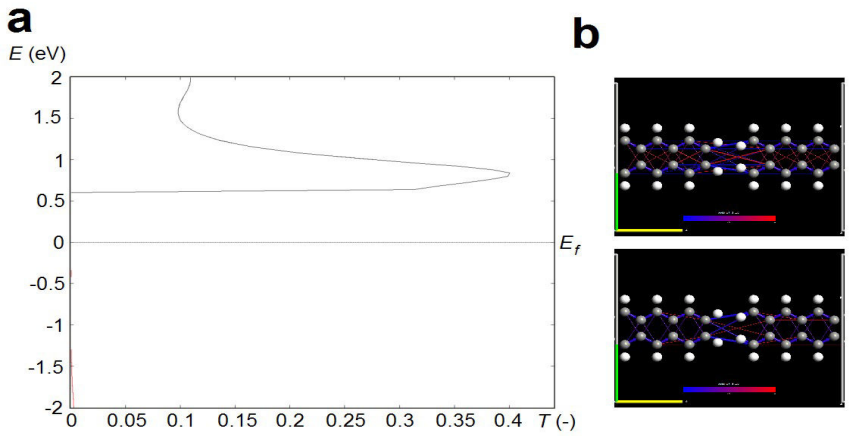

Figure 35. a) Transmission spectrum for spin UP (black) and DOWN (red). **b)** Transmission pathways for spin UP (top) and DOWN (bottom).

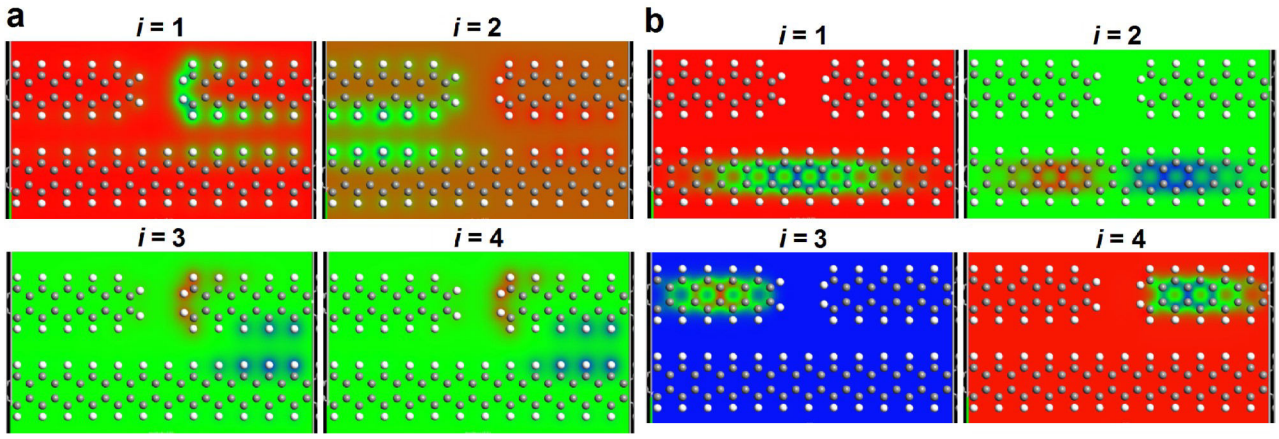

Figure 36. First four eigenstates for **a)** spin UP and **b)** spin DOWN. The color range covers the eigenstate values from their minimum (blue) to maximum (red).

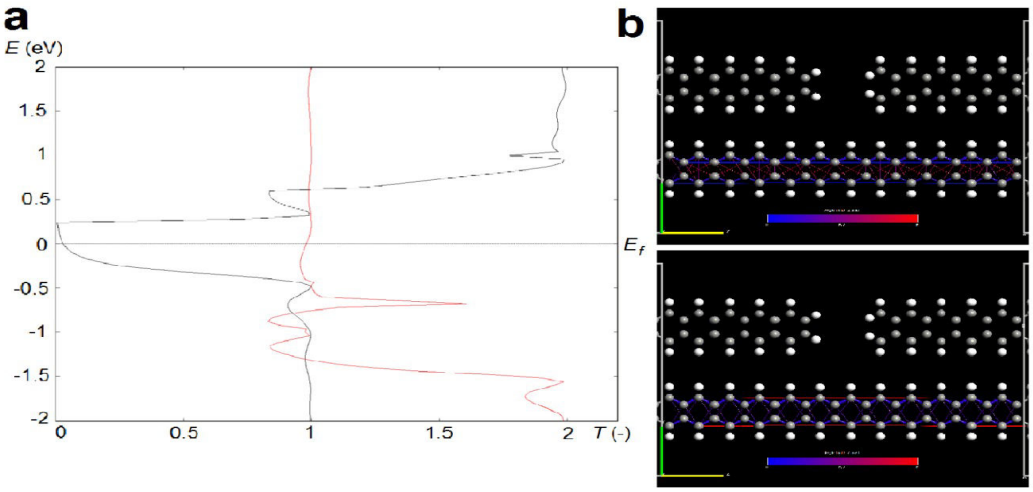

Figure 37. a) Transmission spectrum for spin UP (black) and DOWN (red). **b)** Transmission pathways for spin UP (top) and DOWN (bottom).

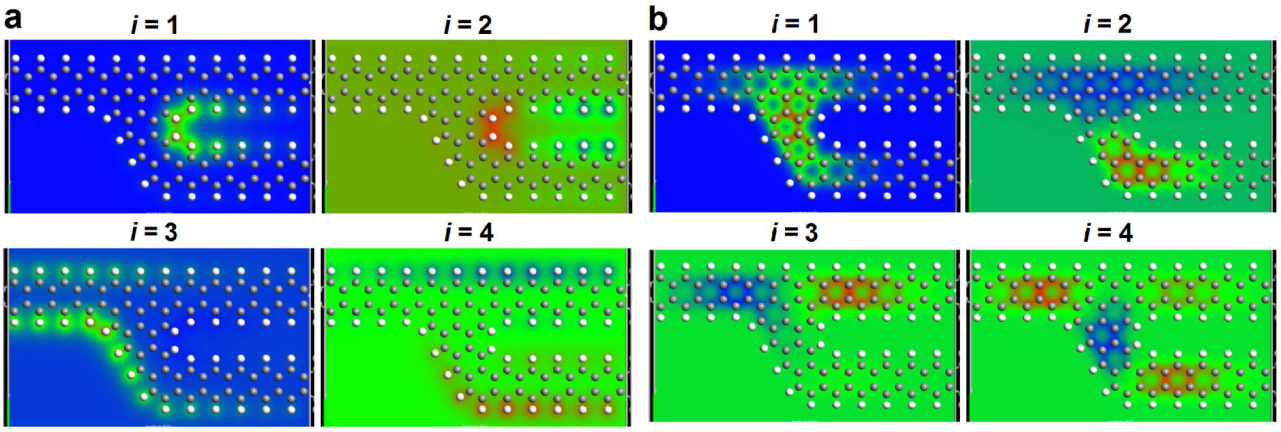

Figure 38. First four eigenstates for **a)** spin UP and **b)** spin DOWN. The color range covers the eigenstate values from their minimum (blue) to maximum (red).

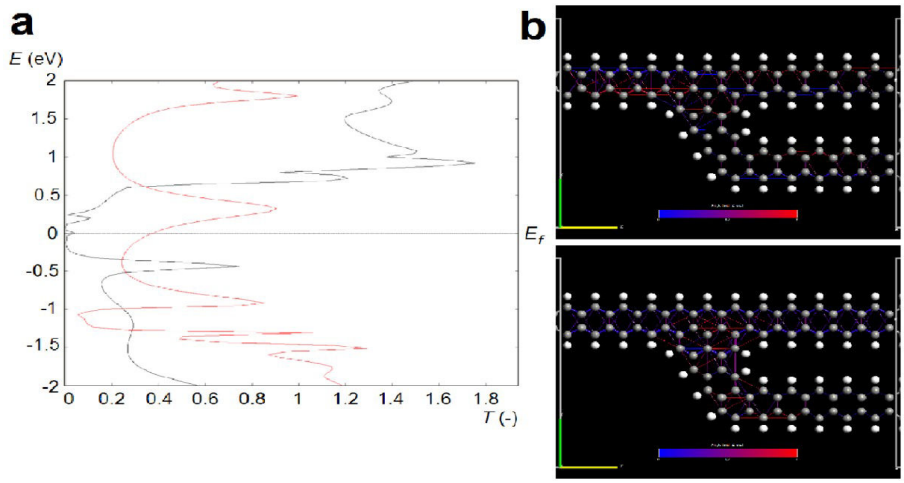

Figure 39. a) Transmission spectrum for spin UP (black) and DOWN (red). **b)** Transmission pathways for spin UP (top) and DOWN (bottom).

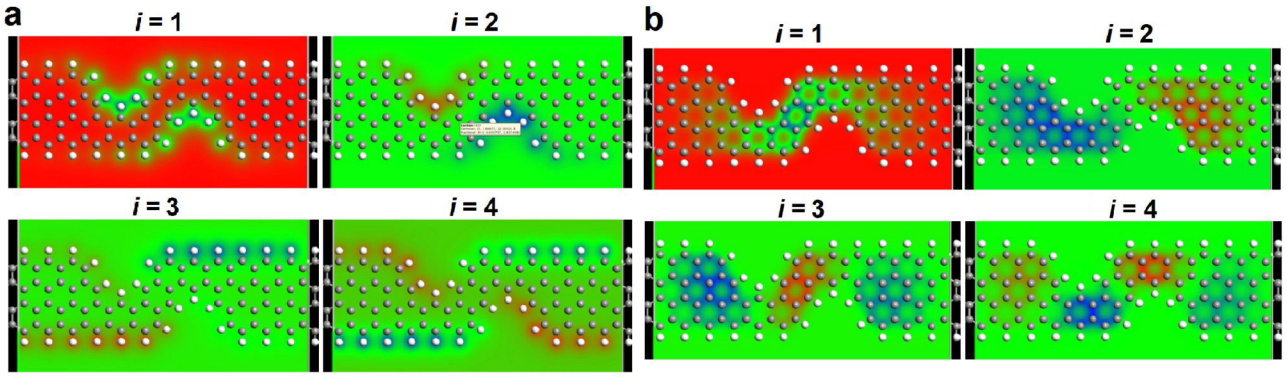

Figure 40. First four eigenstates for **a)** spin UP and **b)** spin DOWN. The color range covers the eigenstate values from their minimum (blue) to maximum (red).

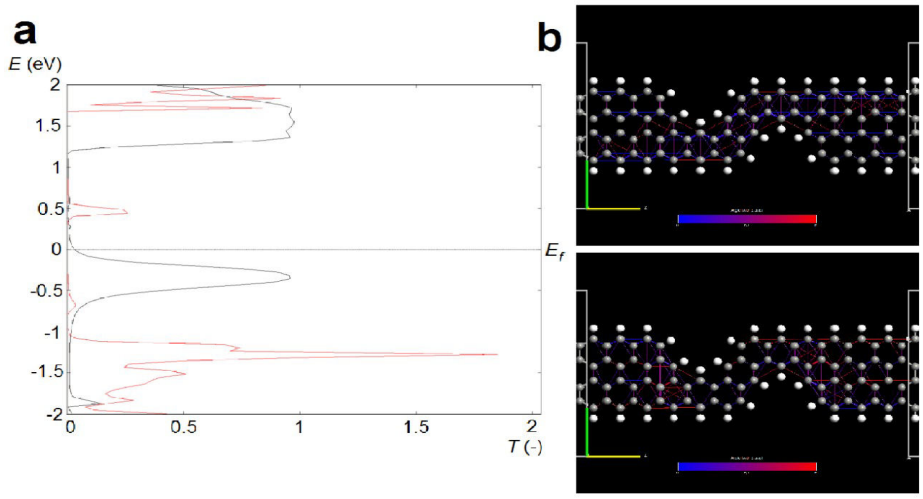

Figure 41. a) Transmission spectrum for spin UP (black) and DOWN (red). **b)** Transmission pathways for spin UP (top) and DOWN (bottom).

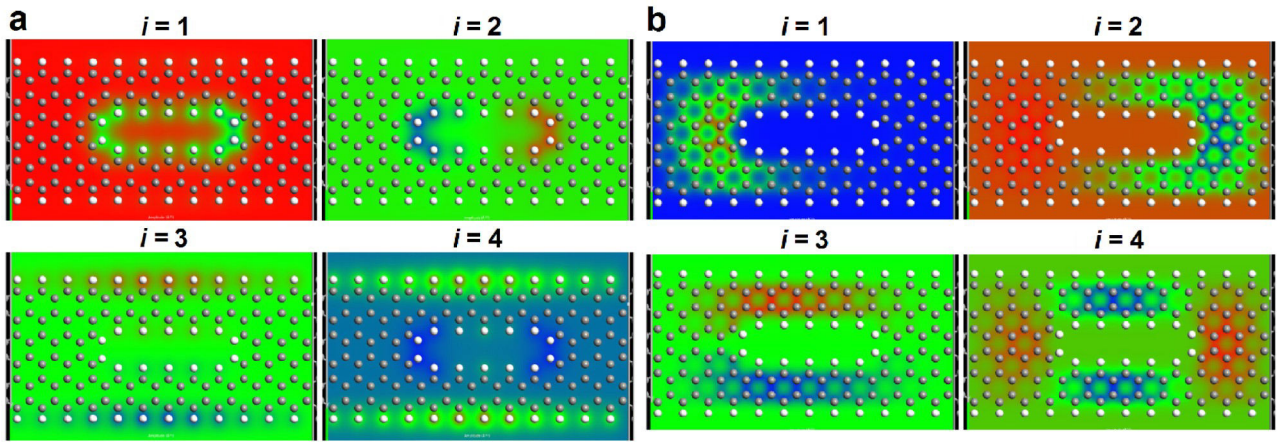

Figure 42. First four eigenstates for **a)** spin UP and **b)** spin DOWN. The color range covers the eigenstate values from their minimum (blue) to maximum (red).

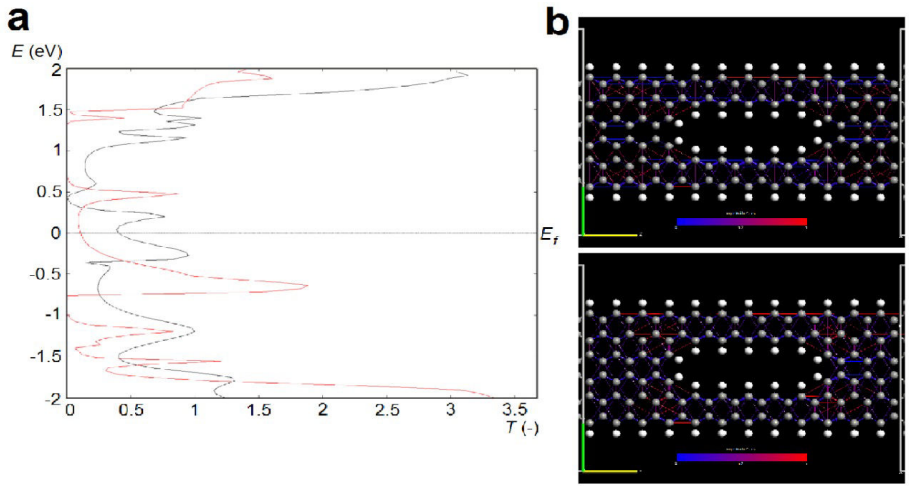

Figure 43. a) Transmission spectrum for spin UP (black) and DOWN (red). **b)** Transmission pathways for spin UP (top) and DOWN (bottom).

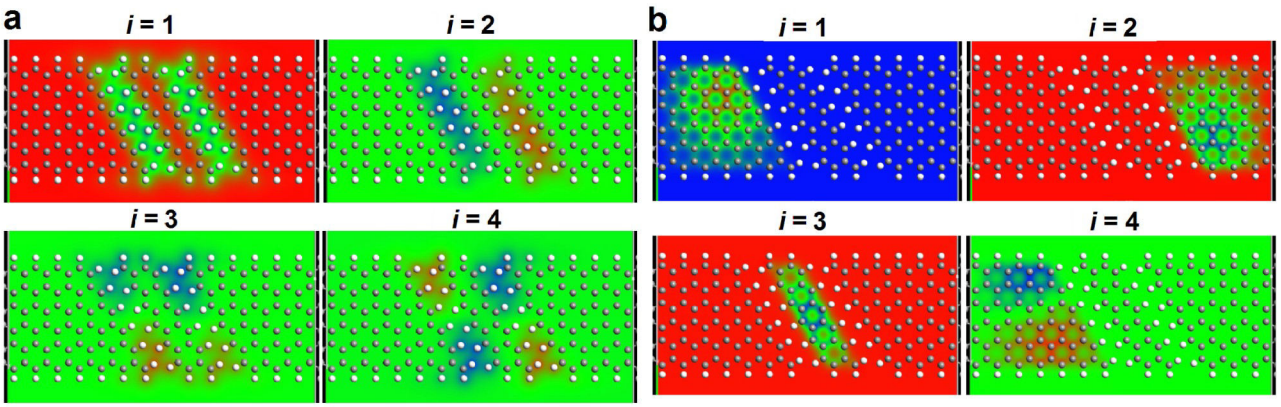

Figure 44. First four eigenstates for **a)** spin UP and **b)** spin DOWN. The color range covers the eigenstate values from their minimum (blue) to maximum (red).

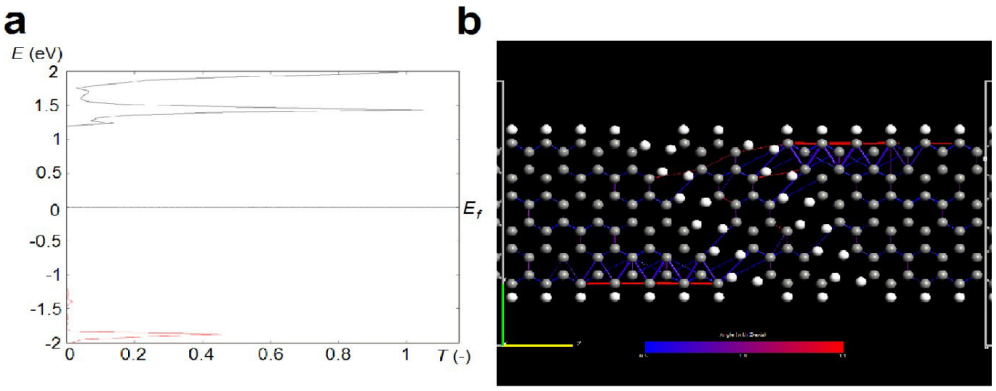

Figure 45. a) Transmission spectrum for spin UP (black) and DOWN (red). **b)** Transmission pathways for spin UP (top) and DOWN (bottom).

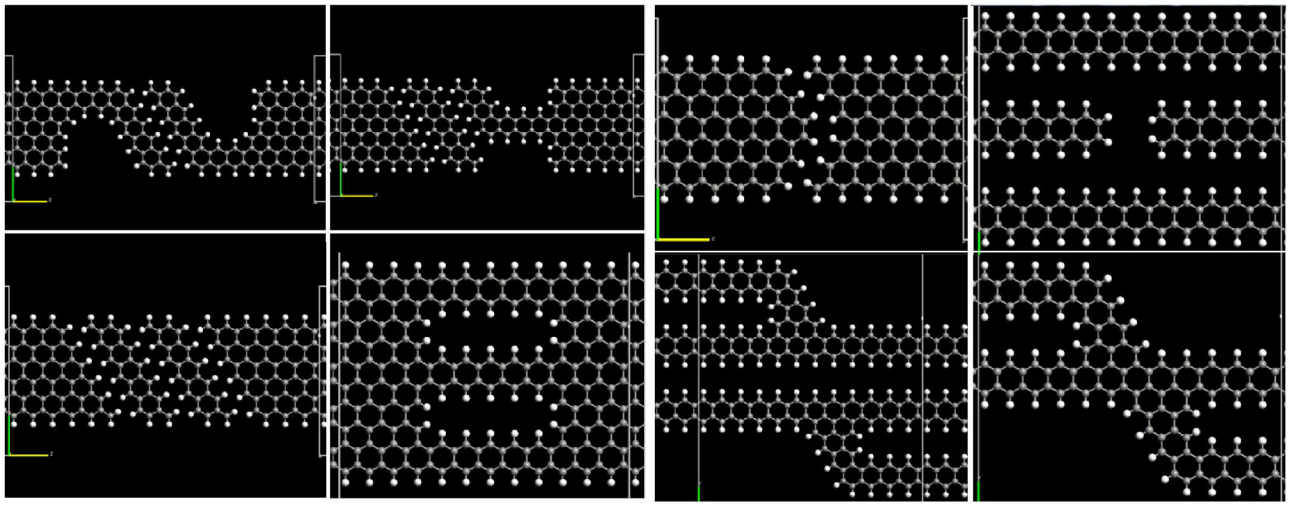

Figure 46. Some other hypothetical GNR topologies.

Our results show that passivated ZGNR structures have strong spin filtering ability and that for the generation of spin-polarized currents, the formation of spin-ordered edge-localized states along the zigzag edges is the key mechanism. Since GNRs have long spin-correlation lengths and good ballistic transport characteristics they can be considered a

promising active material for spintronic devices, without any need of ferromagnetic electrodes or other magnetic entities. The spin filtering structure could be prepared by the nanolithography of GNR. V-shaped notches could be realized by means of local anodic oxidation, e.g. using the scanning probe microscopy. All mentioned GNR structures may be as well prepared chemically from precursors.

5.1.1 Molecular Doping on the Graphene Sheets

The impact of molecular doping on the graphene is also explored in [26]. In comparison to three-dimensional bulk semiconductors such as silicon crystal, the two-dimensional morphology and single-atom thickness offer the graphene sheet more activity in response to either interior defects or exteriorly physical or chemical adsorptions. In graphene, each carbon atom is exposed to the environment with a dangling π bond, and thus is amiable to molecular functionalization on the basal plane. The functionalization process could be reversed by breaking the bonding between adsorptions and graphene sheet. For example, in the chemical reduction process for producing graphene sheets, graphene monolayers are firstly exfoliated from graphite by oxidation, where the epoxy and hydroxyl binding on the basal plane of graphene break the interlayer binding. The oxidation groups are subsequently reduced to recover graphene sheets. There are also efforts in engineering the physical chemistry of graphene by functionalization, especially in the extent of molecular doping, covalently or non-covalently. In addition to the approaches in bulk materials such as substitutions, vacancies and intersticials, the notion of doping has been renovated in a controllable and even reversible manner thanks to the coexistence of chemical inertness of sp^2 carbon network and relative activity of the p_z electrons involved. Non-covalent functionalization, or physisorption refers to the process in which the electronic structure of graphene is barely perturbed. The weak binding nature can be established through forces such as van der Waals or electrostatic dipole-dipole interactions. These functionalizations, especially those are weak in mechanical binding but strong in electronic coupling, hold great promises in various applications such as chemical sensors, molecular switches and transistors. Gaseous non-covalent dopants, such as the water molecule, N_2, NO_2 and NH_3, can be adsorbed physically on the basal plane of graphene. These adsorptions, although interacting weakly with graphene, have remarkable impacts on the intrinsic electronic properties of graphene. The adsorbed molecules change the local carrier concentration in graphene by adding electron, and lead to step-like changes in resistance. The micro-sized graphene thus can detect individual events when a gas molecule attaches to or detaches from its surface. Chemical sensors and non-volatile memories can be directly designed following this concept. The non-covalent binding of 2,3-dichloro-5,6-dicyano-1,4-benzoquinone and tetrathiafulvalene on graphene sheet induce the hybridization between the molecular levels and graphene valence bands, and transform the zero-gap semiconducting graphene into a metallic graphene. While the response of sensor based on this principle is low, it can be improved by introducing metal atoms to intercalate between the molecules and grapene sheet. Also some chemisorptions (forming covalent bonds with carbon atoms on the basal plane of graphene) can tune its properties in controllable manner. Hydrogenation and oxidation are two of the most noticeable approaches in the covalent context. Electrochemical modification of graphene can be induced by chemical reactions of graphene with proton and hydroxyl that are catalytically generated from water molecules in the gate dielectrics, making the graphene nonconductive. This process can be reversed by short current pulses that cause rapid local annealing. There is also the semimetal-insulator transition in graphene after hydrogenation, which is then recoverable through structural annealing. This reversible engineering on graphene has further potential appliacations in designing functional nanoscale materials and devices, such as patterned nanoelectronics.

5.1.2 Interior Doping through Defects

The properties of a crystal are among other, dependent on the concentration of defects. The defects are either impurities or dislocations. While the impurities may act as doping, the dislocations may lead to the degradation of mechanical properties and into severe changes in the bandstructure as well. Because of the reduced dimensionality of graphene (2D), there is also a reduced number of possible defect types in a layer [52] or in a ribbon. In a nanoribbon, the maximum number of defects will be limited by width. In one of our published studies [A7], we investigated the impact of Stone-Wales defects on bandstructure, electron density and interatomic forces in 4ZGNR.

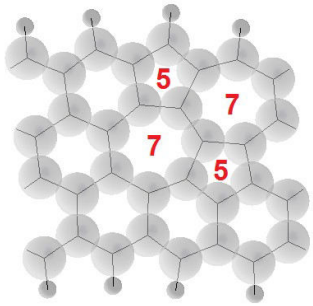

Figure 47. Depiction of SW(5577) defect in 4ZGNR. The ball size represents covalent radius of atoms. Large circles are carbons, small are hydrogens.

The simplest defect in graphene, that may be caused by e.g. radiation damage, thermal load, mechanical stress, or it is already inherent from the preparation method (chemical vapour deposition [52], exfoliation [18], bottom-up assembly [24]), is the rotation of C-C bond by the angle of 90°, the so called Stone-Wales defect (SWd). There are no C atoms added or missing and this defect is made by the lattice reconstruction alone. Because of the sp^2-hybridizing property of graphene that allows the attachment of varying number of nearest neighbours to a C atom, they may form even different polygon structures than hexagons (pentagons, heptagons, octagons). For example, four hexagons can be transformed in 2 heptagons and 2 pentagons (SW (5577)), see **Figure 47**. The described SW (5577) defect, when placed on a thin ZGNR, causes severe changes in the bandstructure. At first we considered a clear 4 bases long 4ZGNR which lacks any defects, then we passivated two edges by hydrogen and left the other two edges for periodic extension of C-C covalent bonds. We optimized the geometry by Tersoff_CH_2010 optimizing algorithm to equilibrium state (with maximal component of interatomic force lower than 0.005 eV/Å), and calculated bandstructure and electron density by DFT calculator. Local Density Approximation with Perdew-Zunger (PZ) basis set. The *k*-point sampling {1, 1, 2} and the mesh cutoff 75.0 Hartree was used. The Poisson solver was set to the FFT2D with periodic boundary conditions in the directions *x* and *y* and the Dirichlet boundary conditions in the direction *z*. Self Consistent Field iterations were included to the depth of 20 steps.

In the next step, we changed the direction of the C-C bond in the middle of the GNR by the angle of 90° and, by the above described means, we calculated the electron density and the bandstructure, this time without the optimization to the relaxed state and thus with resulting greater interatomic forces. Then we used Tersoff_CH_2010 optimizer again with restriction to 10 steps and maximum force limit 0.005 eV/Å. In every 10 steps we recorded the atomic positions and forces and made the electron density and bandstructure results for the purpose of animated sequence. Because the structure converged to equilibrium in 70 optimization steps, we made 7 additional calculations. The resulting atomic positions are depicted in the **Figure 49**. The complete results were composed into .gif sequence available in the published article attachment.

As we can see from the bandstructure (**Figure 48**) and the electron density (**Figure 49a** and **49b**), the undistorted 4ZGNR has the expected linear *E-k* dispersion relation (see **Figure 48a**). When distorted by the SWd, the 4ZGNR exhibits topological changes in the electron density (from the homogenious distribution among C atoms to the lateral distribution with peaks in respect to the y-axis) and the bandstructure becomes parabolic (see **Figure 48b**). At room-temperature conditions (300 K), the structure quickly relaxes to thermodynamic equilibrium (which is simulated by the optimization to minimum interatomic forces) and the bandstructure changes accordingly. The electron density remains unequally distributed in respect to *y*-axis. Because the number of components in the crystal remains the same and the total number of atoms does as well, the resulting forces in the ribbon are small and the optimization of structure converged quickly (in 70 steps) to the maximum interatomic force components not greater than 0.005 eV/Å. The direction of interatomic forces in the GNR changed by introducing the SWd and remained unequaly distributed even after optimization. This implies that the resulting forces in the distorted ribbon are greater than in the undistorted one. The sequence of pictures in the article attachment describes more closely the trend of bandstructure and electron density variations during the optimization.

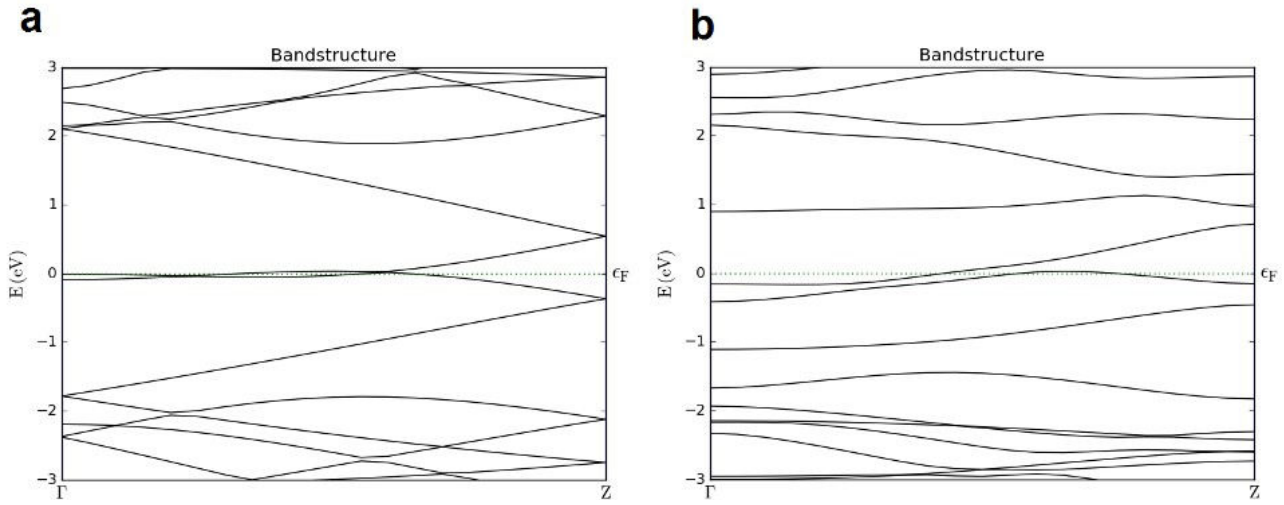

Figure 48. The bandstructure calculated for relaxed 4ZGNR **a**) clear, **b**) with SW(5577). The energy is in absolute values. ϵ_F is the Fermi level, Γ and Z are symmetry points in hexagonal lattice. The *x*-axis represents the *k*-vector values.

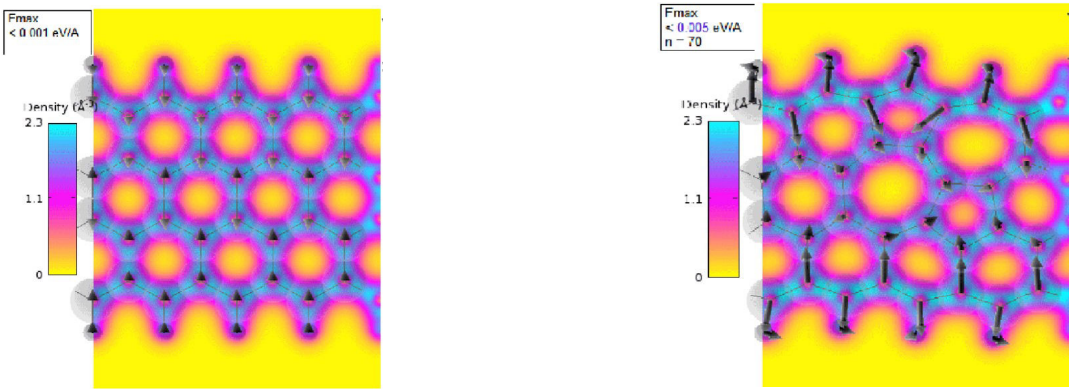

Figure 49. a) Electron density and resulting interatomic forces of clear 4ZGNR. F_{max} is the maximum interatomic force component. **b)** Electron density and resulting interatomic forces of 4ZGNR with SW(5577). *n* is the number of optimization iterations. Optimization was done when maximum interatomic force condition 0.005 eV/Å was reached.

From our calculations we concluded that the bandstructure and the electron density of 4ZGNRs are strongly affected by the Stone-Wales defect introduced into it, however the thermodynamic stability of the structure does not severely changes. The bandstructure of resulting structure exhibits a narrow bandgap for certain *k*-vectors. The homogenious distribution of electron gas changes to the lateral distribution, resulting in two parallel topological quantum wires. The lateral distribution of the electron density may be usefull for improvement in the spin filtering ability of GNRs, e.g. in the case if there are V-shaped lateral constriction (notches) introduced to the ribbon. The questions for the further study are also: the impact on the spin-polarization and the impact of the greater number of defects introduced to a GNR on I-V curve. Because the used approach roughly simulates the SWd generation process, it would be also interesting to study how much the course of optimization follows the real process, e.g. how optimization steps should be compared to the typical time-scale of the generated SW defect relaxation.

5.1.3 Graphene Epitaxially Grown on Step-shaped SiC Surface

In one of our published studies we deal with the recently developed technique of epitaxial graphene growth on silicon carbide surface [A8]. The main problem of graphene nanotubes and nanoribbons are difficulties in the control of the position, radius, chirality and length. In many applications it is more desirable to prepare the graphene directly on an insulating substrate and then pattern the graphene in areas where it is required via process flow similar to one used for silicon-on-insulator devices. A graphene grown on insulator allows integration of large scale circuits, not just individual devices. A process of generating graphene on insulator, or more specifically multilayer epitaxial graphene (MEG) on SiC (MEG/SiC), has been developed by the high temperature sublimation of silicon from SiC [53]. Growing thick graphite samples on SiC has been a well-known process for many years until the thickness was decreased to a few layers, and a full characterization of the high quality graphene sample carried out. The growth of epitaxial graphene on SiC is based on thermal decomposition of the SiC substrate. E-beam heating as well as resistive heating is used, but no difference seems to arise from the different heating methods. In order to avoid contamination the heating is usually performed in ultra-high vacuum (UHV) environment or sometimes with Ar gas. From the molar densities one can calculate that approximately three bilayers of SiC are necessary to set free enough carbon atoms for the formation of one graphene layer. The growth of the graphene can take place on the (001) (silicon-terminated) or (0001) (carbon terminated) faces of 4H-SiC and 6H-SiC wafers. The main difference lies in the sample thickness that one can achieve. In the case of the silicon face, the growth is slow and terminates after relatively short time at high temperatures leading to the rise of very thin samples, down to a monolayer. On the contrary, in the case of the carbon face, the growth does not self-terminate leading to the rise of the relatively thick samples (approximately 5 up to 100 layers) with larger orientation and turbostatic disorder [54].

Because of the relation between graphene and SiC lattice constants, there is a large number of possible orientations of graphene. One structure of particular relevance is the ($6\sqrt{3}$ x $6\sqrt{3}$)R30 structure. Note the high symmetry points of the graphene lattice relative to the SiC. There are points where either the carbon atom in the graphene layer sits directly above an atom in the SiC layer below, or a SiC atom lies directly below the center of a graphene hexagon. We can define a quasi-unit-cell that is defined by these high symmetry points. For the appropriate ($6\sqrt{3}$ x $6\sqrt{3}$)R30 structure the quasi-cell would be a (6 x 6) SiC unit cell [55]. The primary cell of this structure is long and it takes long time to proceed one calculation. So this cell is usually artificially decreased. As a result we get simple model of graphene sitting above a relaxed bulk bilayer. Models like these cannot accurately describe the interface layer, but can predict a number

of important results. Firstly, the relaxed distance between the last substrate atom and the first graphene layer is larger on the Si-face (about 2.0 Å) than on the C-face. Secondly, the evolution of the band structure with the number of graphene layers can be predicted. The first graphene layer, which is more tightly bounded to the substrate, has a significant distortion of the π-bonds that gives the growth to a gap in the band structure. This first graphene layer shows no evidence of a graphitic electronic nature. The second graphene layer has the linear dispersion at the *k*-point characteristic of an isolated graphene sheet. Thus, in these calculations, the first graphene layer on both substrates acts as a 'buffer' layer electrically isolating the second graphene layer from the substrate. The third graphene layer shows splitting of the hole and electron states at the k-point stacked graphene bilayer. It is important to realize that, as the graphene forms, the surface of the sample will recede when Si atoms are leaving. The carbon content in a single graphene monolayer is very close to three SiC bilayers (36.5 atoms per square nm). The latter constitutes 0.75 nm of the height in its SiC form, whereas the graphene monolayers are spaced by about 0.34 nm from each other and have similar spacing to the SiC (for the C-face) or the $6\sqrt{3}$ layer (for the Si-face). Thus, for each additional monolayer of graphene, the top surface must recede by about 0.4 nm. So, if graphene thickness is different across the sample, thickness of substrate is different as well. Also, graphene thickness is measured in number of graphene layers, which is discrete number. Assume sample with 1, 2, 3 and 4 monolayers graphene thickness on it. The morphology of the surface of such sample changes: now is covered by step edges. With the flat regions of the surface, steps form irregularly-shaped μm-sized regions, which are separated from neighbouring terraces by step bunches. If we compare the Si-face and C-face graphene morphologies for a fixed film thickness, we can find that they are very different. But if we compare them at fixed temperatures, the differences become understandable, at approx. 1320°C. The films thickness on the C-face is much greater than for the Si-face (16 vs. 2), but both films display the characteristic ridges associated with strain relaxation. Both surfaces display comparable amount of step bunching. The reason for choosing the thicker film on the C-face is that the (0001) surface and the (0001)/graphene interface have higher energies (are more unstable), respectively, than the (0001) surface and (0001)/graphene interface. Additionally, more defects in the C-face films such as the discontinuities and rotational domain boundaries can lead to easier Si diffusion through the graphene, which will also provoke thicker growth.

When graphene is based on the Si-face in 1 atm of argon, the tendency to grow in a layer-by-layer manner becomes even more pronounced. In that case, it is quite easy to produce a single monolayer extending over order of 10 or 100 of μm on the surface. As indicated above, the electronic properties of EG on SiC are layer dependent. An important fact is that the buffer layer has an energy gap at E_f, so transport experiments and valence spectroscopies measure the effect of the graphene layers. The experimental E(k) is linear, with a characteristic band velocity consistent with the band structure of an ideal monolayer. Close examination of the spectrum reveals a small shift of the energy bands above the Dirac (charge neutrality) point ED relative to the bands below ED. It was ascribed to many-body interactions or to the creation of a small band gap. The parabolic energy bands of layer 2 graphene are apparent, as is the lower energy split-off band. These observations are predicted for bilayer graphene. The small energy gap centered around -350 meV is the result of the interface electric field; it can be driven to zero by balancing the interface field with an electric field contributed by surface adsorbates. Carrier density is also a layer dependent quantity in EG. The charge neutrality point shifts with respect to the Fermi level (zero tunnel bias) for successive EG layers on SiC(0001) [56]. The morphology of epitaxial graphene on SiC is highly influenced by the underlying SiC structure. Steps on substrate can lead to the problem with proper graphene growing without junk effects, but for few-nm steps the graphene lattice is continuous. It

is well known fact, that SiC{0001} surfaces exhibit step bunching. Steps which are perpendicular to the directions <1100> are strongly favored on (0001). It is perhaps expected that epitaxial graphene growth should proceed first on nanofacets. High temperature annealing causes vertically etched steps (on the order of 10 nm deep) to produce (1-10) facets with a normal that has an angle of 23° with respect to the {0001} direction. Cross sectional, high resolution transmission electron microscopy of the graphene on steps on SiC has shown that the graphene terminates perpendicular to the silicon carbide surface both on the bottom of the step or on the steps themselves. Moreover, these atomic resolution studies further show that the graphene edges are along the zigzag direction, indication that the graphene sidewall ribbons are zigzag ribbons. This is very important when the edge structure determines the electronic properties of the ribbons. In particular, zigzag ribbons are always metallic. In [57] are introduced experimental results of produced graphene structures by using standard lithography methods of producing an etch mask on the surface. Then, the masked surface was subjected to a plasma to etch the desired pattern to a predetermined depth into the surface. Then at temperature of about 1550°C, in about 10 minutes, the monolayer of graphene has been grown over the step. It presents an important step towards the realization of high mobility quasi 1D graphene structures that do not suffer from the strong localization effects observed in conventionally patterned graphene structures. In [58] the possibility of graphene production is also shown and resistivity of graphene was measured. According to experimental data, graphene with length about 1.6 μm and width about 39 nm has resistivity 26.1 kΩ. Hydrogen can saturate the silicon dangling bonds without a real decoupling of the interface. In these conditions the charge transfer to the graphene layer is reduced and, as a consequence, the carrier concentration decreases and the carrier mobility increases by about a factor of 2 to 5. The treatment is robust against nanofabrication and thermal cycling, from room temperature down to cryogenic temperature [57].

In this work we consider two different structures: graphene on step shape SiC substrate and graphene on planar substrate with additional interface graphene layer. All primitive cells were taken from QuantumATK database. We used moissanite (SiC) as a substrate because of its hexagonal crystal system. Because of stochastic behavior of the graphene on SiC, the covalent bonds between layers have no period and after optimization it becomes even worse. The problem is that at the end we will have very long structure with thousands of atoms. To avoid such problem we need to create the device directly from initial bulk and then do all optimization and passivate structure by hydrogen. The distance between the first layer of graphene and SiC substrate is approx. equal to 1.43 Å, this value is given differently in different papers, so the main criteria was the maximum distance on which we could get covalent bonds between layers. The distance between the first and the second graphene layer is equal to 2.7 Å on this distance. The next structure we are focused on is graphene on step shape SiC. The main problem here is to save proper structure of SiC and graphene. Because of the different lattice constant, it is very difficult to make sure that structure is periodic in all directions. We have to reduce a number of atoms as much as possible to minimize the time of calculations. So graphene was a little bit stretched. Then the structure was also passivated by hydrogen and optimized by minimization of Brenner potential. In the case with planar structure the minimum max force component was reached is 1.0899 eV/Å, for step structure it is 3.3424×10-4 eV/Å. In order to minimize the time of calculation, we used Extended Hückel method in both cases. We use Cerda.Carbon[graphite] basis with vacuum level -7.36577 eV, Cerda.Hydrogen [C2H4] basis with vacuum level -6.2568 eV and Cerda.Silicon [GW SiC] basis with vacuum level -6.14175 eV, following the QuantumWise manual recommendation. We used *k*-point sampling: *n*A = 10, *n*B = 3 and *n*C = 100 for flat structure and *n*A = 4, *n*B = 4 and *n*C = 100 for step structure. We picked these values empirically trying to find compromise between accuracy and computational time. We used FFT2D as a Poisson equation solver, which uses periodic boundary conditions in front,

back, bottom, top and Dirichlet in left and right. We also need to make sure that periodic condition in top and bottom direction does not affect our structure by extending the cell borders respectively. We calculated transmission spectrum and I/V curve.

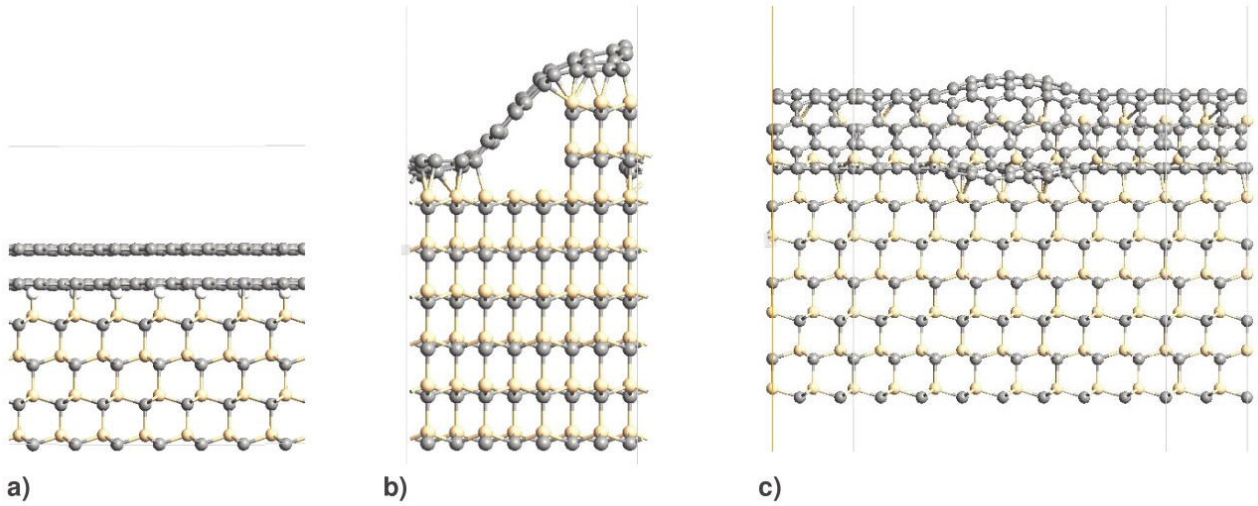

Figure 50. Results of molecular mechanic simulation of **a)** bilayer graphene on hydrogenated planar SiC substrate, **b**, **c)** step shaped non-hydrogenated non planar SiC substrate (front and side view).

The obtained transmission spectra for the planar and non-planar hydrogenated structures are in the **Figure 51**. As we can see in the **Figure 52a**, the I/V curve coefficient of step-shaped structure is approx. 0.075 S, which is almost twice less than for the flat structure. From the calculated results it can be deduced that SiC is conductive on energies higher than 1 eV. The **Figure 52b** describes the base state of electron wave function in the step-shaped non-hydrogenated SiC/ graphene interface.

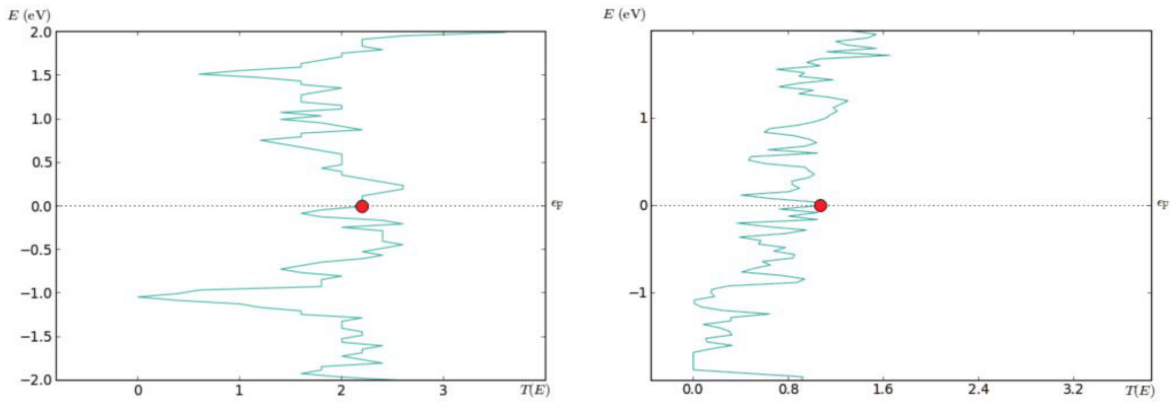

Figure 51. Transmission spectra for structure with hydrogenated **a)** planar SiC/bilayer graphene interface, **b)** step-shaped SiC/graphene interface

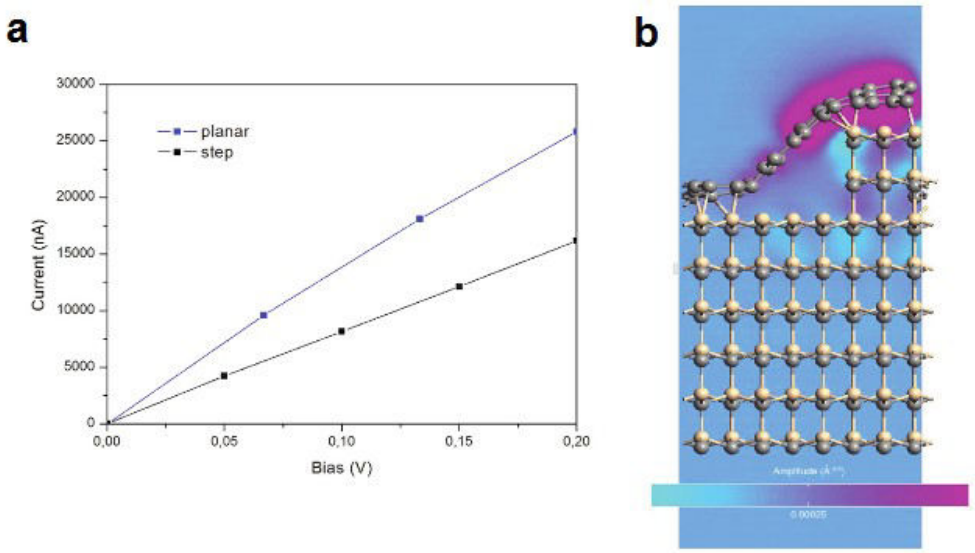

Figure 52. a) Comparisson of the I/V curves of structure with planar hydrogenated SiC/bilayer graphene interface (blue) and structure with hydrogenated step-shaped SiC/graphene interface (black). **b)** Base state electron wave function in the structure with step-shaped SiC/graphene interface.

Our results were compared with the experimental data. The transmission property was selected to evaluate the accuracy. We can look more precisely at resistivity of the graphene nanoribbon. Our calculation shows that the coefficient of I/V curve of step-shaped structure is approx. 0.075 S, which is almost twice less than for the flat structure. Experimental data from the article [58] gives us a value of 26 kΩ for the graphene sample of length 1.6 μm and width 39 nm. If we take into account that our step structure model is 1000 times shorter and 20 times narrower, our value of resistance (13Ω) has the same order but is still a bit smaller than the experimental one. The reason is that the collision of electrons with phonons are not taken into account as well as the temperature of environment and other unideal conditions which we can meet in the real case. These data can be used for continuous investigation of graphene on SiC properties.

5.1.4 Effects of External Fields

In [26] we may also find the study of an external field effects. The bandgap of bilayer graphene can be tuned by electric field in perpendicular to the basal plane (e.g. by placing a gate electrode). The symmetry of sublattice in AB stacking is broken by electrical field. The electrical displacement fields in different graphene layers produce two effects inducing a net carrier doping (shift in Fermi energy) and generation of non-zero bandgap. The gate-tunable bandgap can reach 250 meV and has the unusually strong oscilation strength for the bandgap transitions. Thus tuning bilayer graphene under electrical field can enable novel nanophotonic devices for infrared light generation, amplification and detection. Using a double-gate configuration, an insulating state with large suppresion of the conductivity in bilayer graphene can be further achieved. We investigated effects of voltage bias and external mechanical force on graphene nanoribbons and helicenes, and it is more discussed in the **Chapter 5.5**.

5.2 Carbon Nanotubes

Citing form the literature [59], a single walled carbon nanotube (SWNT) is in principle a rolled graphene sheet. Although the growth mechanism is mostly not based on rolling graphene, the way the graphene sheet is rolled determines the fundamental properties of the tube.

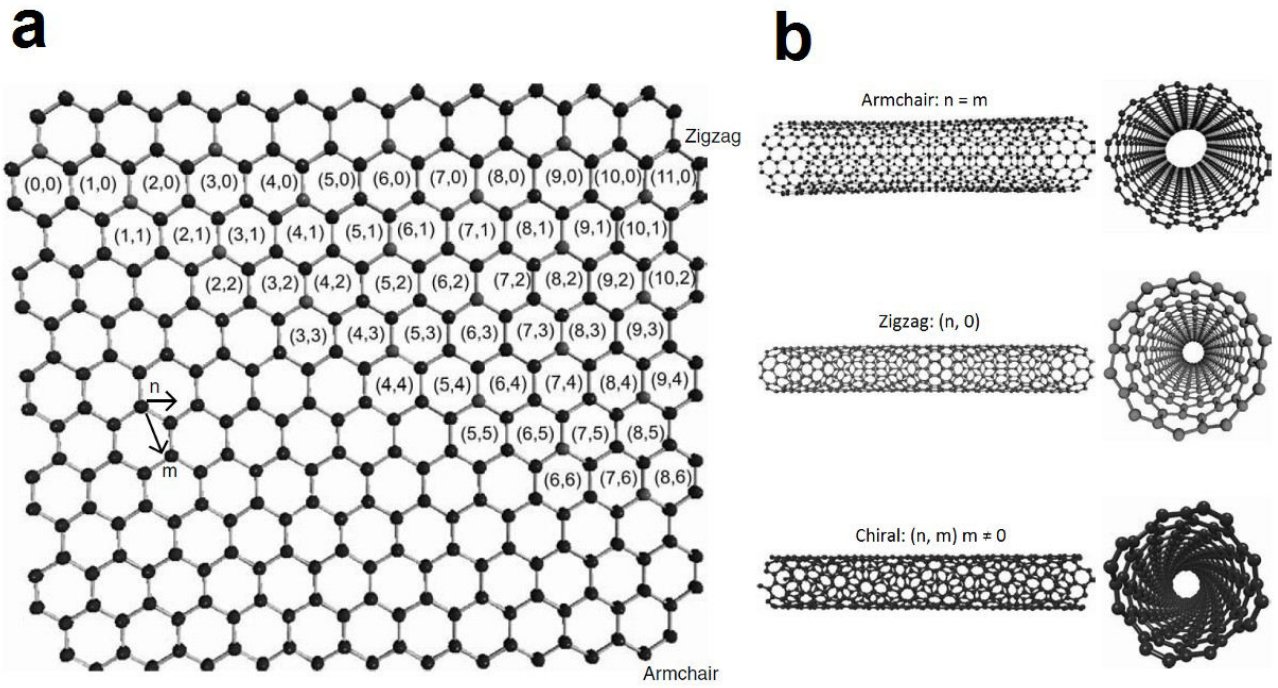

Figure 53. a) Graphene sheet labeled with integers (*n*, *m*). **b)** Examples of the three types of SWNTs identified by the integer values *n* and *m*. The picture is taken from [59].

In order to describe such a fundamental characteristic of the nanotube, two vectors, $\boldsymbol{C_h}$ and $\boldsymbol{T}$, whose rectangle defines the unit cell (**Figure 53a**), can be introduced. $\boldsymbol{C_h}$ is the vector that defines the circumference of the surface of the tube connecting two equivalent carbon atoms, $\boldsymbol{C_h} = n\hat{\boldsymbol{a}}_1 + m\hat{\boldsymbol{a}}_2$, where $\hat{\boldsymbol{a}}_1$ and $\hat{\boldsymbol{a}}_2$ are the two basis vectors of graphite and *n* and *m* are integers which are also called indexes and determine the chiral angle

$$\theta = \arctan\left(\sqrt{3}\left(\frac{n}{2m+n}\right)\right) \quad . \qquad \textbf{(104)}$$

The chiral angle is used to separate carbon nanotubes into three classes differentiated by their electronic properties: armchair ($n = m$, $\theta = 30°$), zigzag ($m = 0$, $n > 0$, $\theta = 0°$), and chiral ($0 < |m| < n$, $0 < \theta < 30°$) (Figure 15b). Armchair carbon nanotubes are metallic (a degenerate semimetal with zero band gap). Zig-zag and chiral nanotubes can be semimetals with a finite band gap if $n - m/3 = i$ (i being an integer and $m \neq n$) or semiconductors in all other cases. The band gap for the semimetallic and semiconductor nanotubes scales approximately with the inverse of the tube diameter, giving each nanotube a unique electronic behavior. The diameter of the nanotube can be expressed as

$$d_t = \sqrt{3}\left[a_{C-C}\frac{\sqrt{m^2+mn+n^2}}{\pi}\right] = \frac{C_h}{\pi} \quad , \qquad \textbf{(105)}$$

where C_h is the length of $\boldsymbol{C_h}$, and $a_{C\text{-}C}$ is the C-C bond length (1.42 Å). Combining different diameters and chiralities results in several hundred individual nanotubes, each with its own distinct mechanical, electrical, piezoelectric, and optical properties. As it is mentioned in [60], a novel material, graphene nanoribbons encapsulated in single-walled carbon nanotubes (GNR@SWNT), was synthesized using confined polymerization and fusion of polycyclic aromatic hydrocarbon (PAH) molecules. Formation of the GNR is possible due to confinement effects provided by the one-dimensional space inside nanotubes, which helps to align coronene or perylene molecules edge to edge to achieve dimerization and oligomerization of the molecules into long nanoribbons. Almost 100% filling of SWNT with GNR is achieved while nanoribbon length is limited only by the length of the encapsulating nanotube. The PAH fusion reaction provides a very simple and easily scalable method to synthesize GNR@SWNT in macroscopic amounts. First-principle simulations indicate that encapsulation of the GNRs energetically favorable and that the electronic structure of the encapsulated GNRs is the same as for the free-standing ones, pointing to possible applications of the GNR@SWNT structures in photonics and nanoelectronics.

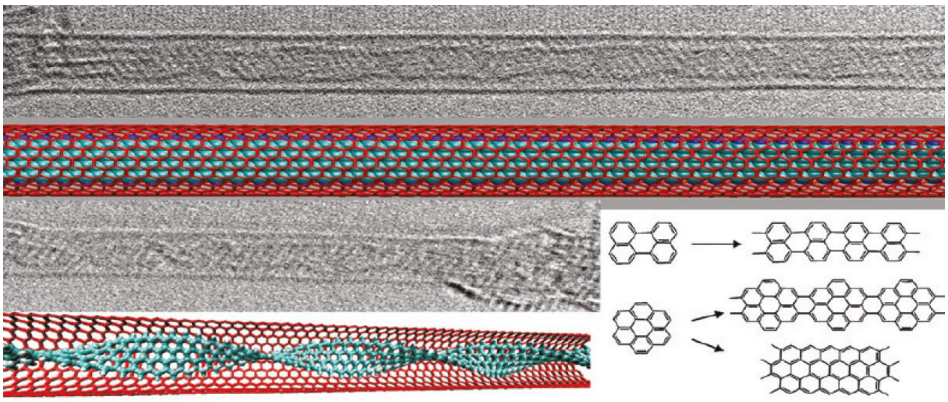

Figure 54. TEM images and wire models of GNRs encapsulated in SWNT obtained using coronene precursor (above) and perylene precursor (below). The image is taken from [60].

5.3 Fullerenes

An infinite number of spherical fullerenes are believed to be able to exist. Known forms include C_{60} (**Figure 55a**), C_{70}, C_{76}, C_{84}, C_{240}, and C_{540}. All fullerenes consists of 12 pentagonal faces and varying number of hexagonal faces. In general, for a fullerene C_n there will be 12 pentagonal faces and half of n minus 10 (n/2-10) hexagonal faces, thus, the C_{60} fullerene has 12 pentagonal faces and 20 hexagonal faces [61].

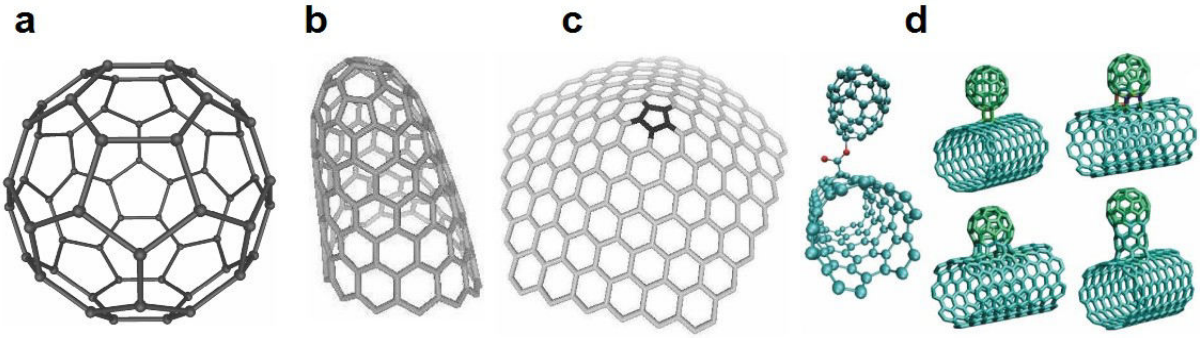

Figure 55. a) Fullerene C_{60}. **b)** Carbon nanohorn. **c)** Carbon nanocone. **d)** Carbon nanobuds. The picture is taken from [61].

Fullerenes have a rich and complex chemistry. C_{60} behaves like an electron deficient alkene, reacts readily with electron rich species, and participates in many reactions (e.g. oxidations, reductions, nucleophilic additions, electrophilic additions, Diels-Alder reactions, and Friedel-Craft alkylations). This rich chemistry permits a wide range of fullerene functionalization and opens the way to designing functionalized fullerene for specific properties and purposes. The applications include organic photovoltaics, polymer electronics, antioxidants, biopharmaceuticals, antibacterials, HIV inhibition, catalyst, water purification, MRI agents, optical devices, scanning tunneling microscopy, and atomic force microscopy [61].

A structure closely related to fullerenes is carbon nanohorn (**Figure 55b**). Many structures related to the basic fullerenes and the carbon nanohorn have been discovered. For example, the carbon nanocone (**Figure 55c**) and "NanoBuds" (**Figure 55d**) created by combining carbon nanotubes and fullerenes. The resulting nanobuds possess properties of both materials (e.g. electrical conductivity of carbon nanotubes, chemical flexibility of fullerenes). Fullerene composites and hybrid materials, such as a fullerene-dendrimer-mesoporous silica hybrid, have been described.

Authors of [62] show, that there is the possibility of filling the inner space of the SWCNTs with fullerenes (Figure 18). The existence of such structure had been long speculated prior to its actual discovery. The speculations were fueled by the capability of fullerenes themselves of retaining atoms or molecules inside. This structure is called endohedral fullerene, refering to the icosahedral C_{60} symmetry. Such materials are denoted as $A@C_x$ where A marks the encapsulated atom or molecule and x = 60, 70 is the index of fullerene. C_{60} fullerenes encapsulated insude SWCNTs were discovered using high resolution transmission electron miscroscopy and this discovery soon led to the birth of a vivid new field within the nanotube research called the peapods which then led to a number of breakthroughs in the study of optical, electronic, and transport properties of the SWCNTs and to a number of applications.

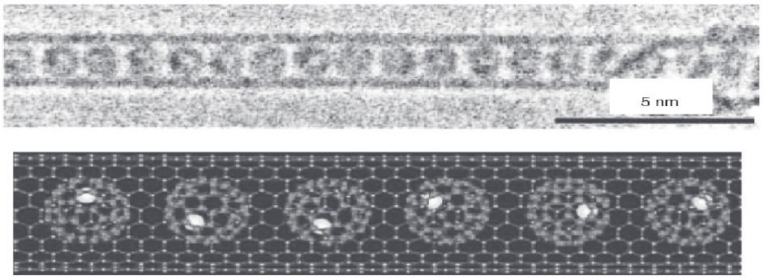

Figure 56. HR-TEM micrograph and schematic representation (not to scale) of $Gd@C_{82}$ metallofullerene peapods. Dark spots in micrograph (white in schematic) correspond to the heavy Gd atoms. The image is taken from [62].

As for the demonstrated applications, SWCNTs are ideal building blocks for nanoelectronics given their small size and their high current-carrying capability. There are three obstacles for the applicability though: the inability of patterned growth and contacting, the random chirality (and thus conductivity) distribution of tubes and the relatively large (above 1 eV) direct bandgap of semiconducting tubes. Modern electronics tends to use small gap semiconductors for increased speed and reduced dissipation. The band gap problem was overcome by means of metallofullerenes inside the SWCNTs (reducing to band gap to 0.1 eV). Further, according to [62], the transistor behavior of this metallofullerene peapod system was also proven. The other demonstrated applications are in solar cells. The fullerenes encapsulated inside SWCNTs act as the active electron-hole producing medium. This means that peapods alone can act as solar cells as they

have the active medium as well as the electrode naturally integrated. Although this effect requires further studies and in particular benchmarks for quantum efficiency for the light induced electron transfer, it shows a high application potential of peapods for solar cell purposes. The next demonstrated application is drug delivery which is given by the biocompatibility of the carbon nanotubes, the possibility to attach the active molecules to the nanotubes (as the SWCNTs have a high specific surface area) and the possibility to track the carbon nanotube in vivo (e. g. by fluorescence spectroscopy).

There are also some expected applications of these structures like photonic crystals. Photonic crystals refer to materials where the periodic array of their constituents give rise to a periodic modulation of the dielectric constant. This results in unique optical properties such as, for example, well-defined gaps in the transmittance in a manner analogous to the band gap behavior of solids. Peapods were suggested to be used as photonic crystals thanks to the periodicity of the encapsulated fullerenes which is well-defined. It was found that the periodicity and the dielectric properties of C_{60} fullerenes give rise to an optical gap around 7 nm which means that soft X-rays with this wavelength could be trapped inside the peapods. This means that if an effective medium, which emits radiation with this wavelength, is placed within the peapod structure, the emitted radiation would be amplified such as in a laser, which could provide a way to construct a soft X-ray laser.

Another application is so called shuttle memory device. Early dynamic observations of the behavior of encapsulated fullerenes by TEM showed that they were able to move back-and-forth in the SWCNT cavity, presumably upon random ionization effects due to electron irradiation in the TEM. The name shuttle describes the fact that the encapsulated C_{60} switches between the different bit values by rapid shuttling. For more details see [62].

As it is further noted in [62], another possible application is for high-frequency oscillators. Interest turned toward utilizing carbon structures for oscillator purposes motivated by the demonstration of very low friction in coaxial multiwall carbon nanotubes. For example, double-wall carbon nanotube structures were considered and studied using molecular dynamics calculations and it was shown that a (9,0) nanotube inside an (18,0) would behave as a 38 GHz nanooscillator. A peapod-based oscillator was proposed and a fundamental eigenfrequency of 50 GHz was found for the C_{60} motion inside a 5 nm long section of a (10,10) SWCNT. In a recent work, the evidence for nanoelectromechanical coupling in peapods has suggested them as NEMS resonators, with an operation frequency set by the vibrational motion of the encapsulated fullerenes in the 100 GHz range. The major obstacle in this approach is difficult control of the C_{60} motion externally.

Quantum computing is the next possible application of peapods. Quantum information processing can be divided into quantum computing and quantum information storage. Both areas require the availability of true quantum variable or qubit (e. g. atomic state, a supercurrent, photon polarization, or a spin). For information storage, a high level of decoupling of the quantum variable from the environment is desired. For information processing, a number of the quantum variables has to interact in order to form an entangled state on which the calculation proceeds. There are two potential challenges in quantum computing: upscalability and decoherence. Practical calculations require a large number of qubits, which however increases complexity and also the decoherence due to the increased level of interactions, thus these two objectives are somewhat exclusive. There is a suggestion to prepare a linear chain of spin qubits for QC. It

was proposed that a single qubit would contain a $N@C_{60}$ endohedral fullerene. In this molecule, the atomic nitrogen is remarkably decoupled from its environment due to the protecting shielding of the fullerene cage. The utility of this molecule for quantum computing has been already demonstrated.

5.4 Annulenes

According to [63], [*n*]annulene is a monocyclic hydrocarbon comprised of alternating single and double bond where the number in brackets denotes the number of continuous sp^2 carbon centers. By definition, cyclobutadiene is therefore considered as [4]annulene, benzene (**Figure 57a**) as [6]annulene, etc. Replacement of one or more of the double bonds with an acetylene unit affords a dehydroannulene (**Figure 57b**). An unfortunate side effect of installing triple bonds in the hydrocarbon skeleton often is compound instability. On the other hand, fusion of one or more benzene rings to furnish a benzoannulene (**Figure 57c**) or dehydrobenzoannulene (**Figure 57d**) heightens macrocycle stability in general.

The main factor driving the early annulene research was the dominating question of whether planar examples of such macrocycles were able to sustain induced ring currents, and if so, what was the strength of those ring currents. The main conclusion was that ring currents in these systems became progressively weaker upon benzannulation, by inclusion of triple bonds, and/or with increasing ring size. A number of discoveries in the last few decades made the previously laborious task of macrocycle assembly now a quick and efficient process. The ability to create new annulenes allowed chemists to easily functionalize the hydrocarbon backbone and thus tailor the chemical reactivity and physical properties of the macrocycles. Recognition of potential materials applications for these π-electron-rich systems has driven most of the annulene research conducted currently. Annulenes have been shown to exhibit nonlinear optical behavior, polymerize yielding tubular polymers, and even explode furnishing ordered carbon nanostructures.

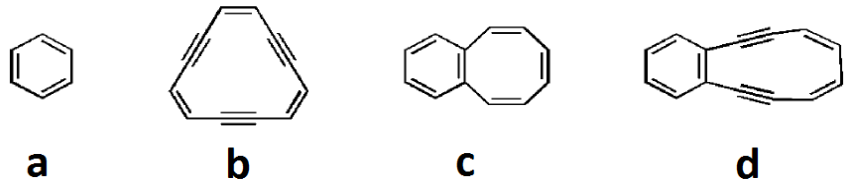

Figure 57. Various annulenes: **a)** [6]annulene (benzene), **b)** Dehydroannulene, **c)** Benzoannulene, **d)** Dehydrobenzoannulene. The image is taken from [63].

Because it is further addressed later in this work, let us use the [18]annulene (**Figure 58a**) as an example. According to [63], it represents an unique target of study due to its status as not only a $(4n + 2)$ annulene but also a member of the aromatic subgroup $6(2p + 1)$ in which the D_{6h}-symmetric point group is allowed without severe nonbonded interactions. As annulene ring size increases, aromatic stabilization energies drop off and bond length alteration becomes more pronounced. An ongoing debate has centered on the ring size at which polyolefin-like, localyzed π-electron structures predominate over fully delocalized conjugation. Put simply, it is the question of the point at which drawing a closed circle inside the ring rather than alternating double and single bonds becomes inappropriate. Computational and theoretical estimates ranging from [30]annulene all the way down to [10]annulene have been put forward. More and more front lines of this debate take root at or near [18]annulene.

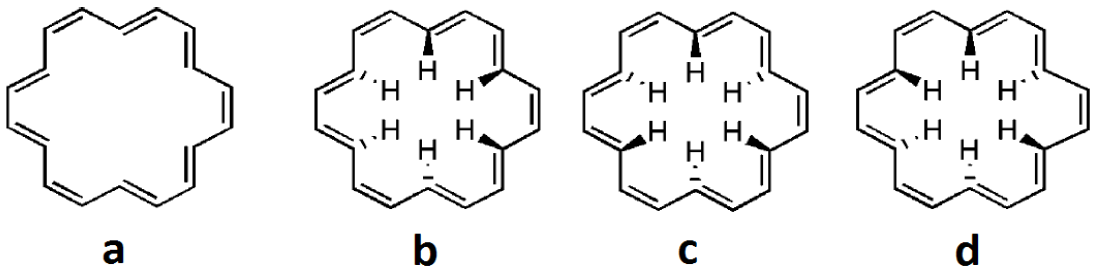

Figure 58. [18]Annulene. **a)** Basic structure. **b-d)** Some possible hydrogen arrangements. The image is taken from [63].

Early studies predicted the unlikelihood of planar D_{6h} [18]annulene due to steric interactions between the internal protons. More recently, low-temperature NMR studies have yielded three confirmations of nearly equal energy with three internal protons above the plane and three below in three possible arrangements (**Figures 58b-d**). Furthermore, upon synthesis, chemical evidence revealed reactivity typical of localized π bonds (addition rather than substitution), behavior drastically different than benzene. It may be a bit suprising then that the X-ray crystal structure of [18]annulene, determined in early studies, showed a nearly centrosymmetric molecule distorted from planarity by 0.085 Å and a C_{3i} symmetry only slightly distorted from D_{6h} symmetry. The nonplanarity was explained by intermolecular nonbonded repulsions and crystal-packing forces. The crystal structure was recently reevaluated and although an additional minor form with slightly different geometry was found, [18]annulene was confirmed by the authors as having an essentially planar aromatic structure in the crystal. The 12 inner C-C bonds were determined to have lengths of 1.385 Å and the 6 outer bonds lengths of 1.405 Å, relatively close to the originally determined geometry. The average C-C length is similar to benzene. The ring internal and reentrant angles are 124.0° and 127.9° respectively.

But these results are disputed (as being a special case where the D_{6h} symmetry may occur) because of the new results obtained by GIAO-B3LYP/6-311+G** methods pointing that only C_{2h} symmetry can give acceptable results and previous data were affected by apparent higher symmetry (given by used experimental method) and time-averaged structure. Even more recent work disputes these assertions by offering that it may in fact be possible to distinguish inversion disorder effects from true single structure at currently attainable resolutions. In addition, there is noted that computation regards molecules as being in the gas phase and that the small barier to symmetrization could be overcome by π-π stacking and favourable crystal packing forces (i. e. driving the molecules in the crystal towards centrosymmetric forms with non-alternating character). If bond alternation does indeed exist in [18]annulene and then vanishes upon crystallization, it would be an extremely unusual phenomenon with implications for solid-state nuclear magnetic resonance. Clearly, further computational efforts are in order.

The higher annulenes (n > 18) present less synthetic interest, mostly due to their significant bond alteration, asymmetry, and conformational flexibility. All annulenes up to n = 30 (**Figure 59**) have been synthesized except n = 26 and 28. Most of the recent work has been computational in nature and aims at understanding the complex interplay between geometric, energetic, and magnetic properties. Aromatic stabilization energies are greatly reduced in the larger systems, and it is believed that the mixing of low-lying excited states and ground states leads to pseudo-Jahn-Teller distortions. The search for discrete transition point between delocalized and localized structures prompted a computational study

that investigated bond length alteration in large annulenes up to n = 66. Various levels of theory and basis sets were sampled. While B3LYP/6-31G* acceptably predicted bond lengths of known ring sizes and oligoenes, Hartree-Fock methods consistently provided clearly incorrect (and at times impossible) values. Using experimental measurements as guides, DFT calculations accurately quantified the bond length alteration ($\delta = R_{single} - R_{double}$) of the minimized structures of both ($4n$) and ($4n + 2$) annulenes as a function of ring size. In the progression of ($4n + 2$) annulene. Conversely, an enforced $\delta = 0$ produced a local maximum for [30]annulene to [66]annulene in the energy profiles. δ values for the lower ($4n + 2$) annulenes are essentially zero and thus not reported. The [30]annulene is the most likely candidate for the transition point to localized, yet still aromatic, structure. Surprisingly the calculated aromatic stabilization energies do not decrease with inreasing ring size but increase up to [18]annulene and then converge to a limiting value of about 23 kcal/mol. This provides further evidence that total delocalization is not required for aromaticity.

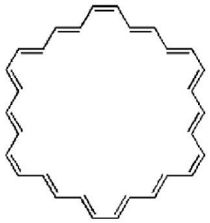

Figure 59. An example of higher annulene: [30]Annulene.

We analyzed electronic transport properties of graphene nanoribbons (GNR) patterned by [6+*N*x12]annulene-like quantum antidots in one of our published articles [A4]. We tried to simulate [18]annulene, [30]annulene and [42]annulene antidots placed on passivated graphene nanoribbon of appropriate width and length. Our results are predicting electronic transport properties similar to graphene. It is shown by analyzing the GNR transmissivities calculated by Extended Hückel Self-consistent Field model (EH-SCF). These structures can be used in future as a high precision molecular sieve for separation of almost any size of molecule because of its holes modifiable by using different [6+*N*x12]annulenes. The sieving can be potentially controlled and/or measured by the changes of potential and/or current flow in chosen GNR layer of the sieve. These structures can be potentially usable for water desalinization, separation of industrially exhaled gases or for mining rare metals from ocean. It can be used as well as a totally new carbon-based nanomaterial with potentially interesting mechanical, optical or electronic transport properties and compatible with graphene. These structures can be prepared by the means of ion (or electron) beam lithography or by the bottom-up approach from chemical precursors in the future.

If we treat graphene as infinite number of benzene molecules, let us assume annulene net as is some kind of extension of graphene where we are connecting together annulene molecules, in right way. By this idea, we can construct a thin layer, which has periodic structure somehow comparable with graphene. In our simulations we are trying to show, that this material is not just possible to construct (as it is a stable form of carbon) but also has similar properties as graphene itself. By checking the molecular dynamics, we can say, that at least [18]annulene, [30]annulene and [42]annulene can be used to form a carbon net with planar structure and minimal interatomic force involved. When confronted with this result, we tried to simulate the electronic transport properties (such as transmissivity, electron density and current transmission pathways) and to compare with graphene. We are trying to show, that annulene nets can be useful material for molecular sieves (with similar properties as zeolites) and for construction of lab-on-chip systems, where it can be used for precise electrically controlled flow of certain reactants. These nets can be as well used for desalinization or

filtering of industrial exhalations in the future and for improvement of the graphene electronics, because it is presumed to be lighter than graphene (simply fewer atoms in same area) and it should have all the advantages of two-dimensional material, such as surface plasmon excitation.

We selected the proper structure, placed the carbon atoms in the original positions and passivated all the free bonds with hydrogen atoms. In order to reach the thermodynamical equilibrium of the system, the optimized atom positions are computed by molecular mechanics. We used embedded Brenner`s quick geometry optimizer so that the maximum component of the interatomic force was less than 10^{-8} eV/Å in all cases after the optimization. For electrical properties calculations we used semi-empirical EH-SCF method for nanoscale devices with spin polarization considered [17]. Due to the used method, we need to extend the electrodes into the structure. In order to consider the electrodes as a bulk region, there is need to have enough space in the central region for both electrode extensions. Depending on the structure, this length for extension should be at least about 5 to 10 Å. It is 10 Å for [18]annulene structure, 7.38 Å for [30]annulene and 7.5 Å for [42]annulene in our simulations. Atom in the electrode extension is identical to the one in the electrode (shown on the **Figure 22** as the red dots). We tried to fuse the annulene net to graphene electrodes made of ZGNRs of appropriate width. In order to simulate the situation where electrodes are made of GNRs, we need to leave the atoms involved in electrodes without change. Thus the first three atoms from both sides of the structure are left without defects and they are only affected by dynamics of the whole system which mostly means small linear stretching over the *z*-axis. The first analyzed structure we may see in the **Figure 60**.

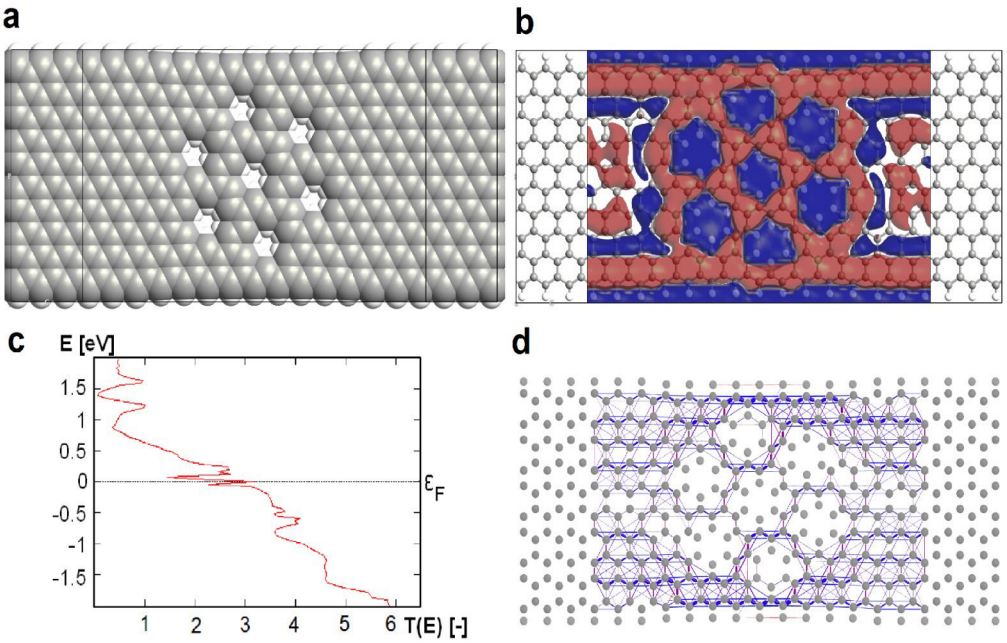

Figure 60. a) Simulated system with visible Van der Waals radii. **b)** Electron difference density isosurface with value -10^{-5} Å^{-3}. **c)** Transmission spectrum for both spins (identical). **d)** Transmission pathways for zero energy level.

The second analyzed structure is the 16ZGNR structure with 7 symmetrically deployed [30]annulene patches along 18 atoms wide central region as shown on the **Figure 61a**. Van der Waals radii show much greater pores to emerge. Width of those pores should be around 8.46 Å and thus provide space for greater molecules to past thru. From the **Figure 61b** we can see isosurface of electron difference density for value -10^{-5} Å^{-3}. We obtained transmission spectrum (**Figure 61c**) with visible depression at Fermi level. **Figure 61d** shows how the current is flowing in the ribbon at zero energy $\varepsilon = 0$ eV.

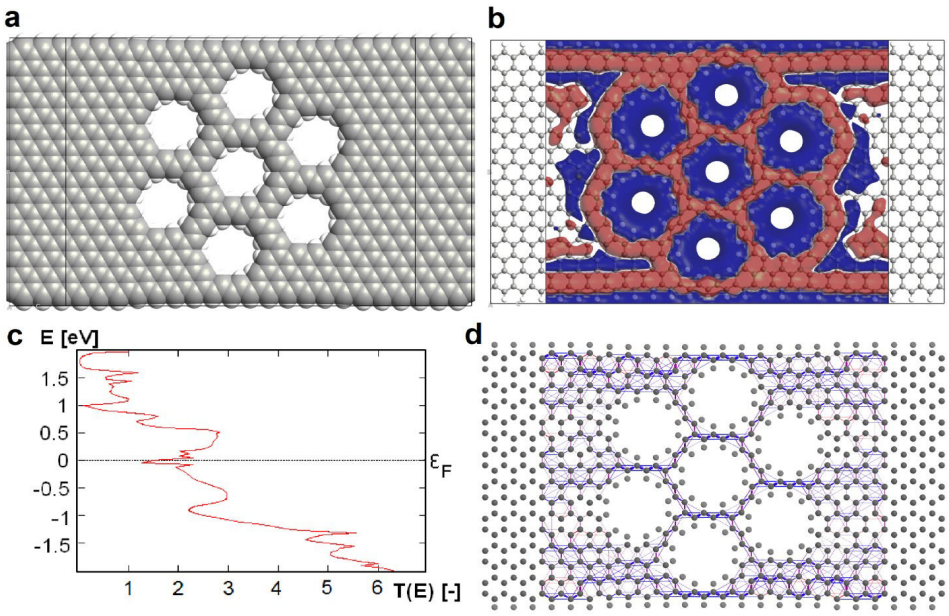

Figure 61. a) Simulated system with visible Van der Waals radii. **b)** Electron difference density isosurface with value -10^{-5} Å^{-3}. **c)** Transmission spectrum for both spins (identical). **d)** Transmission pathways for zero energy level.

The third analyzed structure is the 22ZGNR structure with 7 symmetrical deployed [42]annulene patches along 25 atoms wide central region as shown on the **Figure 62a**. From the **Figure 62b** we can see isosurface of electron difference density for value -10^{-5} Å^{-3}. We obtained transmission spectrum (**Figure 62c**) and **Figure 62d** shows how the current is flowing in the ribbon at zero energy $\varepsilon = 0$ eV.

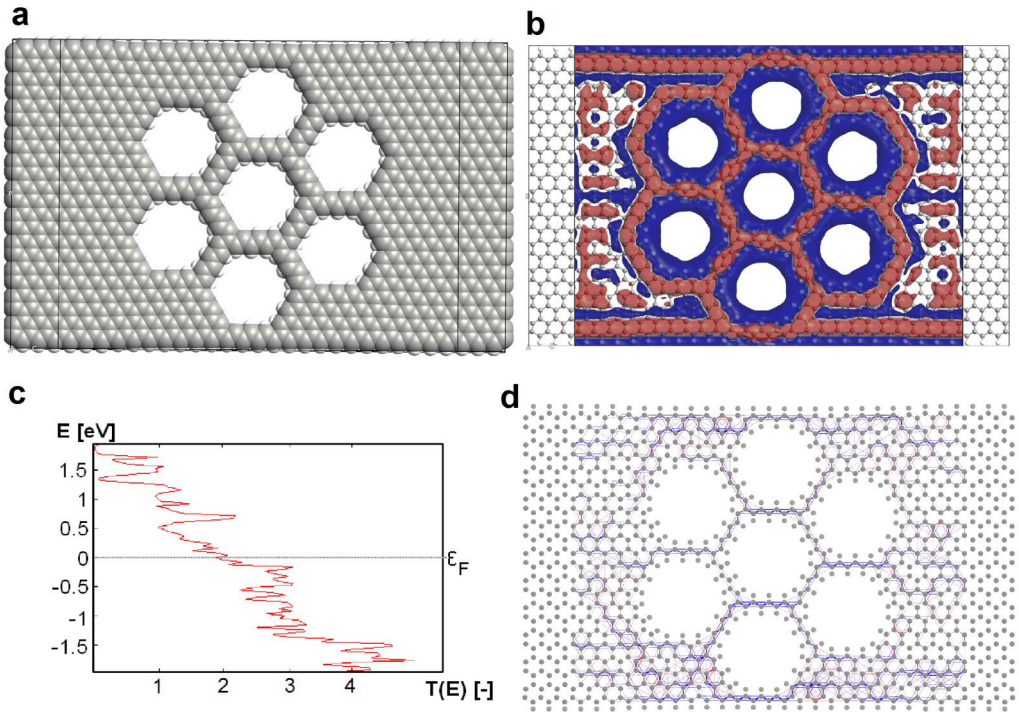

Figure 62. a) Simulated system with visible Van der Waals radii. **b)** Electron difference density isosurface with value -10^{-5} Å^{-3}. **c)** Transmission spectrum for both spins (identical). **d)** Transmission pathways for zero energy level.

Although this study was only a brief insight in to annulene-graphene structures, it shows that these are thermodynamically stable and can form larger structures. These structures should share some of the mechanical and electronic properties of graphene which implies future use as molecular sieves usable e.g. in industry exhalation sanitation, in precise molecular lab-on-chip systems, and for filtration of heavy metals from water and water desalinization. Another possible applications are also improvements of graphene-based technology. These structures can be prepared by means of ion (electron) beam lithography or by growth from chemical precursors.

5.5 Helicenes

In our recently published paper [A2] which extends our previous work on the topic of helicenes [A5, A6] we studied the properties of hybrid graphene-helicene nanosystem. Carbohelicenes are homocyclic aromatic but non-planar and naturally chiral hydrocarbons. The simplest carbohelicene with chemical formula C18H12 is named [4]helicene. The number in brackets denotes the number of ortho-fused benzene rings in the molecule. The helical chirality (helicity) of helicenes can be clockwise or counterclockwise, and corresponding enantiomers are denoted as M (minus) when left-handed and P (plus) when right-handed [64]. There are several comprehensive works describing helicenes synthesis, structure and applications [65, 66, 67, 68]. Similarly to GNRs, the ortho-annulated polyaromatic compounds like helicenes are interesting because their aromaticity implies electronic resonance features, stability, and π-π interactions along with the specific geometric properties and reactivity [69]. Helicenes are basis for a large family of molecules and may be used as precursors for more complex structures like helicoidal fibres [67] and nanowires [70], Möbius topology structures which conserve aromaticity [71], hexapolar structures [72], cages and tweezers able to contain other atoms and molecules [73, 74], and many other oligomers and polymers [75, 76, 77, 78, 79, 80]. Their thermal stability and oxidation resistivity makes them possibly utilizable for sensing [81, 82] and as ionophores [83]. The main field where they are found interesting is optoelectronics. Photochromic helicenes are investigated for chiral discrimination [84] and carbo[6]helicene derivatives with π-conjugated cyano-phenyl groups were explored for chiroptical properties [85]. The Langmuir-Blodgett aggregated helicene films are found to exhibit circular dichroism [86]. There are also theoretical papers describing second-order nonlinear optical properties of chiral films [87], and of benzannulated or selenophene-annulated expanded helicenes [88]. Helicenes may be functionalized photochemicaly [89]. Different substituents and function groups in [5]helicenes are shown to for allow control of its optical emmission properties [90, 91] and are promising perspectives in organic light-emitting diodes [92]. Similarly, in [93] authors present carbazole-based diaza[7]helicene as a material for deep-blue-emitting OLED. Oxa[5]helicene-based racemic glassy films are presented as a material for photothermally stable pervoskite solar cells [94]. Also the helicene-based imidazolium salt is explored as a material for organic molecular electronics [95]. The transistor responses of tetrathia[7]helicene and derivatives were described [96]. In [97] authors show potential-driven electrodeposition of conductive and non-conductive [7]helicene-derived polymers and similarly, electropolymerization method of immobilization onto carbon substrates has been introduced [98]. The methods of helicene gas phase synthesis [99], optically pure and enantiopure helicene preparation were recently developed [100, 101], as well as rapid synthesis of functionalized dibenzohelicenes [102], or synthesis of bi-azahelicenes by photocyclization [103]. Although being challenging, there is also a progress in synthesis of long helicenes. Oxa[9]-, [13]-, [17]- and [19]helicenes prepared by polycyclization are presented in [104], an organometallic route to [11]helicene [105] and one-step photocyclization-based synthesis of [16]helicene [106] have been achieved.

The effects of twist and strain on helicene and graphene nanoribbons and related structures are studied both theoretically and experimentally in several papers. Twistacenes (analogues of 2ZGNRs or acenes) [107] and helicenes [108] as well as helicene chains [109] are investigated for their intrinsic strain. The highly stretchable GNR springs and strained V-shape notched GNRs are investigated for various applications, e.g. for their piezoelectricity and flexoelectricity in pressure sensing [110, 111, 112, 113]. The strain-induced helically chiral polyaromatic systems are more explored in [114]. There are papers that predict non-monotonic energy gap change during compression and stretching [115] which leads to an U-shape current-to-strain relationship in helicenes [116]. Rulíšek et al. calculated energy change of [14]helicene and Gue et al. did similarly for [12]helicene by a different approach. We use these two publications as a reference to define parameters and to compare properties of our structures and they will be discussed in more detail later.

First, let us describe the investigated structures in more detail. The main goal of this paper is to study a simple freestanding ZGNR-helicene-ZGNR molecular junction which will be as close as possible to physical reality. Although the free-standing graphene itself forms wrinkles on a large scale and in the result it is not strictly planar, the graphene nanoribbons several atoms wide with no defects and in vacuum will be considered as planar in this perspective. We want to conserve the aromaticity of the whole structure and get a junction which could be possibly modulated by outer action, in this case by compression and stretching. One condition is to ensure the possibility of periodic prolongation in all directions, which means to place enough vacuum space and/or ensure smooth sp^2 bonding to get the lowest possible interatomic forces on all borders of the simulation cell. We want to build a system with no exocyclic parts and no unintended defects. Given the high number of planar polyhex variations, we need to use a minimal configurations only, both to save computing time and to find a trivial systems from which more complex could be later derived, but we also want to include a helical turn in the central region, to test its properties. We also decided to study only symmetrical structures with (P) helicene enantiomers, as we believe that these structures may provide insight even to the omitted set of structures. For the purpose of navigation through the structure, we labeled the helicene outer carbon atoms suitable for bonding to ZGNRs by letters A to F, as shown in the **Figure 63**. To build up the defined central region we first have to think about carbohelicenes and their symmetries. As we can see in the **Figure 63e**, if we want to include a helical turn in the final structure, there is just one way how to fuse [4]helicene with the two 2ZGNRs, resulting in symmetric axial stretchable electrodes configuration. The terminal carbons of left and right 2ZGNRs must fuse with A2, B2 and A1, B1 carbons of [4]helicene respectively. While looking at the final structure we may notice that when fused in the same linear fashion with these ribbons, the same configuration would stand for the case of [*n*]helicenes, where $n = 5$, 6, 7 and 8. This is an interesting result, as when freestanding, the structural characteristics of all these molecules in fact differ (see **Table 2**). The same stands for [10]helicene (**Figure 63f**). Fusing the molecule with the ribbon all at once examines also configurations with [*n*]helicenes, where $n = 11$, 12, 13 and 14. We may therefore state to also have found properties of these configurations.

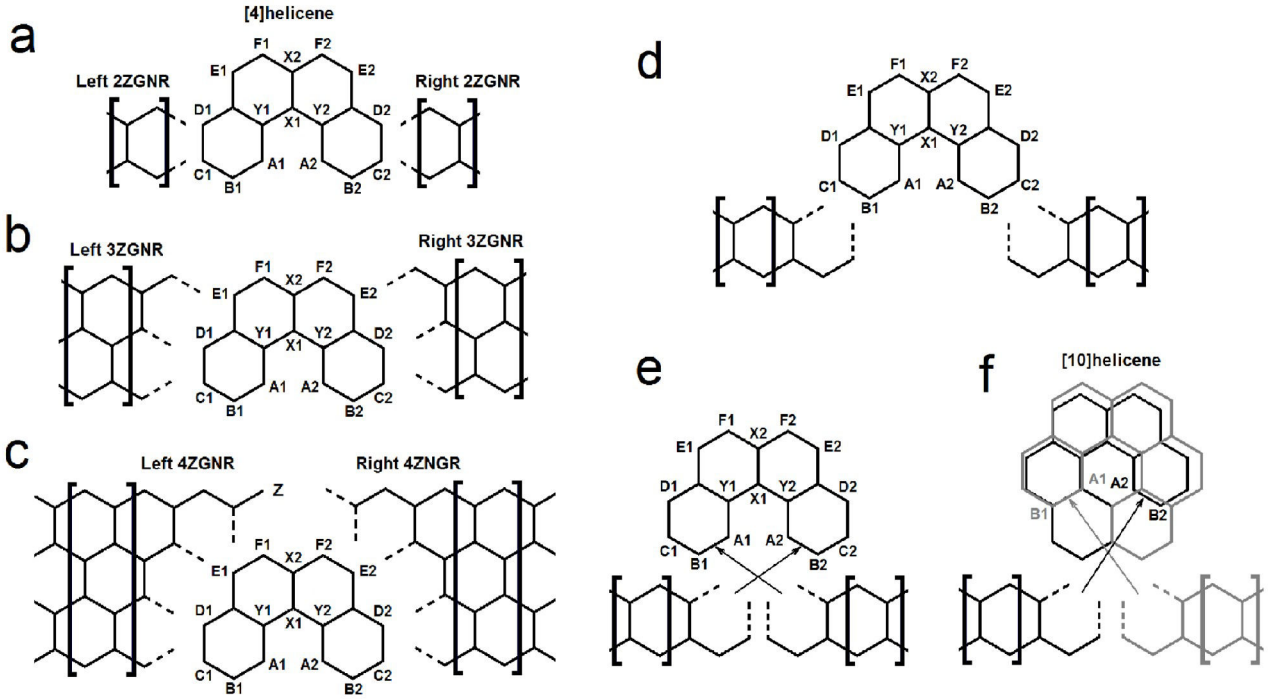

Figure 63. On the variants of fusing [4]helicene resp. [10]helicene with two ZGNRs.

There are also other possibilities how to fuse 2ZGNRs with [4]helicene. The terminal carbons of left and right 2ZGNRs may fuse e.g. with B1, C1 and B2, C2 respectively (**Figure 63d**) or C1, D1 and C2, D2 respectively (**Figure 63a**). This does not lead to a helical turn configuration, however it leads to steric hinderance in the central region as well because the A1, A2 hydrogens preserve the original [4]helicene chirality. The 2ZGNR-based structures which include fused E, F carbons lead to similar helicene chains as described in [109]. For all the variants of [4]helicene ortho- and/or peri-fused with 2ZGNR which share electrodes in side-to-side directions see the **Table 1**. More details on polyhex hydrocarbons are available in the literature [117].

Now let us assume that we want to include [4]helicene in wider ZGNRs. We may see (**Figure 63b**) that when two 3ZGNRs are fused with carbons C, D and E, we actually get a V-shape notched graphene nanoribbon. Similar structures are investigated e.g. by authors of [111]. Likewise, we may expand this to 4ZGNRs and fuse them accordingly with carbons C, D, E, F, and through carbon Z to get the same constriction in a wider ribbon (**Figure 63c**) and so on. This expands (*m*)ZGNR in the opposite side of A1, A2 steric hinderance region, and we presume that with increasing m, the total conductance would increase and the [4]helicene would have a constant impact on it, in the form of a single edge defect. There is also possible to extend (*m*)ZGNRs on the A1, A2 side of [4]helicene and get a set of configurations where the central part of [4]helicene forms a short 2ZGNR bridge on top. We presume that with increasing *m*, this configuration leads to quick saturation of conductance because there is nothing to contribute to the total conductance, except for the influence of quantum mechanical tunneling through a wider structure. In the same fashion, we may expand (*m*)ZGNRs starting with the **Figure 63d** configuration. This leads to the similar configurations like before, where, when expanded on the A1, A2 steric hinderance region side, the impact of ZGNRs expansion on total conductance is presumably negligible and when expanded on the opposite side, expansion of ZGNRs leads to the increase in total conductance by adding more transmission pathways to the nanostructure.

	A1B1	B1C1	C1D1	D1E1	E1F1
A2B2	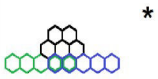	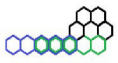			
B2C2	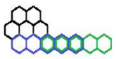		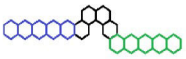		
C2D2		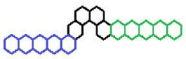		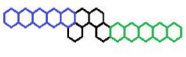	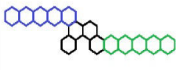
D2E2	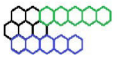				
E2F2		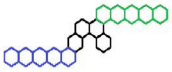			

Table 1. The schematic enumeration of [4]helicene (black) ortho- and/or peri- fused with two 2ZGNRs (blue & green) which share side-to-side directions. The structures on diagonal have symmetric and axial electrodes configuration. Except for the first structure, the 1st row and 1st column structures have non-axial electrodes configuration. Except for the last structure which has three, structures in the last row and last column have two steric hinderance regions (multiple helical elements). Electron transport properties of structures marked by asterisk were calculated.

The 3D nature of molecules used in the central region determines that, in order to have minimal unintended impact on it from the side of electrodes, we have to allow it to have sufficient space. While building up a relaxed structure, we also need to consider that in non-equilibrium conditions, e.g. with compression of the central region, the necessary space needed may increase because of the electrodes deformation. From experiments and DFT studies [115] we know that neutral helicenes and their cations tend to have slightly more benzene rings in one helical turn (approx. 6.05 to 6.08) and anions vice versa. This is determined by the twist angle; positive for neutral and cations, negative for anions. This fact will forbid us to have both perfectly axial electrode directions and perfectly relaxed structure at the same time, and thus we believe our optimized structures to be the best compromise. In the **Figure 64** we may see impact of chosen electrodes on twist angle and interpitch distance of helicene.

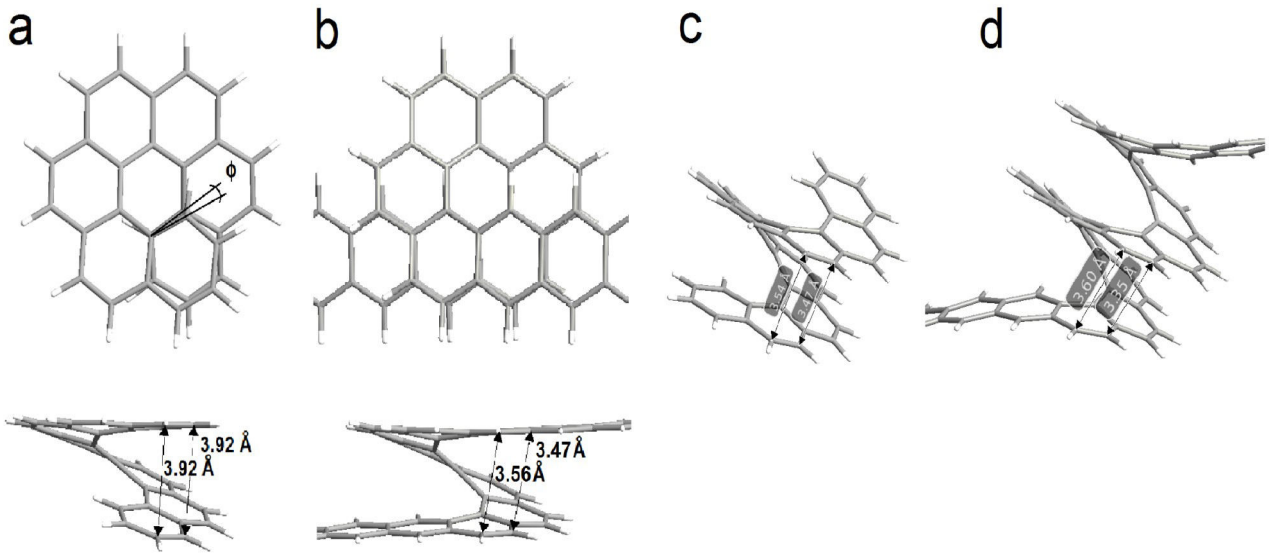

Figure 64. Comparison of twist angle ϕ and distances *IP*1 and *IP*2 used to calculate interpitch (IP_{AV}) for **a)** [7]helicene molecule and **b)** [7]helicene cut from the structure where it was merged with two 2ZGNRs. Geometry of both structures was optimized by ReaxFF CHOCsKNaClIFLi_2019. **c)** Interpitch distances for [10]helicene molecule and **d)** [10]helicene in the structure where it is merged with two 2ZGNRs. ReaxFF CHONSMgPNaCuCl_2018_08 was used for the optimization of both structures.

The problem with adapting the planar ZGNR electrodes to the non-planar helicene-based central region mentioned above gets more complicated when we assume compression and stretching. As we need at least 3 base units of ZGNRs on both sides to satisfy the used electronic transport simulation method [15], and we are using planar ribbons as boundary conditions, we need to ensure, that the maximum interatomic force component of these 3 base units is negligible after the molecular mechanics optimization. As the total number of atoms in the simulation determines its complexity, we also have to reduce it where possible. The resulting number of ZGNR base units needed for adaptation thus varies depending on the specific configuration. After the relaxed configuration is found, the number of base unit is then fixed and varies only as a method of applying strain. The electrodes geometry changes to more planar during stretching but when the helical turn is included, it tend to twist the ribbons and turn them over when stretched sufficiently.

The compression and the stretching are done by adding and removing ZGNR base units in the situation when the electrodes are fixed on the border of the electrode extensions. The stretching is more intuitive as by removing every base unit, the configuration tends to reshape to more axial. The response to compression is not so well determined as the configuration tends to form wrinkles in non-axial of-the-plane directions. To ease the references, we use the following notation: A structure with no strain is labeled as R0L0. The letters R and L denote the respective electrode (right or left) where a ZGNR base unit was added/removed. The symbol after letters R and L denotes the number of added/removed base units. If there is a number, it is removing, if there is a letter it is adding. We use "*n*H" instead of [n]helicene and we also use letters to indicate variants of fusion with GNRs. For example, a designation 4HCDE_RALA indicates that it is [4]helicene, fused in points C, D and E (which in turn means that it will be fused with 3ZGNRs), and compressed equally by adding one ZGNR base unit on both sides.

For the purpose of further analysis we need to find the optimized molecular geometry configurations. First, we have to decide which optimization method to use. Several factors affect our decision: equilibrium C-C and C-H bond lengths, interpitch distance, and twist angle. From the literature we know [115] that the experimental interpitch distance, which is defined as and average of outer helix carbon distances ($IP_{AV} = (IP1 + IP2)/2$), for [7]helicene is 450 pm. The value for [8]helicene obtained by DFT-D method is 410 pm. Comparing the DFT-D value of [7]helicene, which is 464 pm, with the experimental one, we may assume that the real interpitch distance will be smaller by a factor. The DFT-D obtained interpitch distance values moreover tend to saturate near 375 pm for higher helicenes, as also shown in [115]. The structures proposed by us should resemble similar features as longer helicenes because of the steric hinderance effects of the ribbons.

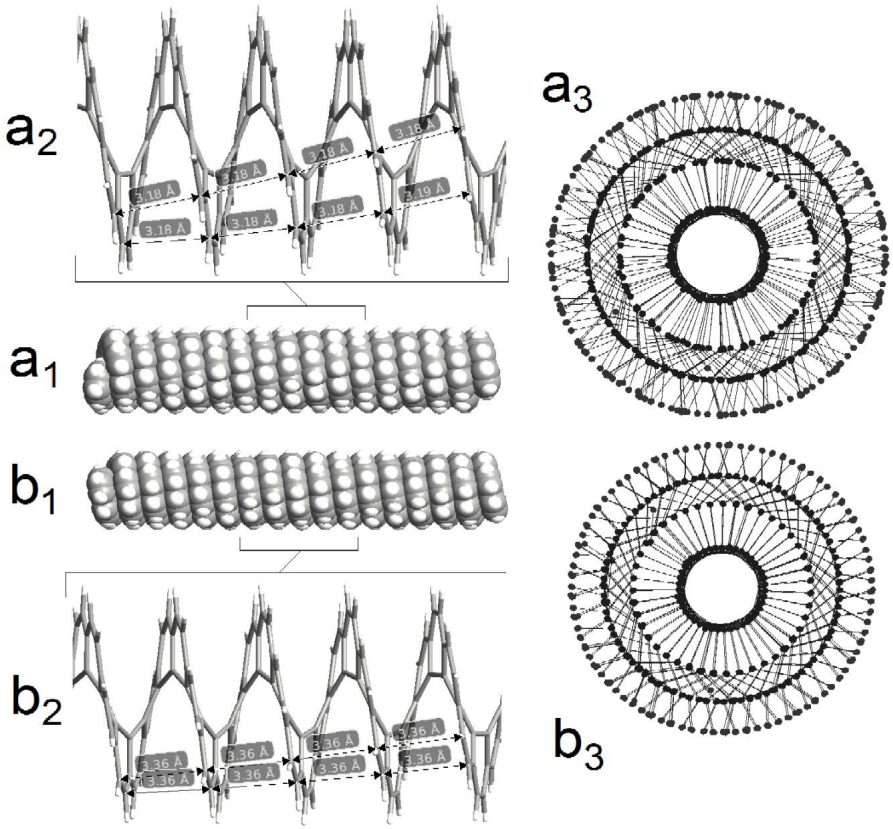

Figure 65. Comparison of [100]helicene geometries after optimization by **a)** ReaxFF_CHOCsKNaClIFLi_2019 and **b)** ReaxFF CHONSMgPNaCuCl_2018_08. The **a1**, **b1** are shown with Van der Waals force radii of all atoms. The **a2**, **b2** details show the central part on which the impact of ends of the molecule should be negligible. The **a3** and **b3** compare the symmetry in axial direction.

According to ReaxFF evolution tree [90] the ReaxFF CHOCsKNaClIFLi_2019 optimization algorithm is derived from early hydrocarbon versions and, as the name indicates, it now includes oxygene, halogenes and some elements of the first group. This draws our attention, because the potential application of helicenes is as ionophores [53]. It is also the most recent version (2019) of ReaxFF available in Synopsys Quantum ATK 2019.12. When tested with benzene molecule ReaxFF CHOCsKNaClIFLi_2019 gives C-C bond length 142 pm and C-H bond length 111 pm. In the case of [7]helicene it gave rather satisfactory result of 392 pm for the interpitch distance of a free molecule and 355 pm (IpAV) in case of the 4HAB_R0L0 structure. However, when tested with longer helicenes, the subsequent DFT calculation did not converged or converged with difficulties. We decided to use ReaxFF CHONSMgPNaCuCl_2018_08 for the longer structures, as this is also usefull optimizer because helicenes are commonly functionalized by nitrogen [23] and in contrast to ReaxFF CHOCsKNaClIFLi_2019, the ReaxFF CHONSMgPNaCuCl_2018_08 includes this element. When tested with a benzene molecule, it gives C-C bond length 143 pm and C-H bond length 107 pm. We investigated effects of bond lengths on a set of [*n*]helicenes for $n \in$ <4, 100> and found, that this more compact configuration of hydrogens leads to prolongation through increase in interpitch distance. This is more apparent in longer helicenes as seen in the **Figure 65**. It affects the calculation convergence, as much less inter-turn interactions (due to the less steric hinderance of helicene turns) is achieved. From the comparison of geometric symmetries of the resulting configurations (**Figure 65c, f**) we may see, that ReaxFF CHONSMgPNaCuCl_2018_08 leads to a better organized structure in longer

helicenes. All results of the molecules optimizations may be found in the supporting material.

Now let us compare the bond lengths and interpitch of all our structures. This is done in the **Table 2**. While studying our results and comparing them with literature [115, 116], we noticed that the interpitch distance is problematic term; at least in our case, but we also believe that this is a common phenomenon. As we know, the interpitch distance is the average of two outer carbon atom distances in helicene, e.g. as in the **Figure 64**. It is not the inter-turn (or inter-layer) distance and it is not defined for lower than [7]helicene, and above the [7]helicene there is already more than one eventuality how to choose the two pairs of outer helix carbons. Also, if we use fixed two pairs of atoms, during the stretching (as the twist angle changes) these atoms slip to new positions and the resulting interpitch (as not any longer being close to the distance of nearest inter-turn carbons) has very low informative value about the inter-turn distance. Our calculations also show that the ends of [*n*]helicene tend to have much higher inter-turn carbon distances than the middle. There is stabilizing effect of inter-layer interactions in the middle which the ends lack. We believe that the intrinsic non-zero twist angle of helicenes does not allow for carbon stacking in linear way and therefore, we do not believe the geometry used by Gou et al. in [116] to be realistic.

We believe that the twists in helicenes are among other ruled by the London dispersion force and H-H bonding, and the result is an inter-layer stacking very similar to GNR multilayers. More on molecular stacking by these mechanisms was explored in [119]. The non-zero twist angle of helicenes furthermore means that, if we omit the distortion caused by the ends of molecule which are stacking differently, there is a specific number of turns (or aromatic rings added) which will lead to repetition of the whole geometry. However, this crystal feature of helicenes becomes distinctly apparent in very long helicenes only. If ReaxFF CHONSMgPNaCuCl_2018_08 is used for the geometry optimization, we calculated that the structure repeats after at least 46 turns, which means in at least [322]helicene molecule. All this also leads to need of definition of what atoms to use for the interpitch measure, or if other means are possible. For the sake of clarity, we decided to use the distance between outer carbons in the last aromatic ring of ZGNR electrode (the same as the first ring of [7]helicene) and outer carbons in the 7th helicene ring (the same as the last ring of [7]helicene), see **Figure 64**. But this is not ideal definition as there is still a big difference between the two carbon pairs distances for short helicenes and no measure available for [n]helicenes with n ϵ <4, 6>. Therefore we added the bond lengths of several atoms in the table. This is also done to indicate which parts of helicene molecule are undergoing strain when the structure is compressed or stretched.

	*IP*1	*IP*2	Ip_{AV}	[115]Ip_{AV}	A1-A2	A1-Y1	Y2-A2	Y1-X1	X1-Y2	X1-X2	X2-F1	X2-F2	
[4]helicene	-	-	-	-	293	142	142	144	144	145	145	145	
[5]helicene	-	-	-	-	309	145	143	144	145	147	145	145	
[6]helicene	-	-	-	-	322	145	145	145	145	147	145	145	
[7]helicene	392	392	392	464	322	145	145	145	145	147	145	145	
[8]helicene	365	352	359	421	326	145	145	145	145	147	145	145	
4HAB_RALA	350	331	341	-	343	145	145	146	146	148	145	145	
4HAB_R0L0	356	347	352	-	310	145	145	145	145	147	145	145	
4HAB_R1L1	619	634	627	-	364	146	146	146	146	148	145	145	
4HAB_R2L2	752	856	804	-	502	148	148	148	148	149	145	145	
4HAB_R3L3	1053	1061	1057	-	571	150	150	152	153	149	145	145	+
4HBC_RALA	-	-	-	-	278	141	141	145	145	145	145	145	
4HBC_R0L0	-	-	-	-	282	141	141	144	144	145	145	145	
4HBC_R1L1	-	-	-	-	349	141	141	146	146	146	145	145	
4HBC_R2L2	-	-	-	-	454	143	143	152	152	145	146	146	+
4HCD_RALA	-	-	-	-	280	145	145	145	145	147	145	145	
4HCD_R0L0	-	-	-	-	279	144	144	144	144	146	144	144	
4HCD_R1L1	-	-	-	-	331	144	144	147	147	146	145	145	
4HCD_R2L2	-	-	-	-	395	144	144	152	152	145	146	146	+
4HCDE_RALA	-	-	-	-	288	145	145	144	144	146	141	141	
4HCDE_R0L0	-	-	-	-	287	145	145	144	144	147	141	141	
4HCDE_R1L1	-	-	-	-	311	144	144	144	144	145	143	143	
4HCDE_R2L2	-	-	-	-	359	145	145	148	148	147	146	146	
4HCDEFZ_R0L0	-	-	-	-	286	144	144	144	144	145	144	144	
4HCDEFZ_R1L1	-	-	-	-	304	144	144	145	145	144	144	144	
[10]helicene	354	347	351	382	326	144	144	144	144	146	143	143	*
[11]helicene	356	348	352	374	326	144	144	144	144	146	143	143	*
[12]helicene	355	349	352	375	325	144	144	144	144	146	143	143	*
[13]helicene	353	347	350	376	325	144	144	144	144	146	143	143	*
[14]helicene	355	347	351	375	326	144	144	144	144	146	143	143	*
10HAB_R0L0	369	347	358	-	329	144	145	145	144	146	143	143	*
10HAB_R1L0	411	364	388	-	378	146	144	144	145	146	143	143	*
10HAB_R1L1	475	414	445	-	422	146	145	144	145	146	143	143	*
10HAB_R2L1	589	540	565	-	457	146	145	144	145	146	143	144	*

Table 2. Comparison of inter-turn carbon distances (*IP*1 and *IP*2) our interpitch value (Ip_{AV}), interpitch value obtained from [115] and selected bond lengths. The interpitch was measured between two specific atoms and is not equal to interlayer distance (of which maximum is around 400 pm when measured in the center of 12HAB_R0L0 structure). We use the same designations of all mentioned atoms as sketched in the **Figure 63**. All values are in pm. Structures designated by * are optimized by ReaxFF CHONSMgPNaCuCl_2018_08, otherwise we used ReaxFF CHOCsKNaClIFLi_2019. Structures designated by + are the limit structures and the next iteration of stretching leads to break in covalent bonds.

The geometry optimization process was described in detail in the previous chapter. Let us add that the maximum component of interatomic forces during optimization was less than 1x10-5 eV/Å in most cases. The electronic properties calculations of the ReaxFF CHOCsKNaClIFLi_2019 optimized structures were carried out in Self-Consistent Field by using the DFT LDA exchange correlation, PZ predefined functionals, LDA.PW PseudoDojo pseudopotentials, double-zeta polarized basis set. The k-point sampling was {kx, ky, kz} = {1, 1, 128} or {1, 1, 64}, and periodic boundary conditions were along the x, y axes and Dirichlet along the z axis. To calculate electronic properties of structures optimized by ReaxFF CHONSMgPNaCuCl_2018_08 we used DFT GGA exchange correlation, PBE predefined functionals and Grimme DFT-D3 Van der Waals correction, k-point sampling {kx, ky, kz} = {1, 1, 16} while other parameters were the same as previous. For the small devices, with [4]helicene, transport calculation converged properly with geometry optimization by ReaxFF CHOCsKNaClIFLi_2019 and did not converged or

converged with difficulties with optimization by ReaxFF CHONSMgPNaCuCl_2018_08. An opposite situation was with larger [10]helicene. The used ab initio DFT method is further described in [15].

To evaluate the electronic transport properties we use formalism described in [12]. Device density of states (DDOS) for all shells, transmission spectrum (TS) and current-voltage curves were calculated for relaxed, compressed and stretched structures. The DDOS and TS of all relaxed structures are in the **Figure 66**. As we may see, the configurations with 2ZGNR and [4]helicene exhibit similar DDOS to the 30 bases long hydrogen passivated 2ZGNR of about the same length that we used as a reference. We found that the [10]helicene-based structure has one more peak in between the two expected Van Hove singularities. The structures with wider ZGNRs have naturally higher densities around the Fermi level and they do exhibit similar but sharper peak in transmission around the Fermi level as perfect ZGNR. Except for the 4HAB configuration, all the 2ZGNR-based structures have negligible transmission around the Fermi level.

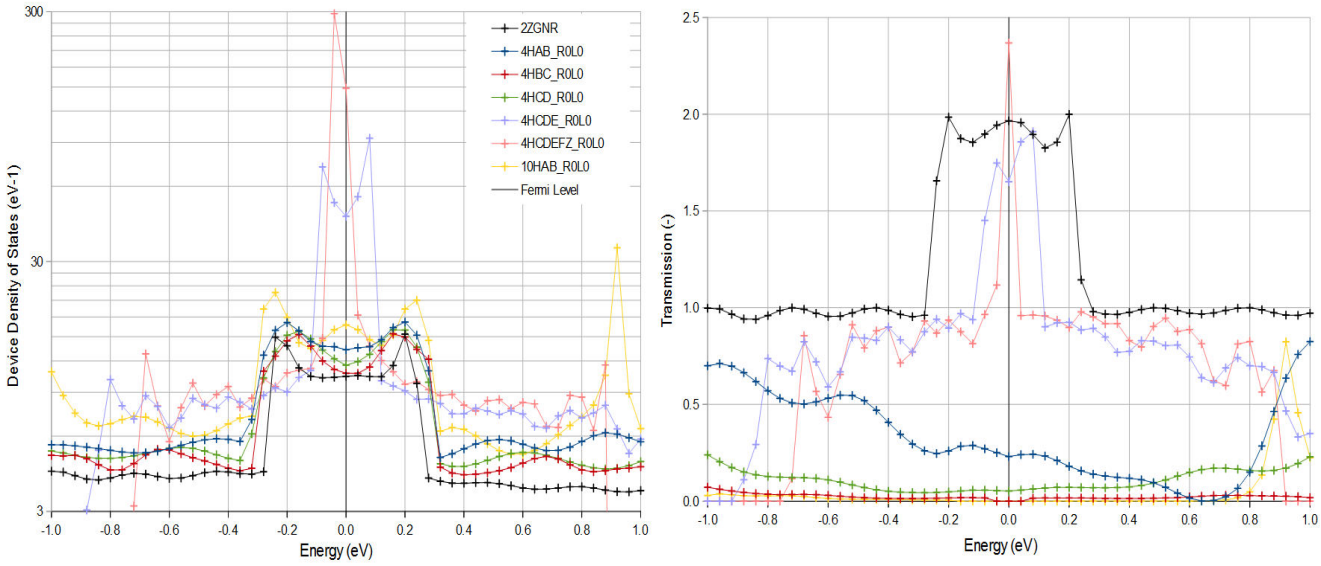

Figure 66. Device densities of states and transmission spectra of relaxed graphene-helicene-graphene structures. The results are supported with data obtained from 30-bases long 2ZGNR optimized by ReaxFF CHOCsKNaClIFLi_2019 used as a reference.

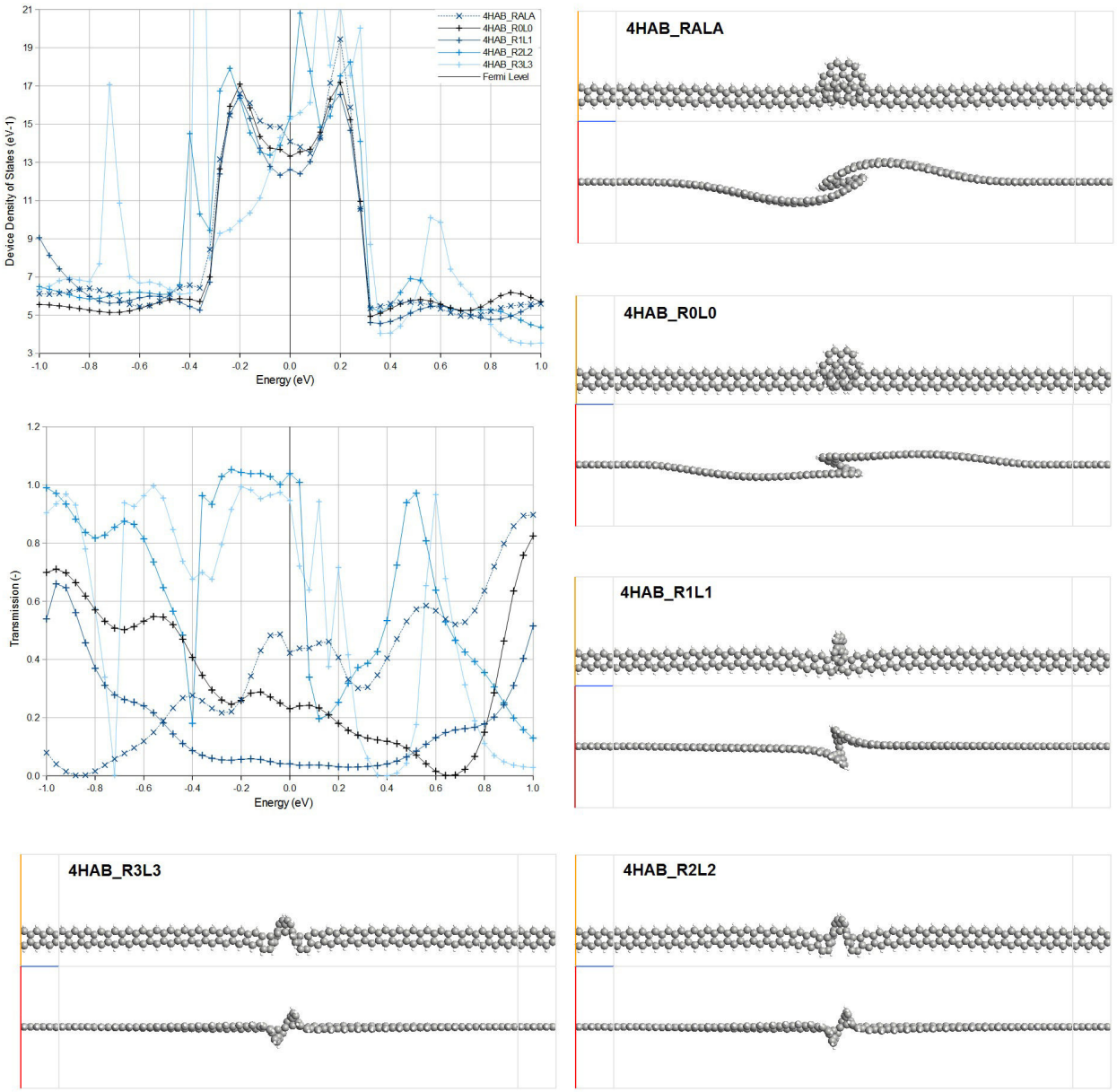

Figure 67. Device densities of states (DDOS) and transmission spectra of [4]helicene fused with two 2ZGNRs in A1B1-A2B2 configuration. The structures are shown from top and side direction where the steric hinderance region is visible. All atoms are displayed with covalent radii.

The strained structures results, along with the optimized molecular geometries, are shown in **Figures 67-72**. As we can see from the **Figure 67**, the direction of turn in the central region is changing fundamentally when the structure is strained. The electrodes geometry changes to more planar during stretching of all structures but when the helical turn is included, it tends to twist the ribbons and turn them over when stretched sufficiently. 4HAB_R3L3 (3 base units removed on both sides) is the last structure explored as the next iteration breaks the 2ZGNR. We may notice, that 4HAB_R3L3 and 4HAB_R2L2 are very similar configurations and also share similar transmission but DDOS differs substantially. In this point it is necessary to say that high interatomic forces, in highly strained structures like this, are forming more singularity points in DDOS and some of them may not be realistic. The transmission of 4HAB structures has a non-linear dependence on strain which was studied by authors of [115, 116] in different helicene-based

configurations. As in the literature, in our case, the compression leads to higher transmission and the stretching leads first to lower transmission and then it rises. We also found that for even more stretched structures it saturates and even falls, before the structure breaks. It is better apparent in the **Figure 73b** where the I/V characteristics are shown. When compared to the literature, our results show rather V-shaped curve than U-shape, because we use a different approach to strain which leads to worse resolution.

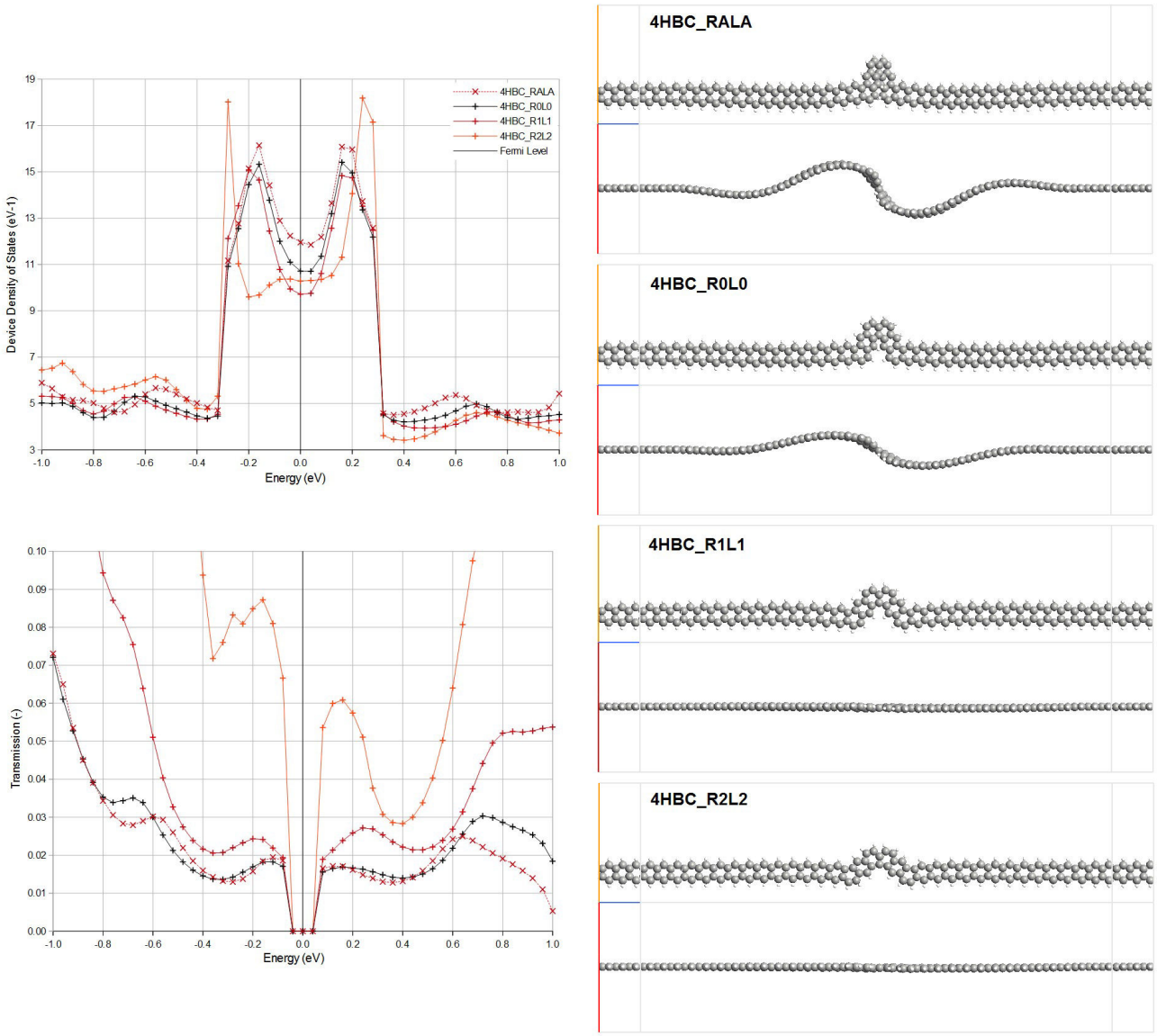

Figure 68. Device densities of states (DDOS) and transmission spectra of [4]helicene fused with two 2ZGNRs in B1C1-B2C2 configuration. The structures are shown from top and side direction where the steric hinderance region is best visible. All atoms are displayed with covalent radii.

We may see the same trend of transmission rised by stretching, but this time only a negligible impact on the transmission by compression, for 4HBC and 4HCD configurations (**Figures 68** and **69**). One interesting fact apparent from these figures is that for 4HBC there is a region of zero transmission around the Fermi level of its TS and next to it a significant rise, while 4HCD configuration behaves in the opposite way and exhibits a high peak around the Fermi level when stretched.

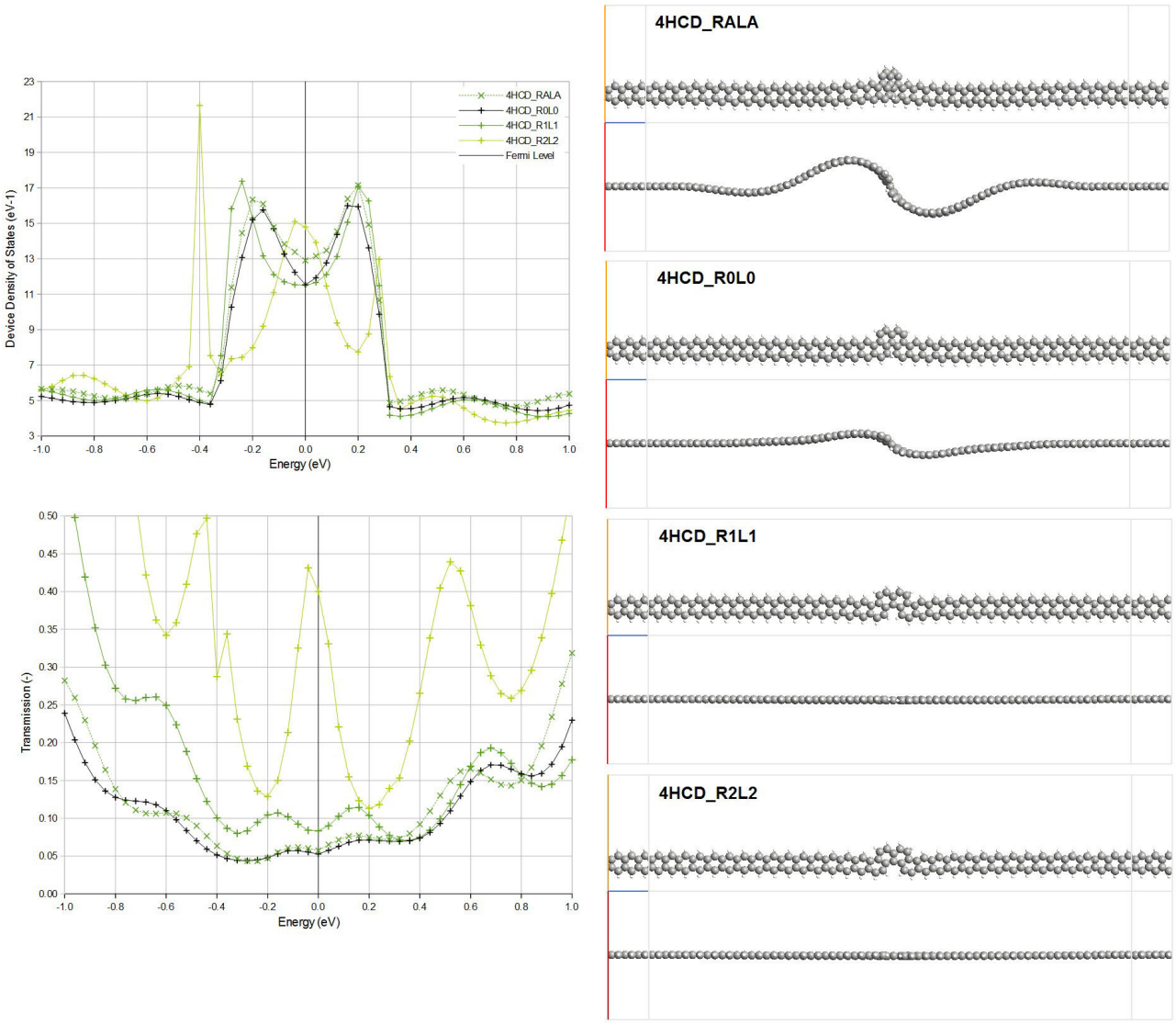

Figure 69. Device densities of states (DDOS) and transmission spectra of [4]helicene fused with two 2ZGNRs in C1D1-C2D2 configuration. The structures are shown from top and side direction where the steric hinderance region is best visible. All atoms are displayed with covalent radii.

The **Figure 70** shows one of the possible 3ZGNR-[4]helicene-3ZGNR configurations. The ribbons fuse with helicene forming notched 3ZGNR with steric hinderance in the notch. This region causes the same deformations of freestanding electrodes as in 2ZGNR-based structures. The same is observed in case of 4ZGNR structure in the **Figure 71**. Because this configuration includes high number of atoms (and thus great computing power), and so far obtained results show a similar trend as the previously studied 3ZGNR-based structure, we decided to spare computing time and end stretching after the first iteration. Although the structures undergo massive change in geometry, our results in **Figure 70** and **Figure 71** show that the impact of strain on wider ZGNRs in these configurations is negligible. The last configuration (**Figure 72**) shows electronic properties of [10]helicene-based 10HAB structure. It is a similar configuration to 4HAB, both having at least one turn in the middle and being fused with two 2ZGNRs in a similar fashion. In this case we used finer resolution when applying strain (only one 2ZGNR base unit on one side was removed at one time) and we only try

stretching. The results show that while the DDOS is comparable to other studied 2ZGNR-based structures, the transmission is zero in a wide window around the Fermi level. As we may see better from the **Figure 73a**, the conductivity of longer helicenes in this configuration is approx. three orders of magnitude smaller and we expect that even longer structures will share the less-conductive behaviour.

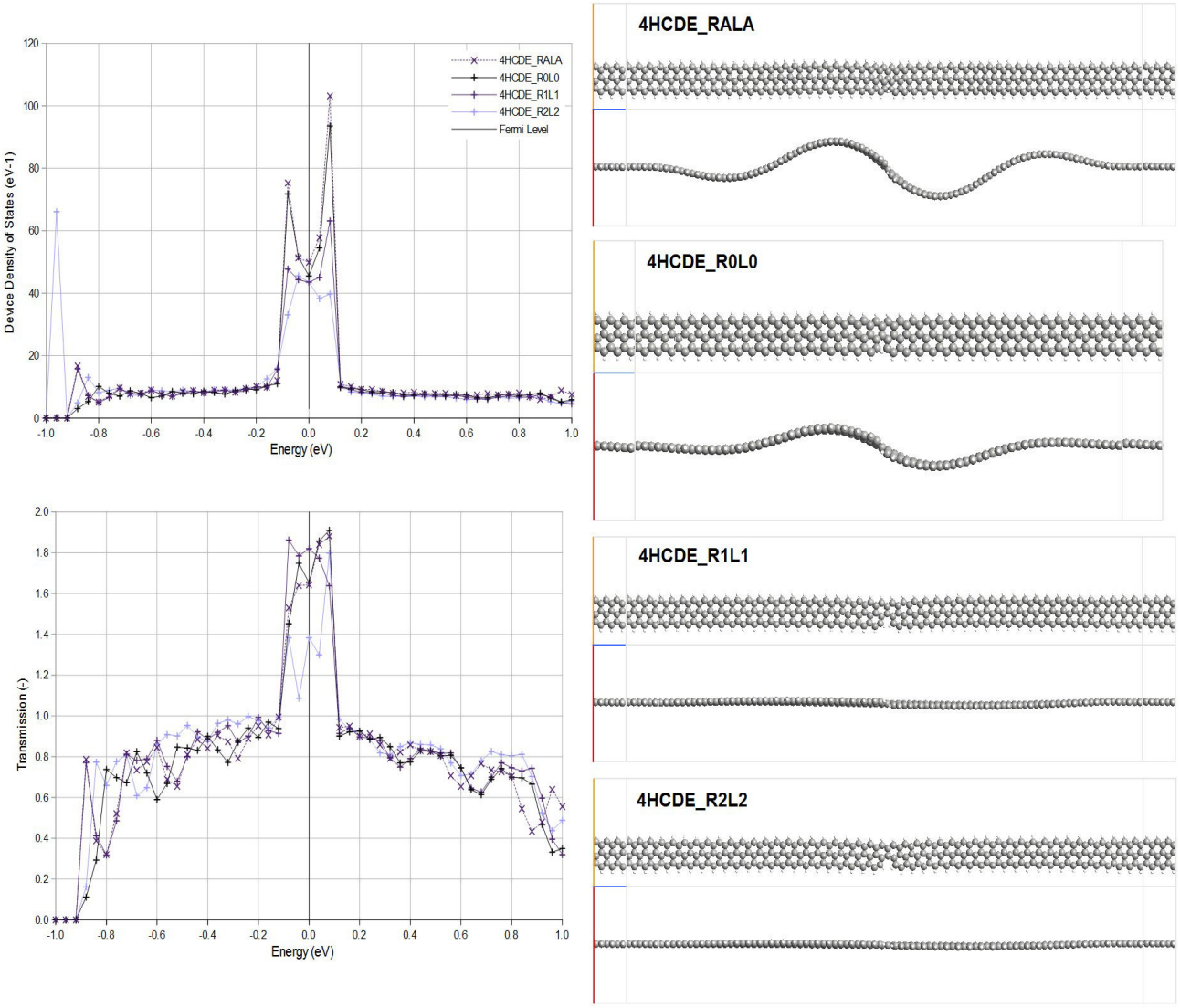

Figure 70. Device densities of states (DDOS) and transmission spectra of [4]helicene fused with two 3ZGNRs in C1D1E1-C2D2E2 configuration. The structures are shown from top and side direction where the steric hinderance region is best visible. All atoms are displayed with covalent radii.

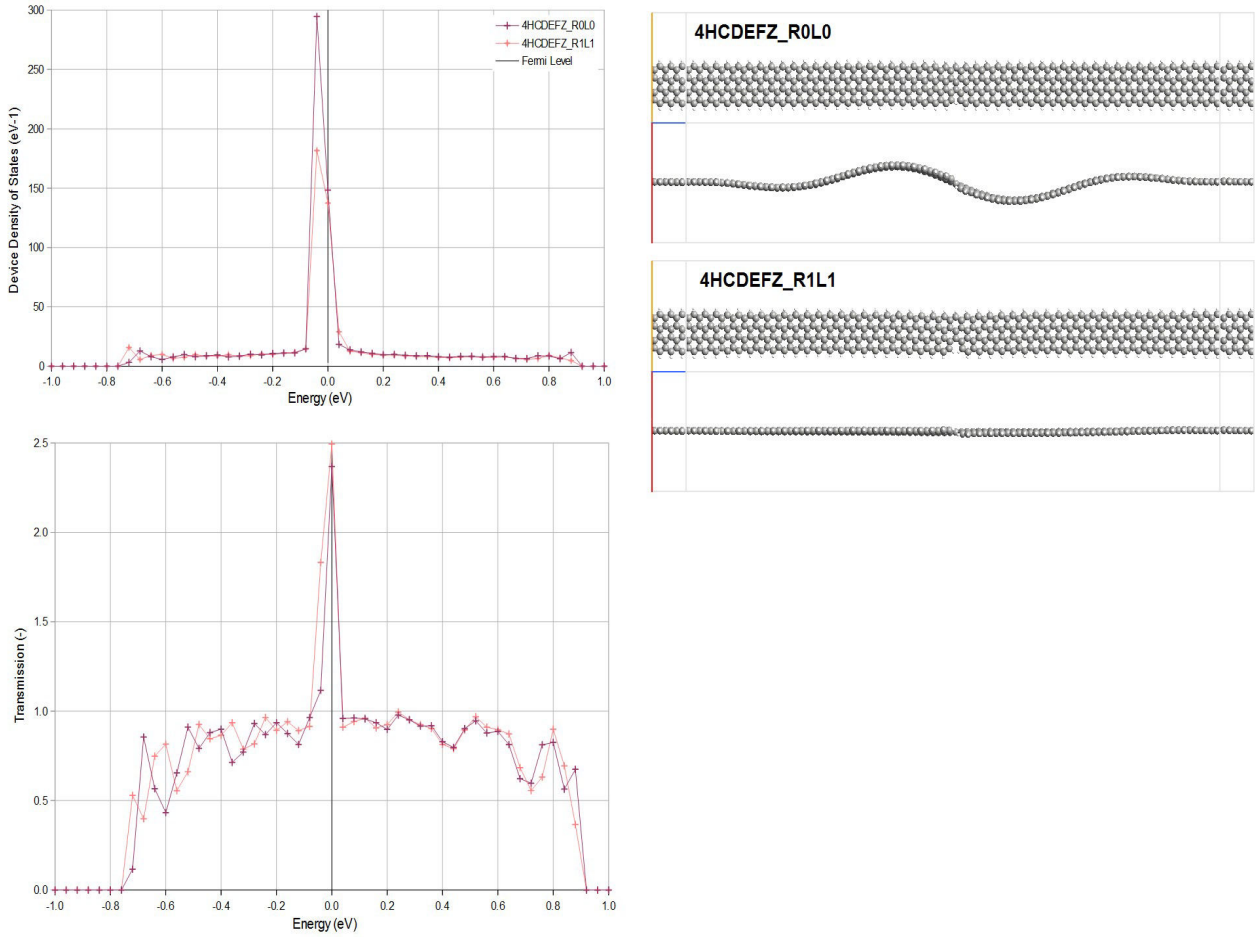

Figure 71. Device densities of states (DDOS) and transmission spectra of [4]helicene fused with two 4ZGNRs in C1D1E1F1Z-C2D2E2F2 configuration. The structures are shown from top and side direction where the steric hinderance region is best visible. All atoms are displayed with covalent radii.

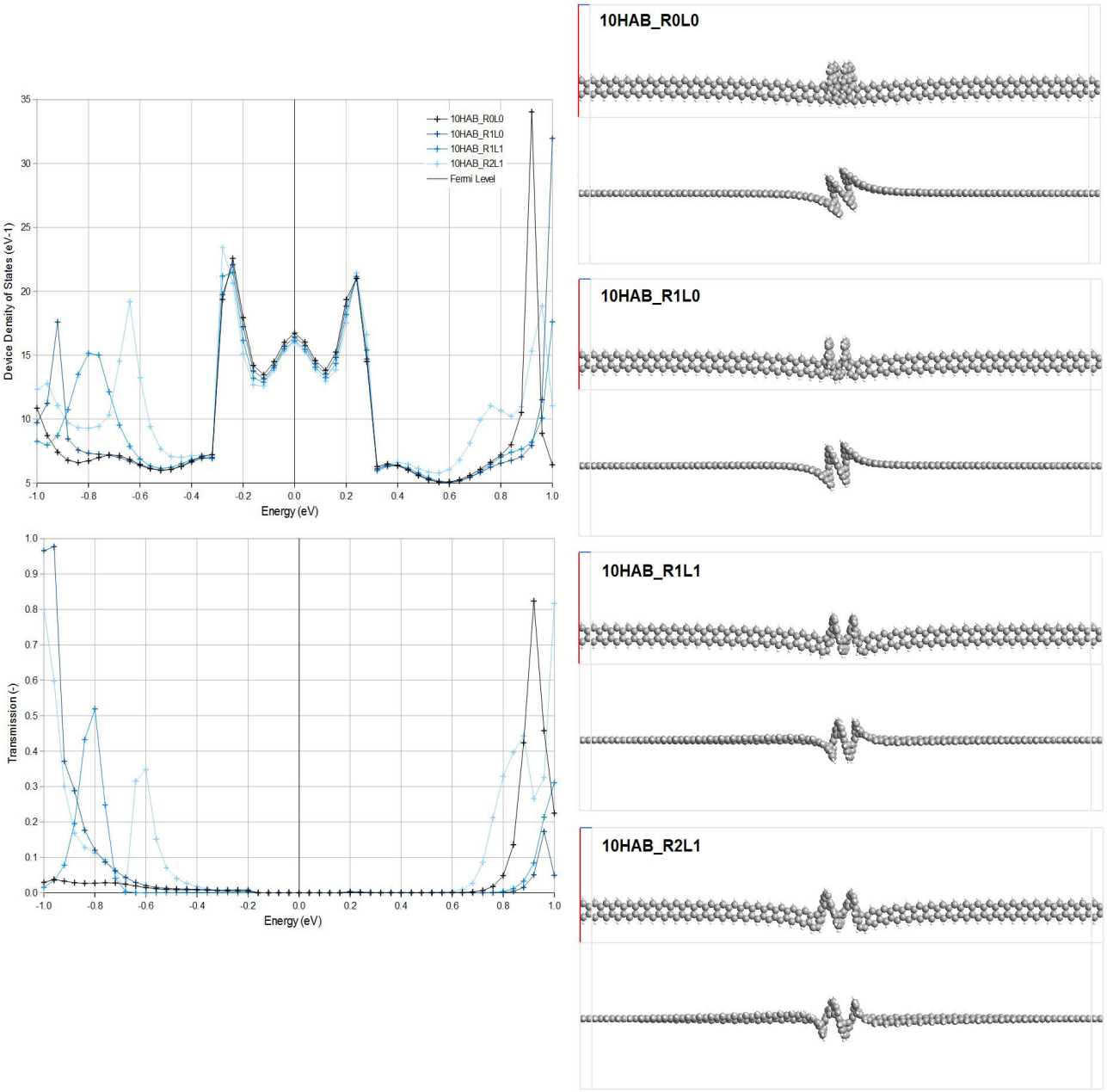

Figure 72. Device densities of states (DDOS) and transmission spectra of [10]helicene fused with two 2ZGNRs in A1B1-A2B2 configuration. The structures are shown from top and side direction where the steric hinderance regions are best visible. All atoms are displayed with covalent radii.

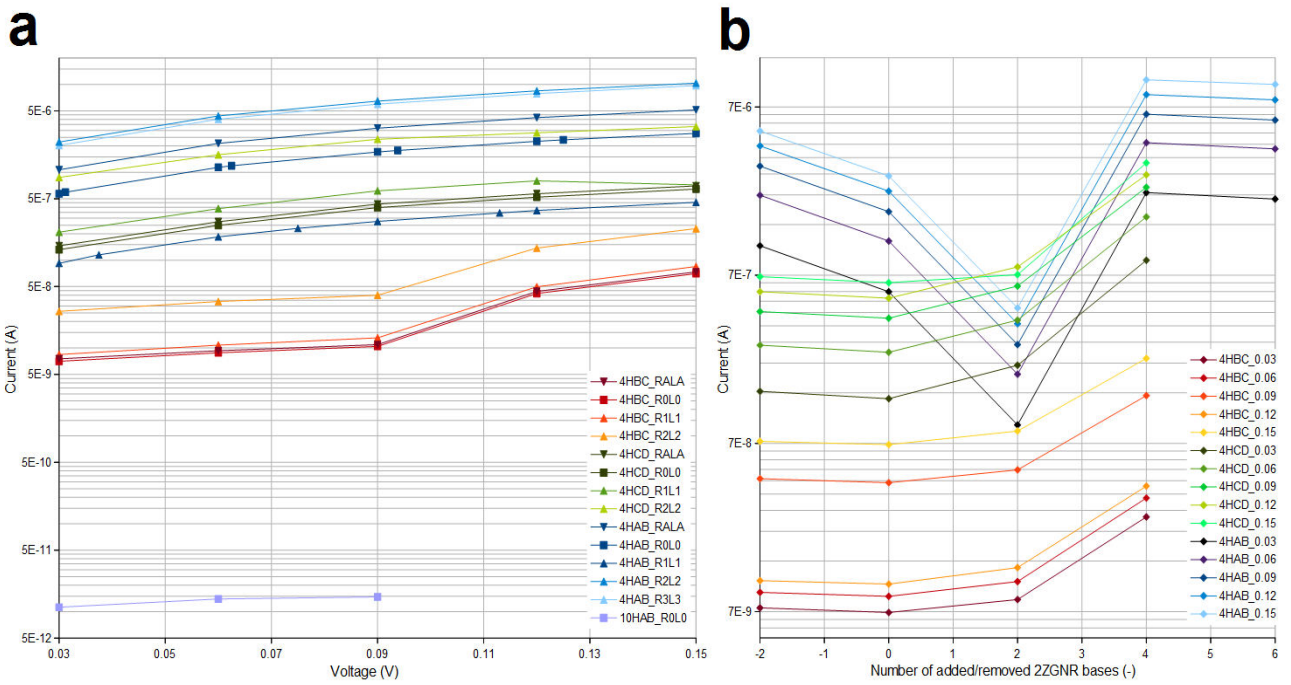

Figure 73. a) Calculated current-voltage characteristics of [4]helicene and [10]helicene fused with two 2ZGNRs for biases 30 to 150 mV. **b)** Current-to-strain relationship of [4]helicene fused with two 2ZGNRs for biases from 30 to 150 mV.

Now, let us compare our results with the available paper from Guo et al. [116]. Authors of this article are using two types of electrodes to probe current through [12]helicene and aza[12]helicene while it is being compressed and stretched. As it was discussed above, we believe that molecular geometry of real [12]helicene results in non-linear stacking of turns and different interpitch value in various parts of the molecule. As was also covered above, this leads to serious problems with the interpitch distance definition. Also, when compared to our approach, authors of [116] do not include the effects of the central region back on electrodes and the resulting nanostructure is thus in an permanent non-equilibrium conditions due to the high interatomic forces on electrode-central region border (even for the unstressed structures). It is obvious that non-equilibrium conditions may have severe effect on electronic properties (e.g. transmission spectrum, spin polarization). These are the main reasons we believe our results to be much more accurate.

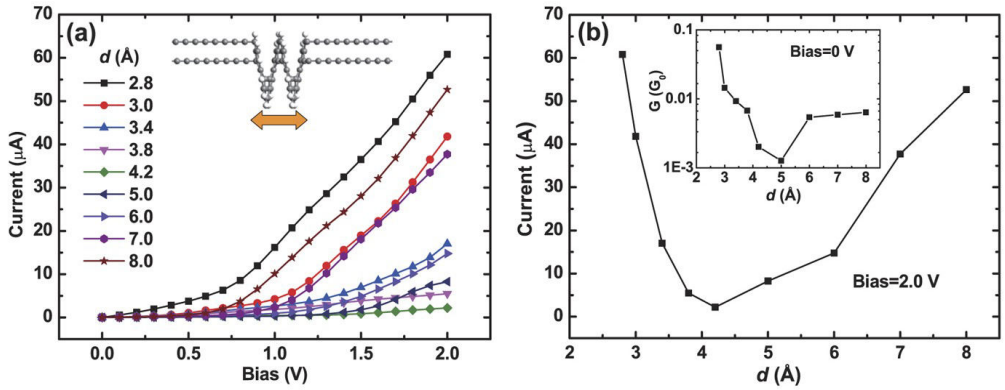

Figure 74. I − V behaviors of [12]helicene contacted with carbon chain electrodes. The pitch of the relaxed (gas-phase) [12]helicene molecule is d = 3.4 Å. **a)** I − V curve under different pitch d. **b)** Current varies with d under the bias of 2.0 V. Inset: Conductance under zero bias on a logarithmic scale. G0 is the conductance quantum (G0 = 2e2/h). The image is taken from [116].

Another conclusion which may be sketched from the comparison is that although different [*n*]helicenes were used under different conditions, the U-shape current-to-interpitch characteristics phenomenon appears in both cases. However, Guo et al. is using [12]helicene, which our molecular mechanics results say to be not suitable for colinear axial electrodes ([10]helicene instead) and we are using [4]helicene connected in a way where it may be interpretted as [*n*]helicene (*n* = 4, 5, 6, 7, 8). Despite these differences, we both obtained the same order of magnitude for current and very similar shape of the current-to-interpitch curve. On the contrary, our relaxed [10]helicene shows 5 orders of magnitude difference when compared to the [12]helicene of Guo et al.. Due to the small current response, the [10]helicene was not subjected to strain as we considered that not interesting to test. Also, we did not see as necessary to simulate behaviour under relatively high voltage bias used by Guo et al. (2V), because the real nanostructure would undergo changes by charge and thermal effects (possibly resulting in avalanche ionization) not included in the simulation methods. Our results show saturation of current for bias voltages over 150 mV for most structures and we dismissed results above that value as inconclusive due to the limitations of the used method.

Let us summarize this chapter. We present our results of graphene-helicene-graphene junction simulations. First, several possible configurations were enumerated. During our investigation, we found geometries of [*n*]helicenes for $n \in \langle 4, 100 \rangle$ optimized by two recent ReaxFF optimization algorithms (CHOCsKNaClIFLi_2019 and CHONSMgPNaCuCl_2018_08). Our results show that ends of longer helicenes have higher interpitch distance than center and in very long helicenes the center is compact. The twist angle in helicenes leads to non-linear turn stacking and we dispute linear structures in [116]. We calculated that, when neglecting the ends effects, the structure repeats after at least 46 turns, which means in at least [322]helicene molecule. The electronic transport properties of several structures under mechanical strain were investigated in device configuration. 2ZGNR-[4]helicene-2ZGNR junctions fused in three different positions show a major difference in TS. The I-V curves show difference in orders of magnitude for them and when investigating their current-to-strain relationship we found that 4HAB structure exhibits a drop in conductance when relaxed or lightly stretched and a rise of conductance when compressed or more stretched. We assume that the V-shape curve we got is consistent with predictions for similar structures made by [115, 116]. The comparison of 4HAB, 4HBC and 4HCD structures reveals that 4HBC and 4HCD do not share this property but their conductance is exponentially rising until mechanically break. We also found DDOS and TS of [4]helicene fused with 3ZGNRs and 4ZGNRs. These structures are similar to V-shape notched GNRs and according to our results exhibit only negligible impact on conductance when strained in this configuration. Finally, we found that [10]helicene has five orders of magnitude lower conductance than [4]helicene in similar device configuration. We found that when fused in the described terms, the same results as for 4HAB structure would be valid for *n*HAB, where *n* = 5, 6, 7, 8, and the results for 10HAB would be valid fo *n*HAB, where *n* = 11, 12, 13, 14. Based on our findings we assume that a combination of graphene and helicene may lead to many applications. It may allow the utilization of helicenes as connectors of nanographenes and as active sensor/actuator parts at the same time. We believe that helicenes could also be used to control connection of graphene monolayers and facilitate the magic-angle setting used in supraconductive experiments.

6 Conclusions

This work proposes some of the simulation results we obtained during our research on carbon-based nanostructures. It also contains all the necessary knowledge needed to understand basics of the state-of-the-art approach to nanostructures simulations. Using the recent literature, we described the basics of quantum-mechanical geometry optimization process as well as the quantum theory of current.

Our results of the graphene nanoribbons simulations (**Chapter 5.1**) show that they have strong spin filtering ability and that for the generation of spin-polarized currents, the formation of spin-ordered edge-localized states along the zigzag edges is the key mechanism. Since GNRs have long spin-correlation lengths and good ballistic transport characteristics they can be considered a promising active material for spintronic devices, without any need of ferromagnetic electrodes or other magnetic entities. The spin filtering structure could be prepared by the nanolithography of GNR. V-shaped notches could be realized by means of local anodic oxidation, e.g. using the scanning probe microscopy. All mentioned GNR structures may be as well prepared chemically from precursors. The structures proposed in the unpublished study may serve as a knowledge basis for compilation of nanographenes into active elements in quantum computers.

From our calculations (**Chapter 5.1.2**) we concluded that the bandstructure and the electron density of 4ZGNRs are strongly affected by the Stone-Wales defect introduced into it, however the thermodynamic stability of the structure does not severely changes. The bandstructure of resulting structure exhibits narrow bandgap for certain *k*-vectors. The homogenious distribution of electron gas changes to the lateral distribution, resulting in two parallel topological quantum wires. The lateral distribution of the electron density may be usefull for improvement in the spin filtering ability of GNRs, e.g. in the case if there are V-shaped lateral constriction (notches) introduced to the ribbon. As the SW defects may be created and removed by thermal load on the nanoribbon, we also believe, that a current-driven thermoelectrical graphene switch device could be realized by introducig SW defects to a ZGNR at one bias voltage and treating them at another (higher) bias voltage. The SW defects would then act as robust molecular-level information storage elements.

As the methods of growing epitaxially graphene by high temperature sublimation of silicon from SiC substrates were developed, we decided to theoretically study it (**Chapter 5.1.3**). The resulting structures were compared with experimental data. The transmission property was selected to evaluate the accuracy. Our calculations show that the I/V curve coefficient of step-shaped structure is approx. 0.075 S, which is almost twice less than for the flat structure. Experimental value from the literature is 26 kΩ for the graphene sample of length 1.6 μm and width 39 nm. If we take into account that our step structure model is 1000 times shorter and 20 times narrower, our value of resistance (13Ω) has the same order but is still a bit smaller than the experimental one. The reason is that the collision of electrons with phonons are not taken into account as well as the temperature of environment and other unideal conditions which we can meet in the real case. The data we obtained may be used for future investigation of graphene grown on SiC substrates.

Motivated by research of the next generation of monolayer graphene derivatives, we conducted a brief study of annulene-graphene structures (**Chapter 5.4**). Our results show that these are thermodynamically stable and can probably form larger ribbons and layers. We concluded that these structures should share some of the mechanical and

electronic properties of graphene which implies future use as molecular sieves usable e.g. in sanitation of industrial emissions, in precise molecular lab-on-chip systems, for filtration of heavy metals from water and desalinization. Annulene nets should also be compatible with graphene-based technology. They can be prepared by the means of ion (electron) beam lithography or by growth from chemical precursors.

We present our results of graphene-helicene-graphene junction simulations subsequent to our previous helicene simulations in the **Chapter 5.5**. At first, the possible polyhex configurations were systematically enumerated. During our investigation, we found geometries of [*n*]helicenes for $n \in \langle 4, 100 \rangle$ optimized by two recent ReaxFF optimization algorithms (CHOCsKNaClIFLi_2019 and CHONSMgPNaCuCl_2018_08). Our results show that ends of longer helicenes have higher interpitch distance than center and in very long helicenes the center is compact. The twist angle in helicenes leads to non-linear turn stacking and we dispute linear structures published in literature. The electronic transport properties of several structures under voltage bias and mechanical strain were investigated. 2ZGNR-[4]helicene-2ZGNR junctions fused in three different positions show a major difference in TS. The I-V curves show difference in orders of magnitude for them and when investigating their current-to-strain relationship we found that 4HAB structure exhibits a drop in conductance when relaxed or lightly stretched and a rise of conductance when compressed or more stretched. We found that the V-shape current-to-interpitch curve we got is consistent with predictions for similar structures found in available literature. The comparison of several diferent graphene-helicene fusions reveals that they do not share this property. We also calculated DDOS and TS of [4]helicene fused with 3ZGNRs and 4ZGNRs and found an identity to V-shape notched GNRs. Finally, we found that [10]helicene has five orders of magnitude lower conductance than [4]helicene when investigated in a similar device configuration. We found that when fused in the described manner, the same results as for the structure with [4]helicene will be valid for [*n*]helicenes where $n = 4, 5, 6, 7, 8$, and the results for [10]helicene will be valid for [*n*]helicenes where $n = 10, 11, 12, 13, 14$. This increases importance of our results. Based on our findings we assume that a combination of graphene and helicene may lead to many interesting applications. Due to the compatibility with graphene technology, it may allow for utilization of helicenes as connectors of nanographenes and as active sensor/actuator parts at the same time. A highly precise motion or dilation sensor could be constructed by this approach. We believe that helicenes could also be used to control fusion and position of graphene monolayers and facilitate the magic-angle setting used in multi-layer graphene supraconductive experiments.

References

[1] Balzani V., Credi A., Venturi M., (2003). Molecular Devices and Machines - A Journey into the Nano World. Weinheim: WILEY-VCH Verlag GmbH & Co. KGaA, ISBN: 3-527-30506-8.

[2] Goddard, W. A., Brenner, D. W., Lyshevski, S. E., Iafrate, G. J., (2003). Handbook of nanoscience engineering and technology. London: CRC Press LLC, ISBN: 0-8493-1200-0.

[3] Saranathan V., Seago A.E., Sandy A., Narayanan S., Mochrie S.G.J., Dufresne E.R., Cao H., Osuji Ch.O., Prum R.O., (2015). Structural Diversity of Arthropod Biophotonic Nanostructures Spans Amphiphilic Phase-Space. Nano Letters, 3735-3742, https://doi.org/10.1021/acs.nanolett.5b00201.

[4] Lee J. Y., Hong B. H., Kim W. Y., Min S. K., Kim Y., Jouravlev M. V., Bose R., Kim K. S., Hwang I., Kaufman L. J., Wong Ch. W., Kim P., Kim K. S., (2009). Near-field focusing and magnification through self-assembled nanoscale spherical lenses. Nature 460, 498-501, https://doi.org/10.1038/nature08173.

[5] Kim J., Lee J., Hamada S., Murata S., Park S. H., (2015). Self-replication of DNA rings. Nature Nanotechnology 528-533, https://doi.org/10.1038/nnano.2015.87.

[6] Jacobs W.M., Reinhardt A., Frenkel D., (2015). Rational design of self-assembly pathways for complexmulticomponent structures. Proc Natl Acad Sci U S A. 2015 May 19;112(20):6313-8, https://doi.org/10.1073/pnas.1502210112.

[7] Venter J.C., Gibson D.G., Smith H.O., Hutchinson III, C.A., (2017). Synthetic Biology: Tools for Engineering Biological Systems. , ISBN: 978-1-621821-18-2.

[8] Choi J., Kim H.J., Wang M.C., Leem J., King W.P., Nam S.W., (2015). Three-Dimensional Integration ofGraphene via Swelling, Shrinking, and Adaptation. Nano Lett. 2015 Jul 8;15(7):4525-31, https://doi.org/10.1021/acs.nanolett.5b01036.

[9] Sun Y., Li L., Wen D., Bai X., Li G., (2015). Bistable electrical switching and nonvolatile memory effect in carbonnanotube-poly(3,4-ethylenedioxythiophene):poly(styrenesulfonate) composite films. Physical ChemistryChemical Physics, https://doi.org/10.1039/C5CP02164B.

[10] Bouř P., (2000). Základy kvantových výpočtů vlastností molekul - Poznámky k přednášce. , lecture notes, available at https://doczz.cz/doc/322530/1-základy-kvantových-výpočtů-vlastností-molekul-poznámky-k.

[11] Strachan A.H., (2011). Introduction to molecular dynamics (tutorial). School of Material Engineering, PurdueUniversity, West Lafayette, lecture notes, available at https://nanohub.org.

[12] Datta S., (2005). Quantum transport. Cambridge University Press, https://doi.org/10.1017/CBO9781139164313.

[13] Leclerc B., (2008). Fock space represenations of Uq(ŝln). Ecole d'été de Grenoble, lecture notes, available at https://leclercb.users.lmno.cnrs.fr/lectnotes_final.pdf.

[14] QuantumATK - Atomistic Simulation Software., (2021). , software manual, awailable at https://www.synopsys.com/silicon/quantumatk.html.

[15] Brandbyge M., Mozos J.-L., Ordejón P., Taylor J., Stokbro K., (2002). Density-functional method for nonequilibrium electron transport. Phys. Rev. B 65, 165401, https://doi.org/10.1103/PhysRevB.65.165401.

[16] Soler J.M., Artacho E., Gale J.D., et al., (2002). The SIESTA method for ab initio order-N materials simulation. J. Phys.: Condens. Matter 14 2745, https://doi.org/10.1088/0953-8984/14/11/302.

[17] Stokbro K., Petersen D.E., Smidstrup S., (2010). Semiempirical model for nanoscale device simulations. Phys. Rev. B 82, 075420, https://doi.org/10.1103/PhysRevB.82.075420.

[18] Geim A.K., Novoselov K.S., (2007). The rise of graphene. Nat Mater. 2007 Mar;6(3):169, https://doi.org/10.1038/nmat1849.

[19] Raza H., (2012). Graphene Nanoelectronics, Metrology, Synthesis, Properties and Applications. Springer-Verlag Berlin Heidelberg, https://doi.org/10.1007/978-3-642-22984-8.

[20] Yu F., Kurmoo M., Zhuang G.L., Zuo J.L., (2018). Hierarchical tandem assembly of planar [3x3] building units into {3x[3x3]} oligomers: mixed-valency, electrical conductivity and magnetism. Chem. Sci., 2018,9, 7498-7504, https://doi.org/10.1039/c8sc02851f.

[21] Talyzin A.V., Anoshkin I.V., Krasheninnikov A.V., Nieminen R.M., Nasibulin A.G., Jiang H., Kauppinen E.I. , (2011). Synthesis of Graphene Nanoribbons Encapsulated in Single-Walled Carbon Nanotubes. Nano Lett. 2011, 11, 10, 4352–4356, https://doi.org/10.1021/nl2024678.

[22] Liu Z., Du H., Li J., Lu L., Li Z.-Y., Fang N.X., (2018). Nano-kirigami with giant optical chirality. Sci. Adv. 2018, 4, 7, eaat4436, https://doi.org/10.1126/sciadv.aat4436.

[23] Cortés B.D.B., Schmidt N., Enache M., Stöhr M., (2018). Role of Cyano Groups in the Self-Assembly of Organic Molecules on Metal Surfaces. J. Phys. Chem. C 2019, 123, https://doi.org/10.1016/B978-0-12-409547-2.13540-1.

[24] Cai J., Ruffieux P., Jaafar R., Bieri M., Braun T., Blankenburg S., Muoth M., Seitsonen A.P., Saleh M., Feng X., Müllen K., Fasel R., (2010). Atomically precise bottom-up fabrication of graphene nanoribbons. Nature 466, 470–473, https://doi.org/10.1038/nature09211.

[25] Li M., Mangalore D.K., Zhao J., Carpenter J.H.,Yan H., Ade H., Yan H., Müllen K., Blom P.W.M., Pisula W., de Leeuw D.M., Asadi K., (2018). Integrated circuits based on conjugated polymer monolayer. Nat Commun. 2018 Jan 31;9(1):451, https://doi.org/10.1038/s41467-017-02805-5.

[26] Mikhailov S., (2011). Physics and applications of graphene - experiments. Croatia: InTech, ISBN: 978-953-307-217-3.

[27] Anthony J.E., (2007). The Larger Acenes: Versatile Organic Semiconductors. Angew. Chem. 47, 3, Jan 4, 2008, 452-483, https://doi.org/10.1002/anie.200604045.

[28] Sirringhaus H., (2005). Device Physics of Solution-Processed Organic Field-Effect Transistors. Adv. Mater. 17, 20, Oct 2005, 2411-2425, https://doi.org/10.1002/adma.200501152.

[29] Gamota D., Brazis P., Kalyanasundaram K., Zhang J., (2004). Printed Organic and Molecular Electronics. Springer, Boston, MA, https://doi.org/10.1007/978-1-4419-9074-7.

[30] Facchetti A., (2007). Semiconductors for organic transistors. Mater. Today 10, 3, Mar 2007, 28-37, https://doi.org/10.1016/S1369-7021(07)70017-2.

[31] Zuzak R., Dorel R., Krawiec M., Such B., Kolmer M., Szymonski M., Antonio M. Orcid E., Godlewski S., (2017). Nonacene Generated by On-Surface Dehydrogenation. ACS Nano 2017, 11, 9, 9321–9329, https://doi.org/10.1021/acsnano.7b04728.

[32] Krüger J., García F., Eisenhut F., Skidin D., Alonso J.M., Guitián E., Pérez D., Cuniberti G., Moresco F., Peña D., (2017). Decacene: On-Surface Generation. Angew. Chem. 56, 39, Sep 18, 2017, 11945-11948, https://doi.org/10.1002/anie.201706156.

[33] Zade S.S., Bendikov M., (2010). Heptacene and Beyond: The Longest Characterized Acenes. Angew. Chem. 49, 24, Jun 1, 2010, 4012-4015, https://doi.org/10.1002/anie.200906002.

[34] Wu Ch.-S., Chai J.-D., (2015). Electronic Properties of Zigzag Graphene Nanoribbons Studied by TAO-DFT. J. Chem. Theory Comput. 2015, 11, 5, 2003–2011, https://doi.org/10.1021/ct500999m.

[35] Ding Z., Jiang J., Xing H., Shu H., Dong R., Chen X., Lu W., (2011). Transport properties of graphene nanoribbon-based molecular devices. J Comput Chem. 2011 Mar;32(4):737-41, https://doi.org/10.1002/jcc.21676.

[36] Souma S., Ogawa M., Yamamoto T., Watanabe K., (2008). Numerical simulation of electronic transport in zigzag-edged graphene nano-ribbon devices. J. Comput. Electron. 7, 390–393, https://doi.org/10.1007/s10825-008-0237-z.

[37] Li J., Li Z., Zhou G., Liu Z., Wu J., Gu B.-L., Ihm J., Duan W., (2010). Spontaneous edge-defect formation and

defect-induced conductance suppression in graphene nanoribbons. Phys. Rev. B 82, 115410, https://doi.org/10.1103/PhysRevB.82.115410.

[38] Hod O., Peralta J.E., Scuseria G.E., (2007). Edge effects in finite elongated graphene nanoribbons. Phys. Rev. B 76, 233401, https://doi.org/10.1103/PhysRevB.76.233401.

[39] Rosales L., Orellana P., Barticevic Z., Pacheco M., (2008). Transport properties of graphene nanoribbon heterostructures. Microelectronics Journal 39, 3–4, Mar–Apr 2008, Pages 537-540, https://doi.org/10.1016/j.mejo.2007.07.080.

[40] Fiori G., Lebègue S., Betti A., Michetti P., Klintenberg M., Eriksson O., Iannaccone G. , (2010). Simulation of hydrogenated graphene field-effect transistors through a multiscale approach. Phys. Rev. B 82, 153404, https://doi.org/10.1103/PhysRevB.82.153404.

[41] Yan Q., Huang B., Yu J., Zheng F., Zang J., Wu J., Gu B.-L., Liu F., Duan W., (2009). Intrinsic Current−Voltage Characteristics of Graphene Nanoribbon Transistors and Effect of Edge Doping. Nano Lett. 2007, 7, 6, 1469–1473, https://doi.org/10.1021/nl070133j.

[42] Tombros N., Jozsa C., Popinciuc M., Jonkman H.T., van Wees B.J., (2007). Electronic spin transport and spin precession in single graphene layers at room temperature. Nature 448, 571–574, https://doi.org/10.1038/nature06037.

[43] Leutenantsmeyer J.Ch., Ingla-Aynés J., Fabian J., van Wees B.J., (2018). Observation of Spin-Valley-Coupling-Induced Large Spin-Lifetime Anisotropy in Bilayer Graphene. Phys. Rev. Lett. 121, 127702, https://doi.org/10.1103/PhysRevLett.121.127702.

[44] Zhang Y.-T., Jiang H., Q. Sun, Xie X.C., (2010). Spin polarization and giant magnetoresistance effect induced by magnetization in zigzag graphene nanoribbons. Phys. Rev. B 81, 165404, https://doi.org/10.1103/PhysRevB.81.165404.

[45] Cho S., Chen Y.-F., Fuhrer M.S., (2007). Gate-tunable Graphene Spin Valve. Appl. Phys. Lett. 91, 123105, https://doi.org/10.1063/1.2784934.

[46] Wimmer M., Adagideli I., Berber S., Tománek D., Richter K., (2008). Spin Currents in Rough Graphene Nanoribbons: Universal Fluctuations and Spin Injection. Phys. Rev. Lett. 100, 177207, https://doi.org/10.1103/PhysRevLett.100.177207.

[47] Mishra S., Beyer D., Eimre K., Ortiz R., Fernández-Rossier J., Berger R., Gröning O., Pignedoli C.A., Fasel R., Feng X., Ruffieux P., (2020). Collective All-Carbon Magnetism in Triangulene Dimers. Angew. Chem. 59, 29, 12041-12047, https://doi.org/10.1002/anie.202002687.

[48] Wang W.L., Meng S., Kaxiras E., (2008). Graphene NanoFlakes with Large Spin. Nano Lett. 2008, 8, 1, 241–245,

https://doi.org/10.1021/nl072548a.

[49] Park J.M., Cao Y., Watanabe K., Taniguchi T., Jarillo-Herrero P., (2021). Tunable strongly coupled superconductivity in magic-angle twisted trilayer graphene. Nature 590, 249–255, https://doi.org/10.1038/s41586-021-03192-0.

[50] Johansson K.O., Head-Gordon M.P., Schrader P.E., Wilson K.R., Michelsen H.A., (2018). Resonance-stabilized hydrocarbon-radical chain reactions may explain soot inception and growth. Science 361, 6406, 997-1000, https://doi.org/10.1126/science.aat3417.

[51] Bruno A., Commodo M., HaqueS.A., Minutolo P., (2015). Spectroscopic investigation of flame synthesized carbon nanoparticle/P3HT blends. Carbon 94, 955-961, https://doi.org/10.1016/j.carbon.2015.07.085.

[52] Lee, S.-M., Kim, J.-H., Ahn, J.-H., (2015). Graphene as a flexible electronic material: mechanical limitations by defect formation and efforts to overcome. Mater. Today 6, 336-344, https://doi.org/10.1016/j.mattod.2015.01.017.

[53] Zhou S.Y., Gweon G.-H., Fedorov A.V., First P.N., de Heer W.A. et al., (2007). Substrate-induced bandgap opening in epitaxial graphene. Nat. Mater., vol. 6, no. 10, pp. 770-5, https://doi.org/10.1038/nmat2003.

[54] Yu X.Z., Hwang C.G., Jozwiak C.M., Köhl A., Schmid A.K., Lanzara A., (2011). New Synthesis Method for the Growth of Epitaxial Graphene. Journal of Electron Spectroscopy and Related Phenomena, vol. 184, pp.100-106, https://doi.org/10.1016/j.elspec.2010.12.034.

[55] Hass J., de Heer W. A., Conrad E. H., (2008). The growth and morphology of epitaxial multilayer graphene. J. Phys. Condens. Matter, vol. 20, no. 32, p. 323202, https://doi.org/10.1088/0953-8984/20/32/323202.

[56] Lalmi B., Girard J. C., Pallecchi E., Silly M., (2014). Flower-Shaped Domains and Wrinkles in Trilayer Epitaxial Graphene on Silicon Carbide. Sci. Rep., vol. 4, pp. 225-229, https://doi.org/10.1038/srep04066.

[57] Hu Z., Ruan M., Guo Z., Dong R., et al., (2012). Structured epitaxial graphene: growth and properties. J. Phys. D. Appl. Phys. , vol. 45, p. 154010, https://doi.org/10.1088/0022-3727/45/15/154010.

[58] Baringhaus J., Ruan M., Edler F., et al., (2014). Exceptional ballistic transport in epitaxial graphene nanoribbons. Nature, vol. 506, no. 7488, pp. 349-354, https://doi.org/10.1038/nature12952.

[59] O'Connell M. J., (2006). Carbon Nanotubes Properties and Applications. London: Taylor & Francis Group, ISBN:978-0-8493-2748-3.

[60] Talyzin A.V., Anoshkin I.V., Krasheninnikov A.V., Nieminen R.M., Nasibulin A.G., Jiang H., Kauppinen E.I., (2011). Synthesis of Graphene Nanoribbons Encapsulated in Single-Walled Carbon Nanotubes. Nano Letters,

https://doi.org/10.1021/nl2024678.

[61] Ösawa E., (2002). Perspectives of Fullerene Nanotechnology. Dordrecht: Kluwer Academic Publishers, ISBN: 978-94-010-9600-3.

[62] Simon F., Monthioux M., (2015). Fullerenes inside Carbon Nanotubes: The Peapods, chapter from e-book, available at http://homepage.univie.ac.at/ferenc.simon/publications/2011/MonthiouxBookChapter.pdf.

[63] Spitler E. L., Johnson II Ch. A., Haley M.M., (2006). Renaissance of Annulene Chemistry. Chem. Rev. 2006, 106, 12, 5344–5386, https://doi.org/10.1021/cr050541c.

[64] Shen Y., Chen Ch.-F., (2012). Helicenes: Synthesis and Applications. Chem. Rev. 2012, 112, 3, 1463–1535, https://doi.org/10.1021/cr200087r.

[65] Chen Ch.-F., Shen Y., (2017). Helicene Chemistry: From Synthesis to Applications. Springer, Berlin, Heidelberg, https://doi.org/10.1007/978-3-662-53168-6.

[66] Yashima E., Maeda K., Iida H., Furusho Y., Nagai K., (2009). Helical Polymers: Synthesis, Structures, and Functions. Chem. Rev. 109, 11, 6102–6211, https://doi.org/10.1021/cr900162q.

[67] Gingras M., (2013). One hundred years of helicene chemistry. Part 3: applications and properties of carbohelicenes. Chem Soc Rev. 42(3):1051-95, https://doi.org/10.1039/c2cs35134j.

[68] Chocholoušová J.V., Vacek J., Andronova A., Míšek J., Songis O., Šámal M., Stará I.G., Meyer M., Bourdillon M., Pospíšil L., Starý I., (2014). On the physicochemical properties of pyridohelicenes. Chemistry 20(3):877-93, https://doi.org/10.1002/chem.201204410.

[69] Hasan M., Borovkov V., (2017). Helicene-Based Chiral Auxiliaries and Chirogenesis. Symmetry 10, 10, https://doi.org/10.3390/sym10010010.

[70] Rybáček J., Huerta-Angeles G., Kollárovič A., Stará I.G., Starý I., Rahe P., Nimmrich M., Kühnle A., (2010). Racemic and Optically Pure Heptahelicene-2-carboxylic Acid: Its Synthesis and Self-Assembly into Nanowire-Like Aggregates. Eur. J. Org. Chem. 2011, 5, Feb 2011, 853-860, https://doi.org/10.1002/ejoc.201001110.

[71] Naulet G., Sturm L., Robert A., Dechambenoit P., Röhricht F., Herges R., Bocka H., Durola F., (2018). Cyclic Tris-[5]Helicenes with Single and Triple Twisted Möbius Topologies and Möbius Aromaticity. Chem. Sci., 2018,9, 8930-8936, https://doi.org/10.1039/C8SC02877J.

[72] Hosokawa T., Takahashi Y., Matsushima T., Watanabe S., Kikkawa S., Azumaya I., Tsurusaki A., Kamikawa K., (2017). Synthesis, Structures, and Properties of Hexapole Helicenes: Assembling Six [5]Helicene Substructures into

Highly Twisted Aromatic Systems. J. Am. Chem. Soc. 2017, 139, 51, 18512–18521, https://doi.org/10.1021/jacs.7b07113.

[73] Matsushima T., Shoko Kikkawa S., Azumaya I., Watanabe S., (2018). Triple Helicene Cage: Three-Dimensional π-Conjugated Chiral Cage with Six [5]Helicene Units. ChemistryOpen 7, 4, Apr 2018, 278-281, https://doi.org/10.1002/open.201800006.

[74] Fuchter M.J., Schaefer J., Judge D.K., Wardzinski B., Weimar M., Krossing I., (2012). [7]-Helicene: a chiral molecular tweezer for silver(I) salts. Dalton Trans., 2012,41, 8238-8241, https://doi.org/10.1039/C2DT30900A.

[75] Toya M., Ito H., Itami K., (2018). Recent advances in acetylene-based helical oligomers and polymers: Synthesis, structures, and properties. Tetrahedron Lett., https://doi.org/10.1016/j.tetlet.2018.03.018.

[76] Olseon J.M., Esch T.E.H., (2019). Synthesis of a [5] Helicene-Based Chiral Polymer. J. Biomed. Mater. Res. Apr 2019, 17, 3, 12908-12915, https://doi.org/10.26717/BJSTR.2019.17.003019.

[77] Fox J.M., Lin D., Itagaki Y., Fujita T., (1998). Synthesis of Conjugated Helical Acetylene-Bridged Polymers and Cyclophanes. J. Org. Chem. 1998, 63, 6, 2031–2038, https://doi.org/10.1021/jo972101u.

[78] Phillips K.E.S., Katz T.J., Jockusch S., Lovinger A.J., Turro N.J., (2001). Synthesis and properties of an aggregating heterocyclic helicene. J. Am. Chem. Soc. 2001, 123, 48, 11899–11907, https://doi.org/10.1021/ja011706b.

[79] Pieters G., Gaucher A., Marque S., Maurel F., Lesot P., Prim D., (2010). Regio-defined Amino-[5]oxa- and Thiahelicenes: a Dramatic Impact of the Nature of the Heteroatom on the Helical Shape and Racemization Barriers. J. Org. Chem. 2010, 75, 6, 2096–2098, https://doi.org/10.1021/jo1000127.

[80] Graule S., Rudolph M., Shen W., Williams J.A.G., Lescop Ch., Autschbach J., Crassous J., Réau R., (2010). Assembly of pi-Conjugated Phosphole-Azahelicene Derivatives into Chiral Coordination Complexes: a Combined Experimental and Theoretical Study. Chem. Eur. J. 16, 20, May 25, 2010, 5976-6005, https://doi.org/10.1002/chem.200903234.

[81] Tounsi M., Braiek M.B., Baraket A., Lee M., Zine N., Zabala M., Bausells J., Aloui F., Hassine B.B., Maaref A., Errachid A., (2016). Electrochemical Capacitive K+ EMIS Chemical Sensor Based on the Dibromoaza[7]helicene as an Ionophore for Potassium Ions Detection. Electroanalysis 28, 12, December 2016, 2892-2899, https://doi.org/10.1002/elan.201600104.

[82] Zhou L.-L., Li M., Lu H.-Y., Chen Ch.-F., (2016). Benzo[5]helicene-based conjugated polymers: synthesis, photophysical properties, and application for the detection of nitroaromatic explosives. Polym. Chem., 2016,7, 310-318, https://doi.org/10.1039/C5PY01794G.

[83] Li M., Lu H.-Y., Liu R.-L., Chen J.-D., Chen Ch.-F., (2012). Turn-on fluorescent sensor for selective detection of Zn(2+), Cd(2+), and Hg(2+) in water. J. Org. Chem. 2012, 77, 7, 3670–3673, https://doi.org/10.1021/jo3002744.

[84] Wigglesworth T.J., Sud D., Norsten T.B., Lekhi V.S., Branda N.R., (2005). Chiral discrimination in photochromic helicenes. J. Am. Chem. Soc. 2005, 127, 20, 7272–7273, https://doi.org/10.1021/ja050190j.

[85] Moussa M.E.S., Srebro M., Anger E., Vanthuyne N., Roussel Ch., Lescop Ch., Autschbach J., Crassous J., (2013). Chiroptical Properties of Carbo[6]Helicene Derivatives Bearing Extended p-Conjugated Cyano Substituents. Chirality 25, 8, Aug 2013, 455-465, https://doi.org/10.1002/chir.22201.

[86] Nuckolls C., Katz T.J., Verbiest T., Elshocht S.V., Kuball H.-G., Kiesewalter S., Lovinger A.J., Persoons A., (1998). Circular Dichroism and UV-Visible Absorption Spectra of the Langmuir-Blodgett Films of an Aggregating Helicene. J. Am. Chem. Soc. 1998, 120, 34, 8656–8660, https://doi.org/10.1021/ja981757h.

[87] Verbiest T., Elshocht S.E., Persoons A., Nuckolls C., Phillips K.E., Katz T.J., (2003). Second-order nonlinear optical properties of highly symmetric chiral thin films. Langmuir 2001, 17, 16, 4685–4687, https://doi.org/10.1016/j.mser.2003.09.002.

[88] Gong L.-J., Liu Ch.-Y., Ma Ch., Lin W.-F., Lva J.-K., Zhang X.-Y., (2019). Theoretical study on the electronic structure and second-order nonlinear optical properties of benzannulated or selenophene-annulated expanded helicenes. RSC Adv., 2019,9, 17382-17390, https://doi.org/10.1039/C9RA01136F.

[89] Jakubec M., Ghosh I., Storch J., König B., (2020). Photochemical Functionalization of Helicenes. Chem. Eur. J. 26, 2, Jan 7, 2020, 543-547, https://doi.org/10.1002/chem.201904169.

[90] Kubo H., Hirose T., Matsuda K., (2017). Control over the Emission Properties of [5]Helicenes Based on the Symmetry and Energy Levels of Their Molecular Orbitals. Org. Lett. 2017, 19, 7, 1776–1779, https://doi.org/10.1021/acs.orglett.7b00548.

[91] Hu Y., Wex B., Perkovic M.W., Neckers D.C., (2008). Tunable blue-emitting fluorophores—benzo[1,2-b:4,3-b′]dithiophene and trithia[5]helicene end-capped with electron-rich or electron-deficient aryl substituents. Tetrahedron 64, 9, 25 Feb 2008, 2251-2258, https://doi.org/10.1016/j.tet.2007.12.029.

[92] Sahasithiwat S., Mophuang T., Menbangpung L., Kamtonwong S., Sooksimuang T., (2010). 3,12-Dimethoxy-7,8-dicyano-[5]helicene as a novel emissive material for organic light-emitting diode. Synth. Met. 160, 11–12, Jun 2010, 1148-1152, https://doi.org/10.1016/j.synthmet.2010.02.039.

[93] Shi L., Liu Z., Dong G., Duan L., Qiu Y., Jia J., Guo W., Zhao D., Cui D., Tao X., (2012). Synthesis, Structure, Properties, and Application of Carbazole-Based Diaza[7]helicene in a Deep-Blue-Emitting OLED. Chem. Eur. J. 18, 26, Jun 25, 2012, 8092-8099, https://doi.org/10.1002/chem.201200068.

[94] Xu N., Li Y, Ricciarelli D., Wang J., Mosconi E., Yuan Y., Angelis F.D., Zakeeruddin S.M., Grätzel M., Wang P., (2019). An Oxa[5]helicene-Based Racemic Semiconducting Glassy Film for Photothermally Stable Perovskite Solar Cells. iScience 15, 31 May 2019, 234-242, https://doi.org/10.1016/j.isci.2019.04.031.

[95] Storch J., Zadny J., Strasak T., Kubala M., Sykora J., Dusek M., Cirkva V., Matejka P., Krbal M., Vacek J., (2015). Synthesis and characterisation of a helicene-based imidazolium salt and its application in organic molecular electronics. Chem. Eur. J. 21, 6, Feb 2, 2015, 2343-2347, https://doi.org/10.1002/chem.201405239.

[96] Moon H., Zeis R., Borkent E.-J., Besnard C., Lovinger A.J., Siegrist T., Kloc Ch., Bao Z., (2004). Synthesis, Characterization and Transistor Response of Tetrathia-[7]-Helicene Precursors and Derivatives. J. Am. Chem. Soc. 2004, 126, 47, 15322–15323, https://doi.org/10.1021/ja045208p.

[97] Hrbáč J., Strašák T., Fekete L., Ladányi V., Pokorný J., Bulíř J., Krbal M., Žádný J., Storch J., Vacek J., (2017). Potential-Driven On/Off Switch Strategy for the Electrosynthesis of [7]Helicene-Derived Polymers. ChemElectroChem 4, 12, Dec 2017, 3047-3052, https://doi.org/10.1002/celc.201700441.

[98] Hrbac J., Storch J., Halouzka V., Cirkva V., Matejka P., Vacek J., (2014). Immobilization of helicene onto carbon substrates through electropolymerization of [7]helicenyl-thiophene. RSC Adv., 2014, 4, 46102-46105, https://doi.org/10.1039/C4RA06283C.

[99] Zhao L., Kaiser R.I., Bo Xu, Ablikim U., Lu W., Ahmed M., Evseev M.M., Bashkirov E.K., Azyazov V.N., Zagidullin M.V., Morozov A.N., Howlader A.H., Wnuk S.F., Mebel A.M., Joshi D., Veber G., Fischer F.R. , (2019). Gas phase synthesis of [4]-helicene. Nat Commun 10, 1510, https://doi.org/10.1038/s41467-019-09224-8.

[100] Žádný J., Jančařík A., Andronova A., Šámal M., Chocholoušová J.V., Vacek J., Pohl R., Šaman D., Císařová I., Stará I.G., Starý I., (2012). A General Approach to Optically Pure [5]-, [6]-, and [7]Heterohelicenes. Angew. Chem. 51, 24, Jun 11, 2012, 5857-5861, https://doi.org/10.1002/anie.201108307.

[101] Chen S., Ge Z., Jia Q., Wang K.-P., Gan L.-H., Hu Z.-Q., (2019). The Preparation of Enantiopure [6]- and [7]Helicenes from Binaphthanol. Chem.: Asian J. 14, 9, May 2, 2019, 1462-1466, https://doi.org/10.1002/asia.201900210.

[102] Jančařík A., Rybáček J., Cocq K., Chocholoušová J.V., Vacek J., Pohl R., Bednárová L., Fiedler P., Císařová I., Stará I.G., Starý I., (2013). Rapid Access to Dibenzohelicenes and their Functionalized Derivatives. Angew. Chem. 52, 38, Sep 16, 2013, 9970-9975, https://doi.org/10.1002/anie.201301739.

[103] Upadhyay G.M., Bedekar A.V., (2015). Synthesis and photophysical properties of bi-aza[5]helicene and bi-aza[6]helicene. Tetrahedron 71, 34, 26 Aug 2015, 5644-5649, https://doi.org/10.1016/j.tet.2015.06.040.

[104] Nejedlý J., Šámal M., Rybáček J., Tobrmanová M., Szydlo F., Coudret Ch., Neumeier M., Vacek J., Chocholoušová J.V., Buděšínský M., Šaman D., Bednárová L., Sieger L., Stará I.G., Starý I., (2017). Synthesis of Long Oxahelicenes by Polycyclization in a Flow Reactor. Angew. Chem. 129, 21 May 15, 2017, 5933-5937, https://doi.org/10.1002/anie.201700341.

[105] Sehnal P., Stará I.G., Šaman D., Tichý M., Míšek J., Cvačka J., Rulíšek L., Chocholoušová J., Vacek J., Goryl G., Szymonski M., Císařová I., Starý I., (2009). An organometallic route to long helicenes. Proc Natl Acad Sci U S A. 2009 Aug 11; 106(32): 13169–13174, https://doi.org/10.1073/pnas.0902612106.

[106] Mori K., Murase T., Fujita M., (2015). One-step synthesis of [16]helicene. Angew Chem Int Ed Engl. 2015 Jun 1;54(23):6847-51, https://doi.org/10.1002/anie.201502436.

[107] Fan W., Winands T., Doltsinis N.L., Li Y., Wang Z., (2017). A Decatwistacene with an Overall 170° Torsion. Angew. Chem. 56, 48 Nov 27, 2017, 15373-15377, https://doi.org/10.1002/anie.201709342.

[108] Zhou Z., Fu L., Hu Y., Wang X.-Y., Wei Z., Narita A., Müllen K., Petrukhina M.A., (2020). Compressing Double [7]Helicene by Successive Charging with Electrons. Angew. Chem. 59, 37, Sep 7, 2020, 15923-15927, https://doi.org/10.1002/anie.202005852.

[109] Pradhan A., Dechambenoit P., Bock H., Durola F., (2016). Fused Helicene Chains: Towards Twisted Graphene Nanoribbons. Chem. Eur. J. 22, 50, Dec 12, 2016, 18227-18235, https://doi.org/10.1002/chem.201603702.

[110] Liu Ch., Yao B., Dong T., Ma H., Zhang S., Wang J., Xu J., Shi Y., Chen K., Gao L., Yu L., (2019). Highly stretchable graphene nanoribbon springs by programmable nanowire lithography. npj 2D Mater Appl 3, 23 (2019), https://doi.org/10.1038/s41699-019-0105-7.

[111] Baldwin J., Hancock Y., (2013). Effects of Strain on Notched Zigzag Graphene Nanoribbons. Crystals. 2013; 3(1):38-48, https://doi.org/10.3390/cryst3010038.

[112] Milovanović S.P., Peeters F.M., (2018). Strained graphene structures: from valleytronics to pressure sensing. Springer, Dordrecht, https://doi.org/10.1007/978-94-024-1304-5_1.

[113] Javvaji B., He B., Zhuang X., (2018). The generation of piezoelectricity and flexoelectricity in graphene by breaking the materials symmetries. Nanotechnology 29 225702, https://doi.org/10.1088/1361-6528/aab5ad.

[114] Rickhaus M., Mayor M., Juríčeka M., (2016). Strain-induced helical chirality in polyaromatic systems. Chem. Soc. Rev., 2016,45, 1542-1556, https://doi.org/10.1039/C5CS00620A.

[115] Rulíšek L., Exner O., Cwiklik L., Jungwirth P., Starý I., Pospíšil L., Havlas Z., (2007). On the Convergence of the Physicochemical Properties of [n]Helicenes. J. Phys. Chem. C 2007, 111, 41, 14948–14955,

https://doi.org/10.1021/jp075129a.

[116] Guo Y.-D., Yan X.-H., Xiao Y., Liu Ch.-S., (2015). U-shaped relationship between current and pitch in helicene molecules. Sci Rep. 2015; 5: 16731, https://doi.org/10.1038/srep16731.

[117] Müller W.R., Szymanski K., Knop J.V., Nikolić S., Trinajstić N., (1989). On the Enumeration and Generation of Polyhex Hydrocarbons. J Comput Chem. 11, 2, Mar 1990, 223-235, https://doi.org/10.1002/jcc.540110208.

[118] Senftle T.P., Hong S., Islam M.M., Kylasa S.B., Zheng Y., Shin Y.K., Junkermeier CH., Engel-Herbert R., Janik M.J., Aktulga H.M., Verstraelen T., Grama A., van Duin A.C.T., (2016). The ReaxFF reactive force-field: development, applications and future directions. npj Comput Mater 2, 15011 (2016), https://doi.org/10.1038/npjcompumats.2015.11.

[119] Datta A., Pati S.K., (2006). Dipolar interactions and hydrogen bonding in supramolecular aggregates: understanding cooperative phenomena for 1st hyperpolarizability. Chem. Soc. Rev., 2006,35, 1305-1323, https://doi.org/10.1039/B605478A.

List of Author's Publications

Publications on the topic of dissertation, impacted (WoS):

[A1] Davydova M., Laposa A., Smarhak J., Kromka A., Neykova N., Nahlik J., Kroutil J., Drahokoupil J., Voves J., (2018). Gas-sensing behaviour of ZnO/diamond nanostructures. Beilstein Journal of Nanotechnology. 2018, 9 9 22-29. ISSN 2190-4286. DOI: 10.3762/bjnano.9.4

Times cited: 14, Shares: DAVYDOVA 12%, ŠMARHÁK 11%, rest 11%

[A2] Šmarhák, J. and Voves J.. Electronic Transport Properties of Compressed and Stretched Helicene-Graphene Nanostructures, a Theoretical Study, 28.2.2021 submitted to Physica E: Low-dimensional Systems and Nanostructures, On 9.4.2021 the reviewer recommends reconsideration of minor revision and modification.

Shares: ŠMARHÁK 80%, Voves 20%

Other peer-reviewed publications (conference proceedings, WoS):

[A3] Šmarhák, J. and Voves J., (2013). Spin Filtering Ability of Patterned Graphene Nanoribbons. Nanocon 2013 5th International Conference, Brno, 2013. Ostrava: Technická universita Ostrava - Vysoká škola báňská, 2013. p. 113-117. ISBN 978-80-87294-47-5. http://www.nanocon.eu/files/proceedings/14/reports/1977.pdf.

Shares: ŠMARHÁK 50%, Voves 50%

[A4] Šmarhák, J. and Voves J., (2014). Electronic Transport Properties of [6+Nx12] Annulene Nets. Nanocon 2014 6th International Conference, Brno, 2014. Ostrava: Technická universita Ostrava - Vysoká škola báňská, 2014. ISBN 978-80-87294-55-0, 2015. p. 235-239. ISBN 978-80-87294-53-6.

Shares: ŠMARHÁK 50%, Voves 50%

[A5] Šmarhák, J. and Voves J., (2015). Simulation of Electron Transport in Helicenes. NANOCON 2015: 7th International Conference on Nanomaterials - Research and Application, Brno, 2015. Ostrava: Tanger, 2015. p. 178-181. ISBN 978-80-87294-63-5.

Shares: ŠMARHÁK 70%, Voves 30%

[A6] Šmarhák, J., (2015). Computer Quantum level Simulations of Helicene-based Structures for Novel bottom-up Molecular Organic Electronics. In: HUSNÍK, L., ed. Proceedings of the 19th International Scientific Student Conferenece POSTER 2015 . 19th International Student Conference on Electrical Engineering, Praha, 2015- 05-14. Praha: Czech Technical University in Prague, 2015. ISBN 978-80-01-05499-4.

[A7] Šmarhák, J., (2018). Impact of Stone-Wales defects on bandstructure, electron density and interatomic forces in graphene nanoribbon, Proceedings of the International Student Scientific Conference Poster – 22/2018. Praha: Czech Technical University in Prague, 2018. ISBN 978-80-01-06428-3.

[A8] Barulin, A., Šmarhák, J. and Voves J., (2018). Simulation of Epitaxially Grown Graphene on Step-Shaped SiC Surface. 8th International Conference on Nanomaterials - Research and Application, Brno, 2016. Ostrava: Tanger, 2016, ISBN 978-80-87294-68-0, 2017. p. 110-115. ISBN 978-80-87294-71-0.

Shares: BARULIN 34%, ŠMARHÁK 33%, VOVES 33%

Publications outside the topic of the dissertation, impacted (WoS):

[A9] Neue G., Benka T., Havránek M., Hejtmánek M., Janoška Z., Kafka V., Korchak O., Lednický D., Marčišovská M., Marčišovský M., Popule J., Šmarhák J., Švihra P., Tomášek L., Vrba V., Konček O., Semmler M., (2018). PantherPix hybrid pixel gamma-ray detector for radio-therapeutic applications. Journal of Instrumentation. 2018, 13 ISSN 1748-0221. DOI 10.1088/1748-0221/13/02/C02036

Shares: All 5.88%